Calibrated cryogenic amplifier measurements

Determining the characteristics of a current pumped nanobridge Josephson Parametric Amplifier using Short-Open-Load and Thermal Calibration

L. Locht

Technische Universiteit Delft

TU Delft

Calibrated cryogenic amplifier measurements

Determining the characteristics of a current pumped nanobridge Josephson Parametric Amplifier using Short-Open-Load and Thermal Calibration

by

L. Locht

to obtain the degree of Master of Science
at the Delft University of Technology,

Cover Image
Picture of the cryogenic system used in the project, with the blue cylinder being the essential switch for the calibration.

Project duration:	September, 2020 – November, 2021	
Daily supervisor:	W. J. M. Franse	
Thesis committee:	Prof. G. A. Steele,	TU Delft, supervisor
	Prof. Y. M. Blanter,	TU Delft
	Dr. T. van der Sar,	TU Delft
	Dr. A. Bruno,	Quantware

An electronic version of this thesis is available at `http://repository.tudelft.nl/`.

TU Delft

Abstract

In this project, we have done a calibrated measurement on a previously designed and fabricated current pumped Josephson Parametric amplifier. We have installed a microwave switch into our crygenic fridge to be able to get a calibrated response measurement using Short-Open-Load calibration, which we used with measurements of the gain and flux tunability of the device. This showed that our previous measurements on the gain deviated significantly, with about 10dB. We also did a thermal calibration on the amplifier by heating the plate it was attached to, and found that the input noise approximates the limit of a half quantum of noise.

List of Figures

List of Tables

Contents

1 Introduction

Amplifiers are one of the essential components that electronics are build upon, our modern digital world could not do without them. They take a signal and ideally output the same but with increased amplitude. Amplifiers have multiple attributes to describe their quality, but a few of the more descriptive are gain, bandwidth, input noise and dynamic range.

Input noise is the amount of noise added to the signal at the input of the amplifier, which will be amplified together with the signal. For certain purposes, such as Qubit readout in quantum computing, or in detecting gravity waves in astronomy, the amount of input noise is the most critical, as it decides what quantities can be measured.

And so, the search for ultralow noise amplifiers is a continuoing journey, of which one of the paths lead to a Josephson Parametric Amplifier. This is an amplifier for superconducting signals, and our variant, the current pumped one, is theoretically limited to a half quantum input noise, the same limit the signal is limited to.[2] This is achieved by doing without resistive components, as they add noise, but only using reactive components. This can be interpreted as instead pushing someone on a swing, to have them move their legs. This is also where the adjective parametric comes from, as the change in body posture changes the inertia, a parameter of the system. Or one could add a cubic term to a harmonic oscillator.

This requires a non-linear term in the reaction of a system however, which is supplied by the Josephson Junction, which can be described as a non-linear inductor. The rest of the non-linear harmonic oscillator will be provided by a capacitance. The power that the signal needs is in our case provided by a pump signal.

But what of the other properties of amplifiers. Well, the bandwidth is limited together with the gain, as with any resonator, resulting in a sharp peak around the pump frequency. This can however be practical if one only wants to amplify in a specific range, additionaly the Josephson Junctions can be used in pairs to form SQUIDS, which will make the resoncance frequency flux tunable. The dynamic range is dependent on the power of the pump, its power needs to be a couple of orders of magnitude higher than the signal. But the amplifier also works best at a very specific level of pump power, which results in a limited dynamic range. This level can be increased by using an array of JJ instead of a single one.

Josephson Junctions are made by having a small gap between superconductors, usually provided by an isolator. It can also be made by adding a constriction in the superconductor, resulting in a nanobridge, which is what is used in this report.

These design choices have lead to the fabrication of a nanobridge JPA, described in this report. Limited measurements were done, looking into the flux tunability and gain of the JPA. This projects aim is to get a precise estimate of these quantities, in addition to the most critical one, the input noise.

However, it was quickly discovered that the measurements previously taken were not sufficient for these goals, as they were distorted by the wires. A more detailed description of this can be found in section 9.1. These wires are neccesary as the JPA only functions at very low temperatures, and thus needs to be cooled using a cryogenic fridge, in our case the He7 entropy, as described in section 9.3.1. To mitigate the distortion of the wires on the results we needed to alter our setup. So in this project also methods to negate these problems were put into practice, short open load calibration to get a clear picture of the gain and flux tunability, and thermal calibration for a clear picture of the input noise.

2

Theory

2.1. Classical parametric amplification

Amplification has many purposes, for the measurement of signals with a tiny amplitude, to creating resonances with a large one, with noise as an important consideration. One can increase the amplitude of the signal with resistance, or by reactance, the latter will add no noise. This is what parametric amplification is all about. The prefix parametric comes from the fact that one changes a parameter of the system. For example with a person on a swing, one can change the system by changing his rotational inertia, in a reaction, as a counter balancing force. Though one needs some initial momentum, which we can see as the signal, another example is a pendulum with a spring as the string. There is no active component, everything happens as a reaction, and the spring does not add any additional energy to the system. We use an RLC circuit where the usage of a Josephson Junction as the inductance introduces the non-linearity, of which the characteristics are explained in 2.3.3. [11]

A pendulum without loss is a harmonic oscillator, so we will include a bit of damping, and also a cubic term, to account for the non-linearity. What we get is a Duffing oscillator, with its formula 2.1.[22]

$$m x'' + k x = 0 \tag{2.1}$$

$$x'' + r x' + \omega_0^2 x + \beta x^3 = 0 \tag{2.2}$$

Where r is the damping, ω_0 is the resonance frequency and β is the restoring force, in this analogy it can be caused by a change of the rotational inertia. Though this does not have an analytical solution, one can find the frequency dependence of the frequency response with this equation, with a driving signal of $F = \gamma \cos(\omega t - \phi)$, and internal amplitude of $A\cos(\omega T)$. This is on the condition $\frac{\beta A^2}{36\omega^2} \ll 1$, so the superharmonics remain insignificant.[4] So inserting the driving force and our internal wave into the previous equation gives, with neglection of the superharmonics:

$$\gamma^2 = \left(\left(\omega_0^2 - \omega^2\right) A + \frac{3}{4}\beta A^3\right)^2 + (r\omega A)^2 \tag{2.3}$$

$$\gamma^2 = A^6 \frac{9\beta^2}{16} + A^4 \frac{3\beta}{2}\left(\omega_0^2 - \omega^2\right) + A^2\left(r^2\omega^2 + \left(\omega_0^2 - \omega^2\right)^2\right) \tag{2.4}$$

Plotting these in figure 2.2, we can see that for most frequencies the oscillator dampens the signal, but for certain frequencies and a critical power the response function changes dramatically. Though our formula for the JPA will be slightly different, as our damping strength is frequency independent the principle remains. We can find the maximum of the response function by realizing that it happens for $\frac{\partial A}{\partial \omega} = 0$. To make the calculation more straightforward, we use $n = A^2$ and $\Delta\omega = \omega^2 - \omega_0^2 + \frac{r^2}{2}$. We use $\frac{\partial n}{\partial \Delta\omega} = 0$ to get the state where the slope is vertical, and take the derivative of the equation.

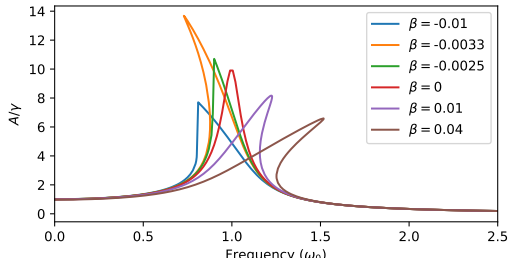

Figure 2.1: Duffing oscillator, the frequency response versus the frequency of the driving force, with values $\gamma = 1$, $\omega_0 = 1$, $r = 0.1$. Here we can see the influence of the size and sign of the non-linear term, note that the JPA has a negative value.

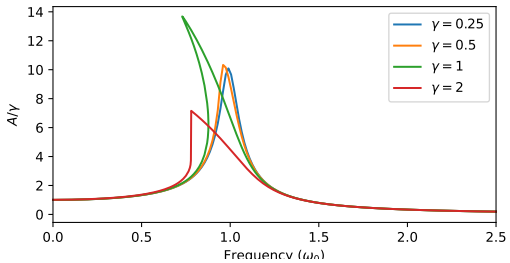

Figure 2.2: Duffing oscillator, the frequency response versus the frequency of the driving force, with values $\omega_0 = 1$, $r = 0.1$ and $\beta = -0.33$

$$0 = n^2 \frac{3\beta}{2} + n2\Delta\omega \tag{2.5}$$

$$n = \frac{4}{3\beta}\Delta\omega \tag{2.6}$$

We can put these back in to our previous third order equation, but the cubic term will drop out.

$$\gamma^2 = \frac{4r^2}{3\beta}\Delta\omega^2 + \frac{4}{3\beta}\left(\omega_0^2 r^2 - \frac{r^4}{4}\right)\Delta\omega \tag{2.7}$$

Since this is a quadratic equation, we will get two solutions, though only one points to our critical frequency. This is particularly useful to find the position where our response is at its maximum. We can see that it shifts linearly with n and the non-linearity.

Another interesting aspect of the Duffing oscillator is the fact that the behaviour has a phase change, the response will enter a bifurcation regime if an incoming signal is applied with a supercritical amplitude, as can bee seen in figure 2.2. In this region there are three real and two stable solutions, and they can be found separately by either lowering or increasing the frequency, as can be seen in figure 2.3, though the semi stable state cannot be reached this way. For the use of the resonator for amplification the critical state, where the slope of the response function is vertical, is most important, or one could say the two jumps seen in figure 2.3 happen at the same point. This has a single value for power, the bifurcation power, and for frequency, the critical frequency, for a single system.

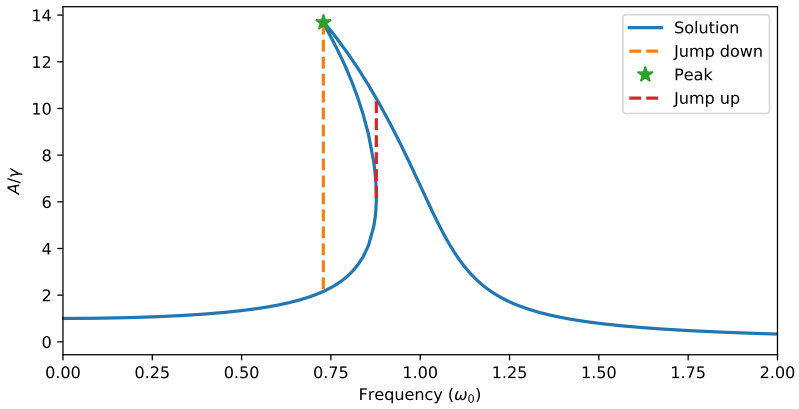

Figure 2.3: The maximum response at this power can be reached at the green star, but if one finds it while decreasing the frequency, the response will jump down if the frequency gets below that point(orange line). Other way around one finds a jump up(red line).

2.2. Microwave theory

2.2.1. Impedance

To describe an AC circuit well, one needs not only include its resistance, but also its reactance, caused by the capacitance and inductance. Impedance is used to describe electrical components in the relation of current and voltage at that point in the frequency domain, with a steady state solution. So without direct current $Z = \frac{V(\omega)}{I(\omega)}$. The impedances of a resistance, capacitance and an inductor respectively are:

$$Z_R = R \tag{2.8}$$

$$Z_C = \frac{1}{i\omega C} \tag{2.9}$$

$$Z_L = i\omega L \tag{2.10}$$

Impedance is dependent on direction, with linear elements opposite directions will have opposite impedance in the same basis frame, as the current will flow in opposite directions. The same value of impedance can be achieved with either resistive or reactive components. Devices of the that are impedance matched have no reflections between them, everything is transmitted, this is further discussed in the next paragraph 2.2.2. Practically this will usually be referenced to a common ground, as it is voltage dependent.

2.2.2. Transmission lines

For the most part, our signals are transferred by coaxial wires. Ideally they should not have any resistance, but they will still change the phase of the signal because of their length. A distributed lumped element notation of a transmission line can be seen in figure 2.4. A wire can be modeled as an infinite sequence of this component, although when $l \ll \lambda$ it can be approximated with just one. Using Kirchhoff's laws, and taking a derivative to

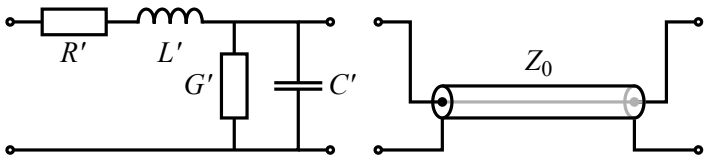

Figure 2.4: Distributed Lumped element representation of a transmission line on the left, while the symbol used in this report is on the right.

length, we find for relations:

$$V'(x,t) = -R'I(x,t) - L'\dot{I}(x,t) \tag{2.11}$$

$$I'(x,t) = -G'V(x,t) - L'\dot{V}(x,t) \tag{2.12}$$

Where for an arbitrary parameter a, a' denotes derivate to space, and a $\dot{a}$ denotes a derivate to time. Then using a Fourrier transformation for the derivative to time and inserting them in one another, we can find two simple second order differential equations to length.

$$V(x)'' = \gamma^2 V(x) \tag{2.13}$$

$$I(x)'' = \gamma^2 I(x) \tag{2.14}$$

Where $\gamma = \sqrt{(R + i\omega L)(G + i\omega C)}$ denotes the complex propagation constant. The solutions for our traveling waves are thus:

$$V(x) = V_- e^{\gamma x} + V_+ e^{-\gamma x} \tag{2.15}$$

$$I(x) = I_- e^{\gamma x} + I_+ e^{-\gamma x} \tag{2.16}$$

Where the time dependence is in ω in the γ. The solutions are symmetric, so $S_{21} = S_{12}$, this is indeed true for this model, and for any linear element, so as long as the cable has similar properties at each point, it will hold up in practice. The imaginary part of the propagation constant describes how quickly the signal builds up phase in time and space, while the real part denotes how much the amplitude of the signal changes to the same respect. In practice the wave's speed is usually denoted as a fraction of the speed of light, while the attenuation is denoted as 1 meaning no attenuation.

Since the impedance is defined by the relation of the voltage and current, as dependent on time and space, one can find the impedance of the line:

$$Z_0 = \sqrt{\frac{R + i\omega L}{G + i\omega C}} \tag{2.17}$$

$$Z_0 = \frac{V_+}{I_+} = -\frac{V_-}{I_-} \tag{2.18}$$

The minus in the last term may seem odd, but it represents the current going in the other direction, increasing the voltage of the wave in the negative direction should decrease the current in the positive direction. Where in the ideal case $Z_0 \approx \sqrt{\frac{L}{C}}$. We will attach a load to our line though, and the impedance found with a transmission line of length l is:

$$Z_{in}(0) = \frac{V(0)}{I(0)} = Z_L \tag{2.19}$$

$$Z_{in}(l) = \frac{V(l)}{I(l)} = \frac{V_-(0)e^{\gamma l} + V_+(0)e^{-\gamma l}}{I_-(0)e^{\gamma l} + I_+(0)e^{-\gamma l}} = \frac{\cosh(\gamma l)\,(V_-(0) + V_+(0)) + \sinh(\gamma l)\,(V_-(0) - V_+(0))}{\cosh(\gamma l)\,(I_-(0) + I_+(0)) + \sinh(\gamma l)\,(I_-(0) - I_+(0))} \tag{2.20}$$

$$= \frac{1}{Z_L}\frac{Z_L + \tanh(\gamma l)Z_0}{\frac{1}{Z_L} + \tanh(\gamma l)\frac{1}{Z_0}} = Z_0\frac{Z_L + \tanh(\gamma l)Z_0}{Z_0 + \tanh(\gamma l)Z_L} \tag{2.21}$$

Where we used the equations 2.15 and 2.16. Another way is to look at the reflection coefficient

$$\Gamma_{in}(l) = \frac{V_+(l)}{V_-(l)} = \frac{V_+(0)e^{-\gamma l}}{V_-(0)e^{\gamma l}} = \Gamma_L e^{-2\gamma l} \tag{2.22}$$

2.2.3. Reflection and Transmission

Attaching different loads to the end of the transmission line will describe most ideal components for our setup. Since we will do reflection measurements in our experiments, this is also what we more or less do with our devices. We have the short, denoting zero resistance, or negligible. An open, denoting infinite resistance, which is provided by a large capacitance, and a resistor at equal impedance. Attaching these to the wire and measuring each gives us the information to know what happens in the wire, and we can thus remove this distortion if we measure a device connected to it, which is the basis of our calibration, seen in section 2.6.

The same impedance as the load could also be gained from an infinite transmission line, even though there are no resistive components. This is due to the fact that there will never be a reflecting wave, and along the line there is still a voltage between the ground and input line. In practice, there will always be a small impedance mismatch, resulting in a reflecting wave in the wires, so called cable resonances.

$$\Gamma = \frac{V_-}{V_+} = \frac{(V_+ + V_-) + (V_- - V_+)}{(V_+ + V_-) - (V_- - V_+)} = \frac{Z_L - Z_0}{Z_L + Z_0} \tag{2.23}$$

Which is indeed zero for $Z_0 = Z_L$. The transmitted power will thus always decrease for larger impedance mismatches. In fact if $Z_L = Z_0 + \Delta Z$:

$$\Gamma = \frac{\Delta Z}{2Z_0 + \Delta Z} \tag{2.24}$$

Where the limits $\Delta Z = -2Z_0$ and $\Delta Z = \infty$ resulting in an short and open respectively. With this we can find out the ratio of the reflecting waves, the Standing Wave Ratio:

$$|SRW| = \frac{1 + \Gamma}{1 - \Gamma} \tag{2.25}$$

These impedance mismatches will make measuring quantitatively very difficult, if not impossible, even without actual resistance. If we attach our device to the end of the transmission line, a part of the signal will bypass the device, and a part will reflect back into the device after exiting from the device, resulting possibly in a feedback loop. These fractions can better be described using S-parameters, and this will also give us the freedom of non-linear elements and a different input from output line.

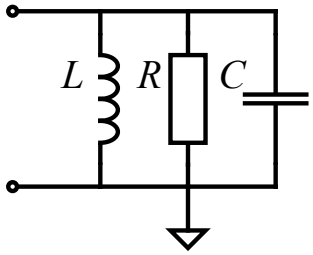

Figure 2.5: An RLC circuit.

2.2.4. RLC circuit

As mentioned earlier, we do not use a pendulum but an electronic circuit, a parallel RLC circuit, as seen in 2.5. [10]

We can do the calculations here as if it would have been a regular RLC circuit, since we can treat Z_0 and R as parrelel resistors, meaning $R_{tot} = \frac{RZ_0}{R+Z_0}$. A description of an RLC circuit as a harmonic oscillator is widely known, and will be used to find the Hamiltonian in subsection 2.3.6.

$$0 = \frac{1}{R} + \frac{1}{Z_0} + i\omega C + \frac{1}{i\omega L} = \frac{R+Z_0}{RZ_0} + i\omega C + \frac{1}{i\omega L} \tag{2.26}$$

Let us now look at the input impedance, this is the impedance as seen from the wire.

$$\frac{1}{Z_{in}} = \frac{1}{R} + i\omega C + \frac{1}{i\omega L} \tag{2.27}$$

$$Z_{in} = \frac{i\omega LR}{R + i\omega L - \omega^2 CLR} = \frac{R}{1 + \frac{R}{i\omega L} + i\omega CR} = \frac{R}{1 + i\omega_0 RC\left(\frac{\omega}{\omega_0} - \frac{\omega_0}{\omega}\right)} \tag{2.28}$$

Using the fact that for the resonance frequency the imaginary part should vanish one can get $\omega_0 = \frac{1}{\sqrt{LC}}$.

$$\frac{1}{Q} = \frac{P}{E\omega_0} = \frac{\frac{V^2}{2R_{tot}}}{\omega_0 \frac{CV^2}{2}} = \frac{1}{\omega_0 CR_{tot}} = \frac{R+Z_0}{\omega_0 RZ_0 C} = \frac{1}{\omega_0 Z_0 C} + \frac{1}{\omega_0 RC} \tag{2.29}$$

$$\frac{1}{\omega_0 Z_0 C} = \frac{1}{Q_{ext}} = \frac{\kappa_{ext}}{\omega_0} \qquad \frac{1}{\omega_0 RC} = \frac{1}{Q_{int}} = \frac{\kappa_{int}}{\omega_0} \tag{2.30}$$

Our resonator can be described by either the dimensionless quality factor Q or by the decay rate, $\kappa = \frac{\omega_0}{Q}$ which is connected to the coupling, which we will later use for the connection to the bath of the Hamiltonian in subsection 2.3.6. The energy dissipated can also be seen as transferring it to a bath, with externally the transmission line or κ_{ext}, and internally the resistor with κ_{int}. The larger the coupling, the faster the transferring, which relates to a lower Q_{int}, as that factor is higher with more storage and less transferal. This is also related to the width of the resonator, as can also be deferred from the reflection parameter:

$$\Gamma = \frac{Z_L - Z_0}{Z_L + Z_0} = \frac{R - Z_0\left(1 + i\omega_0 RC\left(\frac{\omega}{\omega_0} - \frac{\omega_0}{\omega}\right)\right)}{R + Z_0\left(1 + i\omega_0 RC\left(\frac{\omega}{\omega_0} - \frac{\omega_0}{\omega}\right)\right)} \approx \frac{\kappa_{ext} - \kappa_{int} - 2i\Delta\omega}{\kappa_{ext} + \kappa_{int} + 2i\Delta\omega} \tag{2.31}$$

Where $\Delta\omega \approx \frac{\omega_0}{2}\left(\frac{\omega}{\omega_0} - \frac{\omega_0}{\omega}\right)$ an approximation discussed later, also this response function equates to an open $\lambda/2$ resonator, or a shorted $\lambda/4$ resonator. It is now visible where the limits are, with $R < Z_0$, $R = Z_0$ and $R > Z_0$ being under, critically and overcoupled respectively, or in Q's, $Q_{int} < Q_{ext}$, $Q_{int} = Q_{ext}$ and $Q_{int} > Q_{ext}$. Now the cavity can be controlled as two parameters, the different Q, as can be seen in figure 2.6.

A critical coupling results in all power being dissipated when frequency is at resonance. Overcoupling means there is less dissipation into the loss modes then there is back into the transmission line, and into the limit will result in this resonator acting like an open. Undercoupling results in energy being transferred quicker to the resistor then the transmission line, resulting in a reflecting wave if one takes the limit. Also $\Delta\omega \approx \frac{\omega_0}{2}\left(\frac{\omega}{\omega_0} - \frac{\omega_0}{\omega}\right)$ The approximation of $\Delta\omega$ is only valid when $\frac{1}{Q_{ext}} + \frac{1}{Q_{int}} \ll \omega_0$. As can be seen in in the next figure, figure 2.7.

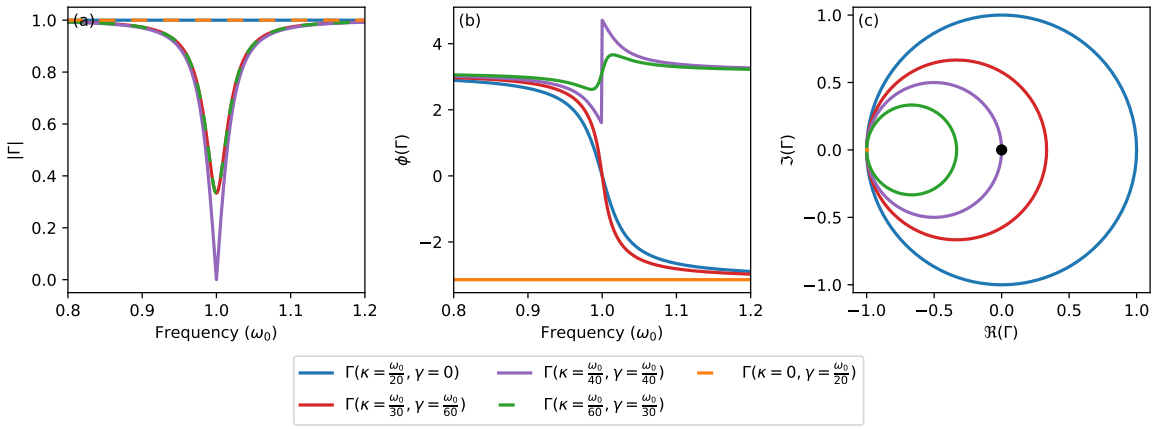

Figure 2.6: From left to right, magnitude, phase and polar plot of the reflection spectrum of a cavity, for different values of internal and external coupling, denoted by γ and κ respectively.

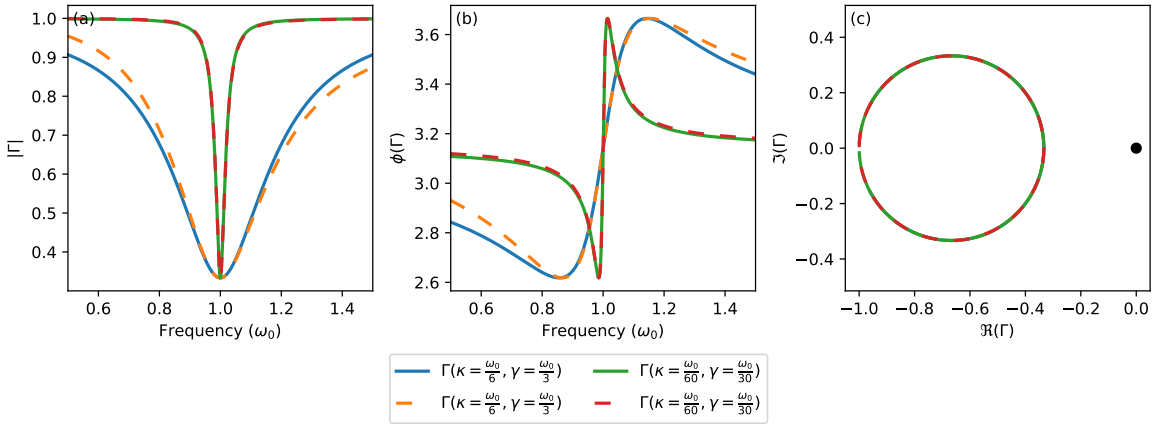

Figure 2.7: From left to right, magnitude, phase and polar plot of the reflection spectrum of the cavity of the RLC circuit. Comparison of the extract and approximated reflection spectrum, with the approximation being for frequency.

Hamiltonian

However, to describe the system quantum mechanically, a Hamiltonian is a more practical description. We can again see the transmission line as a resistor in parallel, meaning we get as our time dependent description.

$$\phi = \int_{-\infty}^{t} V\,dt \tag{2.32}$$

$$0 = \frac{\dot{\phi}}{R_{tot}} + C\ddot{\phi} + \frac{\phi}{L} \tag{2.33}$$

With ϕ being the generalized flux. Hamiltonians are without loss however, so we will neglect the resistance for now. We will later include the dissipation by using an external coupling with the environment. Since this produces damping by coupling to a bath, it will not change the behaviour of the simualated resonator. One way to find the Hamiltonian is by using the Lagrarian of the system, where we use the inductive as potential and the capacitive as kinetic energy.

$$E_{pot} = \frac{I^2 L}{2} \qquad E_{kin} = \frac{CV^2}{2} \tag{2.34}$$

Where they store their energy in a magnetic field or charge density respectively. We can also get the next equation by multiplying equation 2.33 with the voltage, and then integrating over time.

$$\mathscr{L} = E_{kin} - E_{pot} = \frac{CV^2}{2} - \frac{I^2 L}{2} = \frac{C\dot{\phi}^2}{2} - \frac{\phi^2}{2L} \tag{2.35}$$

$$q = \frac{\partial \mathscr{L}}{\partial \dot{\phi}} = C\dot{\phi} \tag{2.36}$$

$$\mathscr{H} = \dot{\phi}\frac{\partial \mathscr{L}}{\partial \dot{\phi}} - \mathscr{L} = \frac{C\dot{\phi}^2}{2} + \frac{\phi^2}{2L} = \frac{q^2}{2C} + \frac{\phi^2}{2L} \tag{2.37}$$

And as expected, gives the harmonic oscillator, with the build up of charge as potential energy, and the flux as kinetic energy. So we still need some damping, which can easily be included by using a resistor, which relates to a coupling to a bath. We also need the non-linearity, that can be achieved by using a Josephson Junction, as explained in section 2.3.3.

In our case, we use a capacitively coupled RLC circuit, but we can show it does not introduce any new behaviour, as it gives approximately the same solution for the reflection as seen in the next section, aside from a constant factor.

2.2.5. Capacitively coupled RLC circuit

In this section, we will go into detail how our system,as described in Franse [13] differs form a regular parallel RLC circuit, we mostly expect the reflection to be different by a factor of -1. As we did last time, we can model

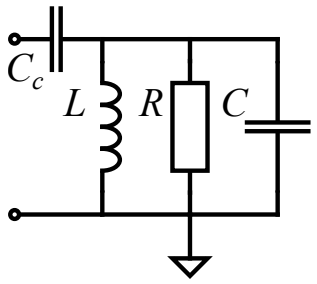

Figure 2.8: A capacitively coupled RLC circuit.

the transmission line as an additional resistance in parallel, but this time with C_c in series. So we start with the impedance as:

$$0 = \left(Z_0 + \frac{1}{i\omega C_c}\right)^{-1} = \frac{i\omega C_c}{1 + i\omega C_c Z_0} = \frac{\omega^2 Z_0 C_c^2}{1 + \omega^2 Z_0^2 C_c^2} + \frac{i\omega C_c}{1 + \omega^2 Z_0^2 C_c^2} = \frac{1}{R'} + i\omega C' \tag{2.38}$$

$$0 = \frac{1}{R} + \frac{1}{R'} + i\omega(C + C') + \frac{1}{i\omega L} \tag{2.39}$$

Which would mean we have a frequency dependent capacitance and resistance. For the total resistance and capacitance:

$$R_{tot} = \frac{RR'}{R + R'} = \frac{Z_0 R\left(1 + \omega^2 Z_0^2 C_c^2\right)}{Z_0 + (R + Z_0)\omega^2 Z_0^2 C_c^2} \tag{2.40}$$

$$C_{tot} = C + C' = C + \frac{C_c}{1 + \omega^2 Z_0^2 C_c^2} \tag{2.41}$$

While for the couplings we get, if we assume $\omega^2 Z_0^2 C_c^2 \ll 1$:

$$\kappa_{tot} = \frac{1}{R_{tot} C_{tot}} = \frac{\omega^2 Z_0^2 C_c^2}{Z_0\left(C_c + C + C\omega^2 Z_0^2 C_c^2\right)} + \frac{1 + \omega^2 Z_0^2 C_c^2}{R\left(C_c + C + C\omega^2 Z_0^2 C_c^2\right)} = \kappa_{ext} + \kappa_{int} \approx \frac{\omega^2 Z_0^2 C_c^2}{Z_0\left(C + C_c\right)} + \frac{1}{R\left(C + C_c\right)} \tag{2.42}$$

We can see that if one aims for a large coupling, to create a wide cavity, one can increase L, which would have the opposite effect previously, or decrease C_C. For the input impedance we get:

$$Z_{in} = \frac{i\omega LR}{R + i\omega L - \omega^2 CLR} + \frac{1}{i\omega C_c} \tag{2.43}$$

The reflection constant or the resonance frequency cannot be easily differed from this, but we can, as we have used for the Hamiltonian, calculate these for the lossless case and then add couplings. Since we want an amplifier, we want κ_{int} to be as small as possible. First the resonance frequency:

$$\lim_{R\to\infty} Z_{in} = \frac{i\omega L}{1-\omega^2 CL} + \frac{1}{i\omega C_c} = \frac{1-\omega^2 CL-\omega^2 C_c L}{i\omega C_C\left(1-\omega^2 CL\right)} \approx \frac{2iL(C+C_c)^2}{C_c^2}\Delta\omega \tag{2.44}$$

Giving us an approximate resonance frequency of:

$$\lim_{R\to\infty} \omega_0 = \frac{1}{\sqrt{L(C+C_c)}} \tag{2.45}$$

In the end, we find for the reflection coefficient:

$$\Gamma \approx \frac{\kappa_{int}-\kappa_{ext}+2i\Delta\omega}{\kappa_{ext}+\kappa_{int}+2i\Delta\omega} \tag{2.46}$$

Where this response function equates to an open $\lambda/4$ resonator, or a shorted $\lambda/2$ resonator. Which is the same as for our previous circuit, except for a factor of -1, as can be seen in figure 2.9, although the couplings are quite different. A comparison between the exact and approximate reflection spectrum can be found in the appendix, subsection 9.2.3.

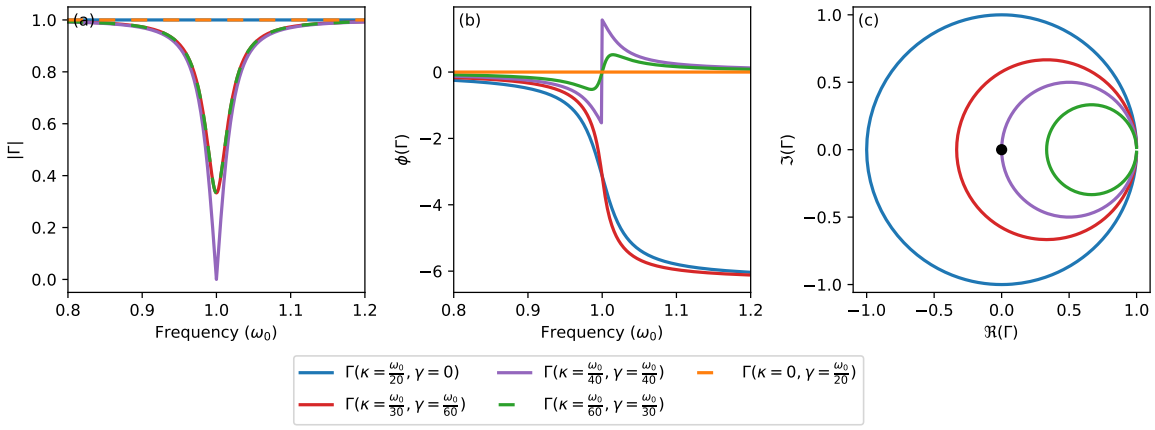

Figure 2.9: From left to right, magnitude, phase and polar plot of the reflection spectrum of the cavity of the RLCC, for different values of internal and external coupling.

The Hamiltonian will mostly be the same as in equation 2.37, even though the other capacitor can now also be charged. One major difference, is the fact that the coupling is different, which will influence the outcome of our input output theory in section 2.5.

2.2.6. Scattering-parameters

The most simple way to model any linear system is to use S-parameters, in fact it can be proven that as long as the transmission and reflection is only frequency dependent, that a one port system can be described with just three parameters. These are S_{11}, S_{22} and $S_{21}S_{12}$ as seen in figure 2.10, with these parameters denoting bypass, back reflection and transmission respectively. With some basic linear algebra one can find that the

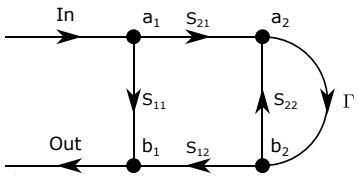

Figure 2.10: Simple model for Reflection Cavity

measured reflection Γ' depends on the system and the actual reflection as:

$$\Gamma' = S_{11} + \frac{S_{21}S_{12}\Gamma}{1-S_{22}\Gamma} \tag{2.47}$$

Scattering, while mostly caused by impedance mismatches, can result in a frequency and phase dependent alteration of our measured reflection spectrum.[24] Our goal is to measure a resonator, which should result in a reflection spectrum containing a lorentzian centered at the resonance frequency, as can be seen in figure 2.6. Interference due to these mismatches can result in the morphing of our lorentzians, as described by FANO in the next subsection, 2.2.7.[12] This is problematic as it can possibly go unnoticed, but another issue is that the state of the JPA changed by pumping will also change its shape, which can be hard to distinguish from it.

2.2.7. Fano

Fano is a type of scattering resulting in a assymetric lineshape, in our case the scattering is mostly due to impedance mismatches.[12] This would result in S_{21} and S_{12} being symmetric, as they are for a transmission line, but if we use a different input line and output line, this will no longer hold.

FANO changes the shape of our response function, which can be seen in figure 2.6. This can be detrimental to our measurements, as the shape of the line tells us a great deal about the state of our Duffing Oscillator. In addition, FANO can also change the measured properties of the system without making it asymmetric, this can possibly result in FANO altering the measurements without us noticing. We will look into these possibilities, as can be seen in figure 2.11.

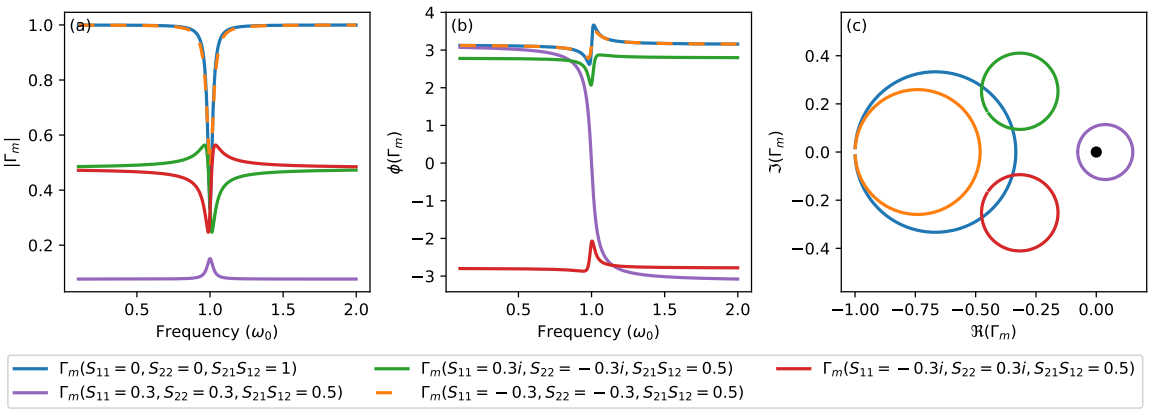

Figure 2.11: Measured reflection spectrum under influence of scattering parameters, resulting in morphed lorentzians, otherwise known as FANO.

Here we can see the different effects of the settings, though with the knowledge of our cavity we could try to get our original shape back. This only works to an extent though, as the outputs are not unique. The different scattering parameters may change the external and internal coupling we find, in addition to the Q factor. Fano can be mitigated by SOL calibration, as described in 2.6.1.

2.3. Circuit superconduction

For parametric amplification, we need a non-linear element, which is not included in elementary components of a classical electronic circuit. In a superconducting circuit however, we can make use of Josephson Junctions which are non-linear, as described in subsection 2.3.3. Since we have ultralow noise specifications, we want to cool our circuit to near zero anyway. Since resistance generates heat, no resistance is ideal, which is exactly the result of superconduction, as described next.

2.3.1. Superconduction basics

The basic model of conduction in metals is the "free electron gas", which just fills the space of the wire with free moving electrons, that do not interact with each other. Neither do they interact with the atoms inside the metal, though due to the electrons being fermions, only a small amount of electrons actually contribute to the conduction, which move way faster than the group electron speed. This is due to the limited energy states, since there are states for each direction, in its ground state each of these cancel each other out. A small but nonzero energy is required to distort this balance, though this is much lower than with a semiconductor. This energy can be lost due to collisions in the lattice, which is why there is always a nonzero resistance in a wire.

When cooling certain poor conducting metals to very low temperatures, in our case aluminium below approximately one Kelvin,[9] we suddenly have conduction with no resistance. One of the description of superconduction, the Bardeen Cooper Shieffer theory, or BCS[3], states that beyond this phase change, lower energy states are created. These come from electrons with equal but opposite momentum forming a cooper pair. Electrons due to the ions in the lattice have a small but non zero binding energy neglected in the previous model. At very low temperatures, this becomes larger than the repulsion between the electrons, so the forming of pairs becomes favourable. This results in perfect conduction, since the conducting pairs will form in the ground state.

Since electrons both have an half integer of spin, the pairs form bosons, and no longer follow the fermion expulsion prinicple. This results in an unlimited number of pairs forming, as of Bose-Einstein condensation. With pure metal superconductors, these have opposite spin, though there is also a different type of superconduction where the electrons have equal spin. The momentum is in any case opposite however, which means that these electrons may not be close apart. The superconducting state can then be better interpreted as a collective wave function in the Schrodinger picture, rather than separate pairs. The opposite momentum also means that they acquire kinetic momentum in opposite direction in a magnetic field, resulting in the Quantum Hall Effect.[7]

Since the Cooper pairs form a collective wave function, any path that starts and ends at the same point needs to acquire a phase of $2n\pi$ with $n \in \mathbf{Z}$. This means that in a loop where flux passes through the flux is quantized, any flux apart from this will thus be countered by a current through said loop. There is no resistance in the superconductor, so the phase acquired by an electron pair is always the same, resulting in the flux quantum: $\Phi_0 = \frac{h}{2e}$ Since most magnetic fields do not penetrate far into a superconductor, this would require a hole in the superconductor. This is one of the ideas behind a SQUID, which consists of two symmetric Josephson Junctions in parallel, and is our nonlinear circuit component, as described in subsection 2.3.5.

Another part of the superconducting behaviour that is important for the SQUID is the behaviour at the edge of the superconductor. The pair states do not exist outside the superconductor, but due to the wave properties of our collective wavefunction, they extend a bit outside of the superconductor. Using junction with a metal, an isolator or even a vaccuum between two superconductors they will overlap, and they will approach weak link behaviour, which is called an SIS junction in the case of an isolator, which is depicted in figure 2.12.

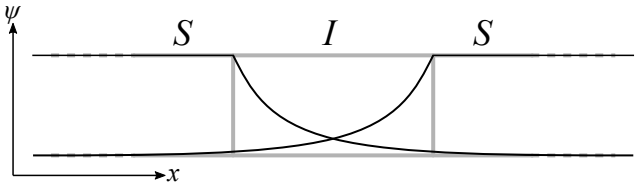

Figure 2.12: Depiction of the wavefunctions overlapping at an SIS junction.

This only holds for small gaps for conductors, because the coupling decreases exponentially, at some point the coupling between the superconductor to the conductor to the superconductor becomes larger. An

electron from the conductor of enough energy will bounce back as a hole, resulting in an electron pair in the superconductor, and vice verca, which forms an SNS junction.

The weak link behaviour between two superconductors is important for a SQUID, as the discontinuity of phase impacts the current, and the that phase difference can be influenced with a magnetic field. We can also use constrictions for weak link behaviour, with for example point contacts or tiny "bridges". This is what is used in our SQUID design. The behaviour at these junctions, the Josphson Relations, is described in the next subsection, while discussion of our type of constructions is discussed in 2.3.4. These relations describe the behaviour of the two collective wavefunctions over the junctions.

2.3.2. Josephson Relations

The collective wave function of superconduction can be described by the amount of particles, and their phase. This is called the order parameter, normalized as such, from the Landau macroscopic theory describing phase changes.

$$\psi = |\psi| e^{i\phi} = \sqrt{n} e^{i\phi} \tag{2.48}$$

Where n is now related to the pair density, which was given a microscopic connection later. With two symmetric superconductors with a gap, the densities will be similar, but the phase may not, so:

$$\psi_a = \sqrt{n_a} e^{i\phi_a} \approx \sqrt{n} e^{i\phi_a} \qquad \psi_b = \sqrt{n_b} e^{i\phi_b} \approx \sqrt{n} e^{i\phi_b} \tag{2.49}$$

Where we can define $\delta = \phi_b - \phi_a$. The two seperate wavefunctions overlap at the junction, also called a Jospehson junction, resulting in a coupling. If there is a voltage difference between the superconductors, there will be an energy difference of $2eV$, since the carrier consists of two electrons. This can be seen as a two state Schrodinger system.

$$i\hbar \frac{\partial}{\partial t} \begin{bmatrix} \psi_a \\ \psi_b \end{bmatrix} = \begin{bmatrix} eV & \kappa \\ \kappa & -eV \end{bmatrix} \begin{bmatrix} \psi_a \\ \psi_b \end{bmatrix} \tag{2.50}$$

Where ψ_a and ψ_b are the collective wavefunctions of the two superconductors coupled to each other by κ, and the energies can be found by the values on the diagonal, for example, ψ_a can be found by $E_a = \langle \psi_a | eV | \psi_a \rangle$ Solving these equations give us the equations:

$$\dot{\phi_a} = \frac{-eV - \kappa\sqrt{\frac{n_b}{n_a}}\cos\delta}{\hbar} \qquad \dot{\phi_b} = \frac{eV - \kappa\sqrt{\frac{n_a}{n_b}}\cos\delta}{\hbar} \tag{2.51}$$

$$\dot{n_a} = \frac{2\kappa\sqrt{n_a n_b}\sin\delta}{\hbar} \qquad \dot{n_b} = \frac{2\kappa\sqrt{n_a n_b}\sin\delta}{\hbar} \tag{2.52}$$

Realizing that the current in proportional to the amount of charge carriers we get the Josephson equations.

$$I = \frac{4e\kappa\sqrt{n_a n_b} A_J}{\hbar} = I_c \sin\delta \tag{2.53}$$

$$\dot{\delta} = \dot{\phi}_b - \dot{\phi}_a = \frac{2eV}{\hbar} = \frac{2\pi V}{\Phi_0} \tag{2.54}$$

Where A_J would be the surface of the junction if n would be the average pair density of the surface. Together with the coupling they give the critical current of the junction, or the maximum current which can pass through. This is the defining feature of a junction, and is dependent on the junction design, shape and composition. With the relations, we will now take a look as a circuit component, in the next subsection.

2.3.3. Josephson Inductance

We start at the Josephson Relations, as given in equation 2.53. We can integrate the relation to voltage to find the relation to generalized flux, where we use Φ instead of ϕ we used earlier.

$$\delta = \frac{2e\Phi}{\hbar} = \frac{2\pi\Phi}{\Phi_0} \tag{2.55}$$

Where δ is the reduced phase drop across the junction and $\Phi_0 = \frac{h}{2e}$. As for the energy:

$$E_{pot} = \int_0^{\bar{t}} IV\,dt = \int_0^{\bar{t}} I_c \sin\delta \frac{\Phi_0}{2\pi}\dot{\delta}\,dt = \frac{I_c\Phi_0}{2\pi}\int_0^{\bar{\delta}} \sin\delta\,d\delta = \frac{I_c\Phi_0}{2\pi}(1-\cos\delta) \tag{2.56}$$

Now for the Inductance, note that we have a non-linear inductance, while this is not normally the case, as such there is a difference in definition. We can either use $\Phi = LI$ where $\Phi(t) = \int_0^t V(\bar{t})d\bar{t}$, $\Phi = \frac{\hbar}{2e}\delta = \frac{\Phi_0}{2\pi}\delta$ or

$$V = \frac{\mathrm{d}\Phi}{\mathrm{d}t} = L\frac{\mathrm{d}I}{\mathrm{d}t} \tag{2.57}$$

The difference between these definitions only becomes relevant when the inductance is non-linear, as the derivative of the inductance to time is no longer constant. We will use the second one in this document, though papers we refer to, such as [11], may use the first.

$$L = \frac{\Phi}{I} = \frac{\hbar}{2eI_c}\frac{\delta}{\sin\delta} \tag{2.58}$$

We define $L_J \equiv \frac{\hbar}{2eI_c} = \frac{\Phi_0}{2\pi I_c}$ and a taylor expansion to get our non-linear terms:

$$L = L_J\frac{1}{\cos\delta} = L_J\left(1 - \frac{\delta^2}{2} + \frac{\delta^4}{24} + ...\right) \tag{2.59}$$

Where the third term gives rise to our Kerr non-linearity. For this inductor we have a symbol to denote it in circuits, as can be seen in figure 2.13.

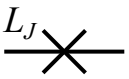

Figure 2.13: Symbol for the Josephson Junction

The capacitance of a non-ideal Josephson Junction is also nonzero, since the entire junction can be modeled as a parallel RLC circuit, with inductance L_J and capacitance C_J, as in the RCSJ model[33], as see in figure 2.14.

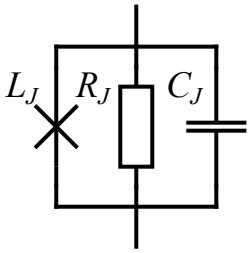

Figure 2.14: Approximation of the Josephson Junction with the RCSJ model.

This gives:

$$I_{tot} = I_c\sin\delta + \frac{V}{R} + C_J\frac{\mathrm{d}V}{\mathrm{d}t} \tag{2.60}$$

However, we use an additional capacitance in parallel, so it will not impact the resonant frequency, as our additional capacitance should be orders of magnitude larger.

2.3.4. NanoBridges

Now the Nanobridge part of the title relates to the Josephson junctions, depicted in figure 2.15. As our nanobridges are connected to 3D banks, they approach weak link behaviour, or an SNS junction, including their nonlinearity. Their resistance increases linearly with length after a certain offset, which is due to the banks.[37]

If we model our weak link as an aparature with surface S and chance of transmission D, we can find an equation for the critical current in the form of:

$$I_c = \frac{\pi\Delta}{2eR_n}\frac{\sin\delta}{\sqrt{1 - D\sin\frac{\delta}{2}^2}}\tanh\frac{\Delta}{2T}\sqrt{1 - D\sin\frac{\delta}{2}^2} \tag{2.61}$$

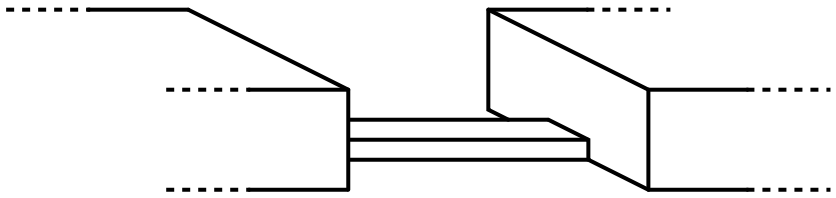

Figure 2.15: Schematic of our nanobridges, where the bridge is smaller in each dimension, though only in one vertical direction.

where $R_n^{-1} = \frac{e^2 k_F^2 SD}{4\pi^2 \hbar}$ is the normal state resistance, or Shervan resistance, Δ is the superconducting gap and T is the temperature. We can take this in a ballistic limit, which hold approximately for our nanobridges, as in [37]. Or we can take it in the limit of a tunnel junction, for the SIS junctions. When $D \ll 1$

$$I_c = \frac{\pi\Delta}{2eR_n} \sin\delta \tanh\frac{\Delta}{2T} \tag{2.62}$$

And when $D \approx 1$

$$I_c = \frac{\pi\Delta}{eR_n} \sin\frac{\delta}{2} \tanh\frac{\Delta\cos\frac{\delta}{2}}{2T} \tag{2.63}$$

Our junction is only close to this behaviour, actually having a value less but still on the same order of magnitude[16]. The main difference from these equations, is that the critical current should be higher with the nanobridges, since D is much larger for the nanobridge junctions than the SIS junctions. The results in practice of these different designs is looked into in section 6.1.

2.3.5. SQUIDS

SQUIDS consist of a loop with two symmetric arms, and a Jospephson Juncion in each, as can be seen in figure 2.16. Since the paths are of equal length, this will mean that both sides have the same current, if the phase jump is the same.

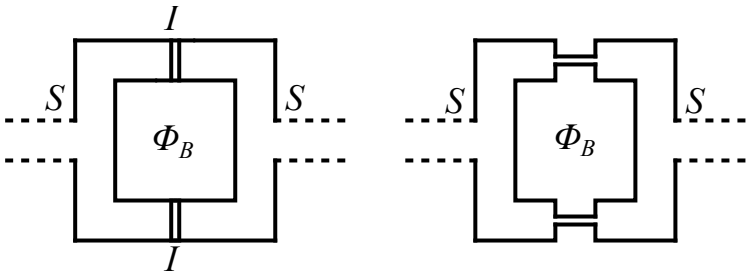

Figure 2.16: Schematic of a SQUID, with on the left with SIS junctions and on the right one with nanobridges. The nanobridges are still thinner than the banks though.

We can however apply a magnetic field, which will give us a symmetry breaking phase acquired by a travelling charged particle in a vector potential.

$$\phi = \frac{q}{\hbar}\int Adl \tag{2.64}$$

Where A is the vector potential, with $\nabla \times A = B$ and both are zero at the same time. Using Stokes theorem, we can find that there is a phase difference between two paths with the same start as endpoint, depending on the flux encircled, the Aharonov-Bohm effect.[1]

$$\Delta\phi = \frac{2e}{\hbar}\oint Adl = \frac{2e\Phi_B}{\hbar} = \frac{2\pi\Phi_B}{\Phi_0} \tag{2.65}$$

Since the magnetic field is zero in the ring itself, due to the Meissner effect[25], there will be a constant phase difference between particles travelling through different arms, independent on the exact path. Since

in a SQUID the junctions themselves only make up a tiny part of the path of the electron, and we know the quantization.

$$\delta_a - \delta_b + \frac{2\pi\Phi_B}{\phi_0} = 2\pi n \tag{2.66}$$

with $n \in \mathbf{Z}$, though this is of course irrelevant for behaviour. δ_b has a negative sign due to the direction of the current going against the clockwise path. Since the junctions are symmetric, the phase jumps should be the same for either side in the absence of a magnetic field, and the average should remain constant, $\delta = \frac{\delta_a+\delta_b}{2}$.

$$I_{SQ}(\Phi_B) = I_c(\sin\delta_b + \sin\delta_a) = 2I_c \sin\frac{\delta_b+\delta_a}{2}\cos\frac{\delta_b-\delta_a}{2} = 2I_c\cos\frac{\pi\Phi_b}{\Phi_0}\sin\delta \tag{2.67}$$

$$L_{SQ}(\Phi_B) = \frac{\mathrm{d}\Phi}{\mathrm{d}I} = \frac{\Phi_0}{4\pi I_c\left|\cos\frac{\pi\Phi_B}{\Phi_0}\right|}\frac{\mathrm{d}\delta}{\mathrm{d}\sin\delta} = \frac{\Phi_0}{4\pi I_c\left|\cos\frac{\pi\Phi_B}{\Phi_0}\right|}\frac{1}{\cos\delta} \tag{2.68}$$

$$E_{pot}(\Phi_B) = I_c\frac{\Phi_0}{\pi}(1-\cos\delta)\left|\cos\frac{\pi\Phi_B}{\Phi_0}\right| \tag{2.69}$$

Without a magnetic field the inductance, and also the capacitance, of the system is exactly half the one of the Josephoson Junction. From now on we will use $I_B = 2I_c\left|\cos\frac{\pi\Phi_B}{\Phi_0}\right|$ to denote the critical current of the SQUID, and $L_B = \frac{\Phi_0}{2\pi I_B}$, others would use for the Josephson energy: $E_B = \frac{\Phi_0 I_B}{2\pi} = \frac{\Phi_0^2}{4\pi^2 L_B}$

Now that we have our non-linear component, we can make it into a Duffing oscillator with a capacitor in parallel, and derive its Hamiltonian in the next subsection.

2.3.6. Hamiltonian

To get to our Duffing oscillator, we will need the Hamiltonian. We will start with the simplest model of our circuit, and get the classical Hamiltonian. This model is the LC circuit, as depicted in figure 2.17. 2.17.

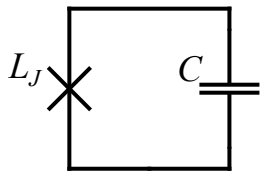

Figure 2.17: Schematic of a LC resonator, with for the inductor the non linear Josephson Junction.

We now have a non-linear inductor, so we need to recalculate the potential energy. Then we can do the same as in subsection 2.37. We will use the reduced flux quantum for clarity $\Phi_R = \frac{\Phi_0}{2\pi}$, so $\delta = \frac{\Phi}{\Phi_R}$.

$$E_{pot} = I_B\Phi_R(1-\cos\delta) \approx I_B\Phi_R\left(1-1+\frac{\Phi^2}{2\Phi_R^2}-\frac{\Phi^4}{24\Phi_R^4}\right) = \frac{1}{L_B}\left(\frac{\Phi^2}{2}-\frac{\Phi^4}{24\Phi_R^2}\right) \tag{2.70}$$

$$\mathscr{L} = E_{kin} - E_{pot} = \frac{C_S\dot{\Phi}^2}{2} - \frac{1}{L_B}\left(\frac{\Phi^2}{2}-\frac{\Phi^4}{24\Phi_R^2}\right) \tag{2.71}$$

$$\mathscr{H}_S = \dot{\Phi}\frac{\partial\mathscr{L}}{\partial\dot{\Phi}} - \mathscr{L} = \frac{C_S\dot{\Phi}^2}{2} + \frac{\Phi^2}{2L_B} - \frac{\Phi^4}{24\Phi_R^2 L_B} \tag{2.72}$$

Now we need to use how the charge is related to the generalized flux to get the equation in the shape of a harmonic oscillator.

$$q = \dot{\Phi}\frac{\partial\mathscr{L}}{\partial\dot{\Phi}} = C_S\dot{\Phi} \tag{2.73}$$

Which results in our non-linear oscillator:

$$\mathscr{H}_S = \frac{q^2}{2C_S} + \frac{\Phi^2}{2L_B} - \frac{\Phi^4}{24\Phi_R^2 L_B} \tag{2.74}$$

2.3.7. Array of SQUIDs

Though using a SQUID in an array instead of a single one as our non-linear inductor results in multiple differences, we are mostly interested in the result that the relative size of the non-linear part of the inductance to the linear inductance becomes smaller. This cannon be achieved by simply tinkering with a single SQUID, and the relative size controls the dynamic range. So now we will put N SQUIDs in series, and assume the phase drop is distributed equally among them, just as the voltage, as seen in figure 2.18

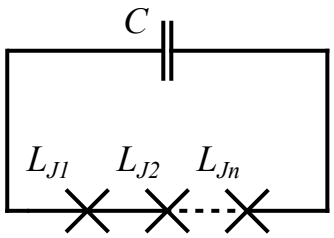

Figure 2.18: Schematic of a LC resonator, with for the inductor an array of Josepson Junctions.

To not change the resonance frequency, the two quadratic terms need to be the same, so we will use $L_{SE}N = L_B$ and $C_{SE}N = C_S$, denoting the inductance and capacitance of each element of the array. Though since we use a parrallel capacitance, its part remains the same by default.

$$\mathcal{H}_{SA} = \sum_{i=0}^{N-1} \frac{Nq^2}{2C_B N^2} + \frac{N}{L_B}\left(\frac{\Phi^2}{2N^2} - \frac{\Phi^4}{24\Phi_0^2 N^4}\right) = \frac{q^2}{2C_B} + \frac{1}{L_B}\left(\frac{\Phi^2}{2} - \frac{\Phi^4}{24\Phi_0^2 N^2}\right) \tag{2.75}$$

We can see that with increasing the amount of SQUIDs or JJ, we can decrease the size of the non-linear term relative to the linear one. This means we can increase the bifurcation power, the power at what the maximum gain can be achieved, and in conjunction the power at which saturation takes place. Also with increasing the power the device can handle with the same quadratic factor, because the critical current also increases with N, which means n_{max} increases with N^2[11].

A more in depth calculation also taking in the capacitance's between the individual SQUIDs and the ground can be found in this paper [28].

2.3.8. Inclusion of linear resonator

Including a linear resonator in series with our SQUID, we can increase the linear inductance without changing the non-linear inductance. This may be important for the tuning behaviour of the resonance frequency, as can be read in 2.4. The circuit can be seen in figure 2.19, and this derivation is based on van der Spek [34].

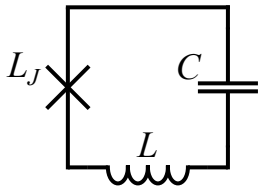

Figure 2.19: Schematic of a LC resonator, with for the inductor a Josephson Junction and a linear inductor.

We start with $\Phi = \Phi_J + \Phi_I$ denoting the generalized flux over the SQUID array and linear inductor respectively. We now use an approximation where the non-linearity is small, and so $\frac{\Phi_J}{L_J} = \frac{\Phi - \Phi_J}{L_I}$, as well as $\Phi_J = \beta\Phi$ for clarity, now, for a single SQUID:

$$E_{pot} = \frac{1}{L_I}\frac{\left(\Phi - \Phi_J\right)^2}{2} + \frac{1}{L_J}\left(\frac{\Phi_J^2}{2} - \frac{\Phi_J^4}{24\Phi_R^2}\right) = \frac{\Phi^2(1-\beta)^2}{2L_I} + \frac{\Phi^2\beta^2}{2L_J} - \frac{\Phi^4\beta^4}{24L_J\Phi_R^2} \tag{2.76}$$

$$\mathcal{L} = E_{kin} - E_{pot} = \frac{C\dot{\Phi}^2\beta}{2} - \frac{\Phi^2(1-\beta)^2}{2L_I} - \frac{\Phi^2\beta^2}{2L_J} + \frac{\Phi^4\beta^4}{24L_J\Phi_R^2} \tag{2.77}$$

$$\mathcal{H} = \dot{\Phi}\frac{\partial\mathcal{L}}{\partial\dot{\Phi}} - \mathcal{L} = \frac{q^2}{2C} + \frac{\Phi^2}{2}\left(\frac{(1-\beta)^2}{L_I} + \frac{\beta^2}{L_J}\right) - \frac{\Phi^4\beta^4}{24\Phi_R^2 L_J} = \frac{q^2}{2C} + \frac{\Phi^2}{2(L_I+L_J)} - \frac{\Phi^4\beta^3}{24\Phi_R^2(L_I+L_J)} \tag{2.78}$$

Where we used $\left(\frac{(1-\beta)^2}{L_I}+\frac{\beta^2}{L_B}\right)=\frac{1}{L_I+L_B}$. Including the use of our array, we use the Hamiltonian:

$$\mathscr{H}=\frac{q^2}{2C}+\frac{\Phi^2}{2(L_I+L_B)}-\frac{\beta^3\Phi^4}{24\phi_R^2(L_I+L_B)N^2}=\frac{q^2}{2C}+\frac{\Phi^2}{2L_f}-\frac{\beta^3\Phi^4e^2}{6\hbar^2L_fN^2}=\frac{q^2}{2C}+\frac{\Phi^2}{2L_f}+K\frac{C\Phi^4}{3\hbar L_f} \tag{2.79}$$

Where $L_f=L_I+L_B$ and $K=-\frac{\beta^3e^2}{2\hbar N^2C}$. If we include the influence of a magnetic field, and the approximations as described in subsection 2.2.5, we can find that is also describes our actual circuit, as seen in figure 2.20.

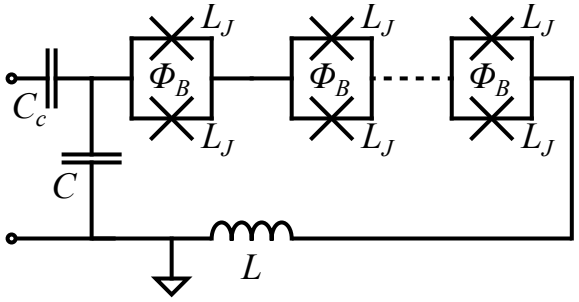

Figure 2.20: Schematic of the lumped element model of our circuit.

2.3.9. Quantization of Hamiltonian

We will quantize the Hamiltonian based on the harmonic operator. Starting from equation 2.79

$$\left[\hat{\Phi},\hat{q}\right]=i\hbar \tag{2.80}$$

$$\hat{\Phi}=\sqrt{\frac{\hbar}{2}\sqrt{\frac{L_f}{C}}}\left(\hat{A}+\hat{A}^\dagger\right) \tag{2.81}$$

$$\hat{q}=-i\sqrt{\frac{\hbar}{2}\sqrt{\frac{C}{L_f}}}\left(\hat{A}-\hat{A}^\dagger\right) \tag{2.82}$$

We can get the quantum mechanical Hamiltonian.

$$\hat{\mathscr{H}}=\frac{\hat{q}^2}{2C}+\frac{\hat{\Phi}^2}{2L_f}+K\frac{C\hat{\Phi}^4}{3\hbar L_f}=-\frac{\hbar}{4\sqrt{CL_f}}\left(\hat{A}-\hat{A}^\dagger\right)^2+\frac{\hbar}{4\sqrt{CL_f}}\left(\hat{A}+\hat{A}^\dagger\right)^2+\frac{\hbar K}{12}\left(\hat{A}+\hat{A}^\dagger\right)^4 \tag{2.83}$$

The first part results in the harmonic oscillator since:

$$\hat{\mathscr{H}}_l=\frac{\hbar}{4\sqrt{CL_f}}\left(2\hat{A}\hat{A}^\dagger+2\hat{A}^\dagger\hat{A}\right)=\frac{\hbar}{2\sqrt{CL_f}}\left(1+2\hat{A}^\dagger\hat{A}\right)=\frac{\hbar}{\sqrt{CL_f}}\left(\frac{1}{2}+\hat{A}^\dagger\hat{A}\right) \tag{2.84}$$

Where $\frac{1}{\sqrt{CL_f}}$ gives the resonance frequency, just as with a Harmonic oscilator. The second part is more complicated, but since we will later apply RWA, we can neglect all terms uneven in $\hat{A}$ or $\hat{A}^\dagger$. Expanding gives:

$$\left(\hat{A}+\hat{A}^\dagger\right)^4=6\hat{A}^\dagger\hat{A}^\dagger\hat{A}\hat{A}+12\hat{A}^\dagger\hat{A}+3 \tag{2.85}$$

The total Hamiltonian is then, while omitting the zero point energy:

$$\hat{\mathscr{H}}=\hbar\left(\frac{1}{\sqrt{CL_f}}+K\right)\hat{A}^\dagger\hat{A}+\frac{\hbar K}{2}\hat{A}^\dagger\hat{A}^\dagger\hat{A}\hat{A} \tag{2.86}$$

Which gives $\omega_0=\frac{1+K\sqrt{CL_f}}{\sqrt{CL_f}}\approx\frac{1}{\sqrt{CL_f}}$, where K is dependent on flux and the amount of elements in the array.

2.4. Magnetic resonance tuning

By using SQUIDS, we can tune the resonance frequency of our JPA, and as previously stated.

$$\omega_0 = \frac{1}{\sqrt{L_{SQ}C}}, \qquad L_{SQ} = \frac{L_J}{2\left|\cos\frac{\pi\Phi_B}{\Phi_0}\right|}\frac{1}{\cos\delta} = \frac{L_J}{2\left|\cos\frac{\pi\Phi_B}{\Phi_0}\right|}\frac{1}{\sqrt{1-\frac{I^2}{I_c^2}}} \tag{2.87}$$

Which would give us an inductance that goes to infinity at flux quantum, and a corresponding frequency that goes to zero. In reality however, this does not happen, and a first step to take this into account is to use some additional inductance. This is because not only do the junctions have inductance, but the loop itself as well, in relation to the surface of the loop. For a circular loop $L \propto 2\mu_0 r \ln 16r$, though the material can also add some.[5] This can also come from small differences between the SQUIDs, or by a SQUID with only one functioning arm, or other faults in design and manufacturing.

$$L = L_I + L_{SQ} \tag{2.88}$$

$$\omega_0(\Phi_B) = \frac{1}{\sqrt{LC}} = \frac{1}{\sqrt{\left(L_I + \frac{L_J}{2\left|\cos\frac{\pi\Phi_B}{\Phi_0}\right|}\right)C}} = \frac{\omega_0(0)}{\sqrt{\Lambda + \frac{1-\Lambda}{2\left|\cos\frac{\pi\Phi_B}{\Phi_0}\right|}}} \tag{2.89}$$

Where $\Lambda = \frac{L_I}{L_{SQ}+L_I}$ denotes the part of the total inductance that is independent on flux[18], a simulation of this can be seen in figure 2.21. As one can see here, increasing Λ will broaden the arcs.

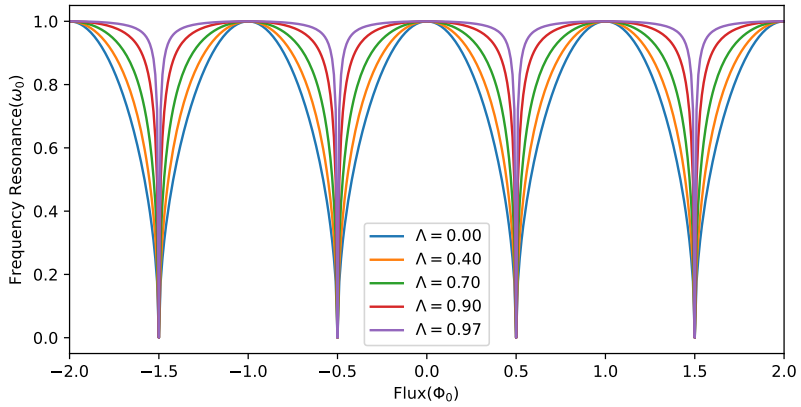

Figure 2.21: Impact of different relations between the linear and non linear inductance on the resonance tuning.

This gets us a lot closer to an experimental shape of a flux arc. In experiments, we can also see "overlapping" flux arcs, resulting in jumps, for that we need to take self-inductance into account. This is caused by the inductance of the loops interfering with the junctions. [33] This means that the flux actually going trough the loop may differ from what is applied.

$$\Phi_x = \Phi_B + LI_c \sin\frac{\pi\Phi_B}{\Phi_0} \tag{2.90}$$

Where Φ_B is the flux tuning our resonance frequency, as before, only now does it differ from the applied flux Φ_x. This can result in hysteresis, and so in the flux jumps, the constraint being:

$$\beta_L \equiv \frac{2L_l I_c}{\Phi_0} = \frac{L_l}{\pi L_J} \leq \frac{2}{\pi} \tag{2.91}$$

Where the results of a couple of simulations can be seen in figure 2.22. At the top, we can see the resonance frequency we measure, with the red and green lines showing what a measurement in either direction would

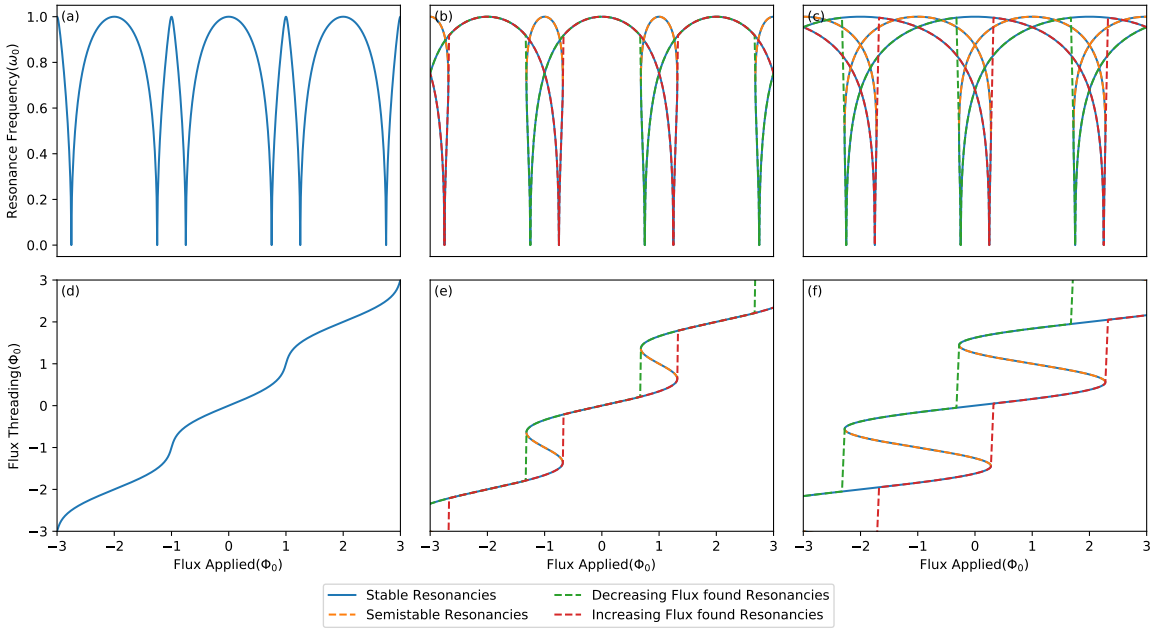

Figure 2.22: Impact of self inductance on the resonance tuning, for $\Lambda = 0.3$. With from left to right, $\beta_L = 0.5$, $\beta_L = 1.5$ and $\beta_L = 3.5$.

show. The source of the hysteresis can be better seen in the bottom row, where applied flux and threading flux is set out against each other.

But still our frequency will go near zero for certain values of flux, and our inductance to infinity. In our case it can flux jump before reaching this state, but even if β_L is small enough, it is not achievable in reality, and so our frequency range is limited, as can be read in Kim et al. [21]. This tells that the relative size of the non-linear capacitance and inductance to the linear capacitance and inductance results in a limit.

2.4.1. Influence of Magnetic flux on non-linearity.

Though the linear inductance has naturally no impact on the value of K in our Hamiltonian, the flux tuning in equation seems to do, as it reduces the non-linear terms of the inductance with the same factor. However in an expression for K, this does not seem to be the case, as long as the fraction β remains to be the same. This means that in the case where $L_{SQ} \gg L_l$, the non-linearity is approximately constant, while in the case of $L_l \gg L_B$, the non-linearity is actually dependent on the third power. This can have drastic impacts, as seen in figure 2.23.

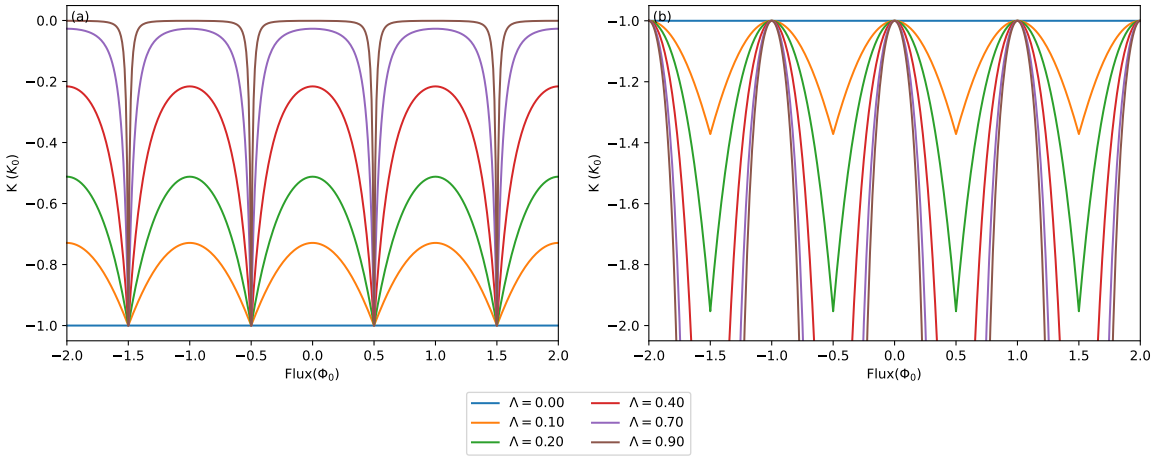

Figure 2.23: Influence of the magnetic flux on the non-linearity for different values of Λ, with on the left normalized to $\Phi = \frac{\Phi_0}{2}$, and on the right normalized to $\Phi = 0$.

If the Λ of a system is not close to zero, the non-linearity will change in size much quicker than the resonance frequency. Looking at systems with different Λ but the same resonance frequency and non-linearity when there is no flux threading the loop, we will arrive at subplot b. This has a secondary impact on the dynamic range at that point.

2.5. JPA

Remember the equation for the inductance of the Jospephson Junction:

$$L_J(\phi) = \frac{\Phi_0}{2\pi \cos\Delta\phi} = \frac{\Phi_0}{I_c\sqrt{1-\frac{I^2}{I_c^2}}} \tag{2.92}$$

With ϕ being the generalized flux, and $I_c \equiv \frac{2eE_j}{\hbar}$ being the critical current of the junction. There are still two ways to use this, one is by changing the magnetic flux through a loop with two symmetric Josephson Junctions, a SQUID, as that will alter the current, which will result in $L \approx L_J\left(1+\frac{I(t)}{I_0}\right)$.

Where I_c depends on the SQUID loop, the dependence of the inductance on the current is linear, and thus it will result in three wave mixing. The way used in the device of researched in this project changes just by using an AC-current, we can just use a Taylor expansion: $L \approx L_J\left(1+\frac{1}{2}\left(\frac{I(t)}{I_C}\right)^2\right)$

Since this is quadratic, this will result in four wave mixing. Together with a capacitor this will make an LC circuit with a parametric inductance. The quantum mechanical Hamiltonian is calculated in the previous section:

$$\hat{\mathscr{H}} = \hbar\omega_0 \hat{A}^\dagger \hat{A} + \frac{\hbar K}{2}\hat{A}^\dagger\hat{A}^\dagger\hat{A}\hat{A} \tag{2.93}$$

With in our circuit, as seen in figure 2.20.

$$\omega_0 = \frac{1}{\sqrt{L_l + \frac{L_{SQ}}{2\cos\frac{\pi\Phi_B}{\Phi_0}}(C+C_c)}} \qquad K = -\frac{e^2}{2\hbar N^2(C+C_c)}\left(\frac{L_{SQ}}{L_l\cos\frac{\pi\Phi_B}{\Phi_0}+L_{SQ}}\right)^3 \tag{2.94}$$

Where the last term will result in the non-linear behaviour, which is what we need for a parametric amplifier. The coming derivation follows [39] or [11], the difference between the two mainly being that the first assumes that there is a significant contribution to the nonlinear dissipation. A solution can be found for this equation, coming from input output theory.[14]

$$\dot{A} = -i\omega_0 A - iKA^\dagger AA - \frac{\kappa+\gamma}{2}A + \sqrt{\kappa}A_{in}(t) + \sqrt{\gamma}b_{in}(t) \tag{2.95}$$

Here A is the solution for the inner field, κ is the coupling to the input line, and γ is the coupling to the bath, the dissipation. This equation works for the stiff pump approximation, which assumes that signal or noise is of negligible influence on the resonator state. This breaks down if the signal or vaccuum fluctations term become significant! For now we look at the response to a classical pump, so only for a single frequency. Using input output theory we come to the following equation:[38]

$$A_{out}(t) = A_{int}(t) - \sqrt{\kappa}A(t) \tag{2.96}$$

Which differs from Eichler and Wallraff [11] by A_{out} having a different sign due to the fact that our device is capacitively coupled, resulting in an open off resonance. Now we will apply the rotating wave approximation, which neglects higher order frequencies.[15] This is done in the negative pump frequency $-\omega_p$.

$$A(t) = \alpha e^{-i\omega_p t} \tag{2.97}$$

$$A_{in}(t) = \alpha_{in} e^{-i\omega_p t} \tag{2.98}$$

$$A_{out}(t) = \alpha_{out} e^{-i\omega_p t} \tag{2.99}$$

Putting that in the previous equation gives:

$$i(\omega_0-\omega_p)\alpha+\frac{\kappa+\gamma}{2}\alpha+iK\alpha^2\alpha^*=\sqrt{\kappa}\alpha_{in} \tag{2.100}$$

And multiplying that with its complex conjugate gives:

$$\kappa|\alpha_{in}|^2=|\alpha|^2\left((\omega_0-\omega_p)^2+\frac{(\kappa+\gamma)^2}{4}\right)+|\alpha|^4 2(\omega_0-\omega_p)K+|\alpha|^6K^2 \tag{2.101}$$

Which gives us a cubic relation in $|\alpha^2|$, the photon number. We can use $\omega_\delta=\omega_p-\omega_0$ and multiply by K to see that the K and $|\alpha_{in}^2|$ cannot be found separately by looking at the JPA's behaviour:

$$\kappa K|\alpha_{in}|^2=K|\alpha|^2\left(\omega_\delta^2+\frac{(\kappa+\gamma)^2}{4}\right)-K^2|\alpha|^4 2\omega_\delta+K^3|\alpha|^6 \tag{2.102}$$

One can reduce it further to show that the whole thing only depends on three dimensionless parameters, as can be seen in Eichler and Wallraff [11]. Using:

$$\delta\equiv\frac{\omega_\delta}{\kappa+\gamma},\qquad \tilde{\alpha}_{in}\equiv\frac{\sqrt{\kappa}\alpha_{in}}{\kappa+\gamma},\qquad \xi\equiv\frac{|\tilde{\alpha}_{in}|^2K}{\kappa+\gamma},\qquad n\equiv\frac{|\alpha|^2}{|\tilde{\alpha}_{in}|^2} \tag{2.103}$$

Standing for the reduced detuning, reduced driving amplitude, power multiplied by nonlinearity and the relative photon number respectively. This results in:

$$1=\left(\delta^2+\frac{1}{4}\right)n-2\delta\xi n^2+\xi^2n^3 \tag{2.104}$$

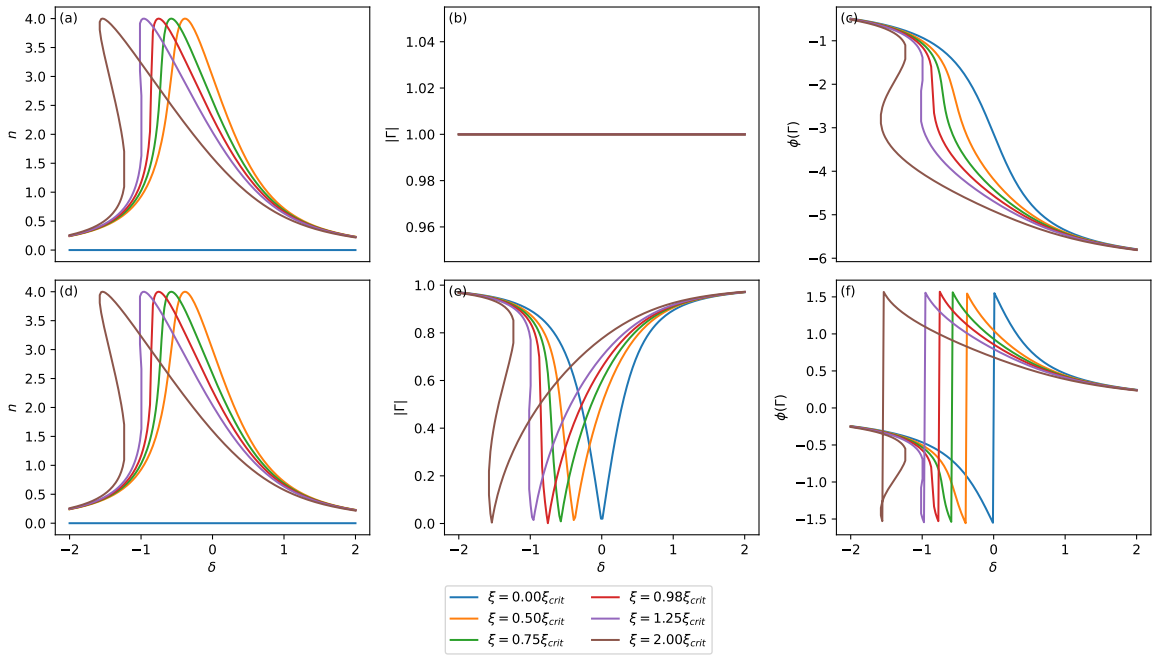

Figure 2.24: Simulated response of the JPA, with on the left the absolute magnitude, the middle the phase and on the right the photon number. This is done for on the top row $\kappa=0.1\omega_0,\gamma=0$ and on the bottom row with $\kappa=0.05\omega_0,\gamma=0.05\omega_0$.

Note that it has the same shape as the equation in the classical section, main difference being that the ω's are not squared here, also different, its dependence on ω in the last term with the Duffing oscillator. A simulation of this can be seen in the right column of figure 2.24. We can see that the relative photon number has a maximum of four, independent on power, and that for increasing power the peak slopes sideways. If we would have a positive K it would slope to positive frequencies. At critical power, the bifurcation power, the left side becomes vertical, and beyond it will have three solutions for some frequencies. Two of these are stable

and one is semi-stable, and cannot be reached by just sweeping left or right in pump frequency. Another thing is between the rows one can see that the photon number is independent on the relation between κ and γ.

When $\frac{\partial n}{\partial \delta} = 0$ the maximum photon number is achieved, we can find this by taking the derivative of the previous equation with respect to delta. This happens when:

$$\delta = \xi n \tag{2.105}$$
$$\delta = 4\xi \tag{2.106}$$

There are two points where $\frac{\partial \delta}{\partial n} = 0$, if the input amplitude is above the critical point, or one at the critical point. These points notate the location of the jumps due to hysteris:

$$0 = \left(\delta^2 + \frac{1}{4}\right) - 4\delta\xi n + 3\xi^2 n^2 \tag{2.107}$$

together with equation 2.104. Together they result in an equation with no analytical solution, but they can be found numerically. The critical point can be found by looking for the moment there is only one equation, or $\frac{\partial^2 \delta}{\partial^2 n} = 0$ is also true.

$$4\delta\xi = 6\xi^2 n \tag{2.108}$$

This gives critical values of:

$$\delta_{crit} = -\frac{\sqrt{3}}{2} \tag{2.109}$$
$$\xi_{crit} = -\frac{1}{\sqrt{27}} \tag{2.110}$$

Which is not the point at the largest relative photon number, as $\delta_{crit} \neq 4\xi_{crit}$, these can also be seen in the right column of 2.24.

Now onto the reflection $\Gamma = \frac{\alpha_{out}}{\alpha_{int}}$, which can be found by combining equation 2.96 and 2.100. This gives:

$$\Gamma = 1 - \frac{\kappa}{\kappa+\gamma}\frac{1}{\frac{1}{2} - i\delta + i\xi n} = \frac{\gamma - \kappa - 2i\omega_\delta + 2iK|\alpha|^2}{\gamma + \kappa - 2i\omega_\delta + 2iK|\alpha|^2} \tag{2.111}$$

Which is save for the Kn the same solution as our classical one, although it is also its complex conjugate, probably due to our choice of negative frequency earlier. Using its complex conjugate, we get the result in the left and middle column of figure 2.24. Here the left shows the absolute magnitude, while in the middle the phase is visible. When $\xi = 0$ it behaves exactly like a normal resonator, but when ξ is increased is slopes sideways, at the bifurcation power the phase shift becomes vertical, and for the critical coupled cavity the magnitude also gets a vertical slope. When $\gamma = 0$ the magnitude is independent on power and always 1, and the dips depth is also independent on ξ. We can also see that the overcoupled device keeps it 2π phase shift in subplot b, while the critically coupled device keeps its 1π phase shift.

2.5.1. Pumped JPA

When we pump the JPA, we add a variable to our input and output signals, like so:

$$A(t) = (a(t) + \alpha)e^{-i\omega_p t} \tag{2.112}$$
$$A_{in}(t) = (a_{in}(t) + \alpha_{in})e^{-i\omega_p t} \tag{2.113}$$
$$A_{out}(t) = (a_{out}(t) + \alpha_{out})e^{-i\omega_p t} \tag{2.114}$$

Putting that in the equation 2.95.

$$\begin{aligned}&\dot{a} + i(\omega_0 - \omega_p)(\alpha + a) + \frac{\kappa+\gamma}{2}(\alpha + a) - \sqrt{\kappa}(\alpha_{in} + a_{in}) - \sqrt{\gamma}b_{in} = \\ &-iK\left(\alpha^2\alpha^* + 2a\alpha\alpha^* + \alpha^2 a^\dagger + 2a\alpha a^\dagger + a^2\alpha^* + a^2 a^\dagger\right)\end{aligned} \tag{2.115}$$

Now if we use a stiff pump approximation, there are a lot of terms that can be safely neglected, only terms that are at most linear in a will remain. Next we will use a Fourier composition.

$$a(t) \equiv \frac{\kappa+\gamma}{\sqrt{2\pi}} \int_{-\infty}^{\infty} a_\Delta e^{-i\Delta(\kappa+\gamma)t} d\Delta \tag{2.116}$$

Where Δ relates to the difference in reduced pump and signal frequency, giving us:

$$0 = \left(i(\delta - 2\xi n + \Delta) - \frac{1}{2}\right) a_\Delta - i\xi n e^{2i\phi} a^\dagger_{-\Delta} + \tilde{c}_{in,\Delta} \tag{2.117}$$

Where $\tilde{c}_{in,\Delta} \equiv \frac{\sqrt{\kappa}a_{in,\Delta}+\sqrt{\gamma}b_{in,\Delta}}{\kappa+\gamma}$ and $\alpha = |\alpha|e^{i\phi}$

Where ϕ is the internal phase. In conjunction with the equation of $\tilde{c}_{in,-\Delta}$ we can find a steady state solution.

$$\tilde{a}_{out,\Delta} = g_{S,\Delta} a_{in,\Delta} + g_{I,\Delta} a^\dagger_{in,-\Delta} + \sqrt{\frac{\gamma}{\kappa}}(g_{S,\Delta}+1) b_{in,\Delta} + \sqrt{\frac{\gamma}{\kappa}} g_{I,\Delta} b_{in,\Delta} \tag{2.118}$$

With $g_{S,\Delta}$ being the gain from that frequency and to that frequency, while $g_{I,\Delta}$ is the gain to that frequency from the frequency opposite to the pump frequency.

$$g_{S,\Delta} = 1 - \frac{\kappa}{\kappa+\gamma} \frac{i(\delta - 2\xi n - \Delta) + \frac{1}{2}}{-\Delta^2 - i\Delta + \frac{1}{4} + \delta^2 - 4\delta\xi n + 3\xi^2 n^2} \tag{2.119}$$

$$g_{I,\Delta} = \frac{\kappa}{\kappa+\gamma} \frac{i\xi n e^{-2i\phi}}{-\Delta^2 - i\Delta + \frac{1}{4} + \delta^2 - 4\delta\xi n + 3\xi^2 n^2} \tag{2.120}$$

Where the denominator aside from the Δ equals equation 2.107, which makes sense, as the gain should explode for these frequencies. One can also see that $g_{I,\Delta} = g^*_{I,-\Delta}$, while for the signal gain, this is not the case, due to the asymmetry of the reflection. The influence of Δ and δ together is graphed in the appendix, but in figure 2.25 we show the impact of ξ when the system is ideally pumped.

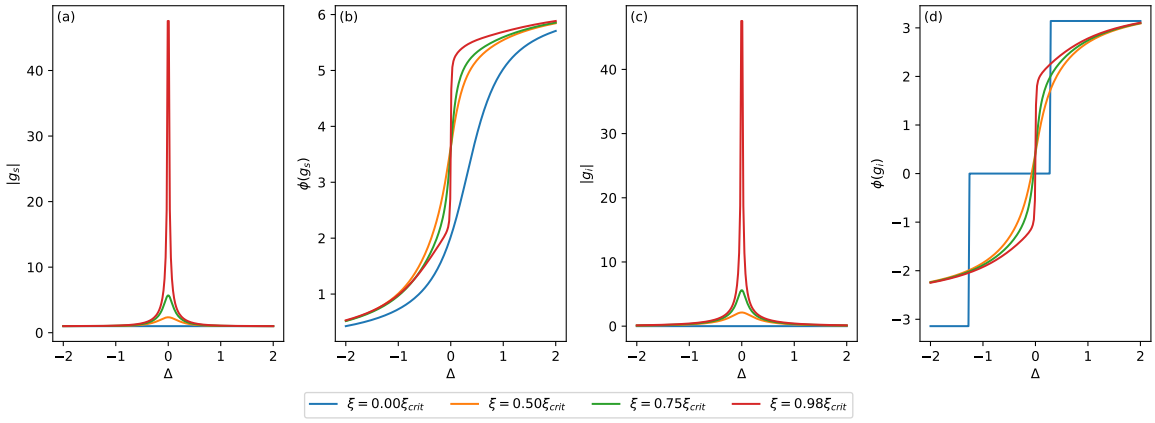

Figure 2.25: Simulated signal response of the JPA, for different settings of ξ, but with ideal δ. From left to right, signal gain magnitude, signal gain phase, signal idler magnitude and signal idler phase. Note that the idler phase gets an offset due to the internal phase.

When $\gamma = 0$,

$$G_\Delta \equiv \left|g_{S,\Delta}\right|^2 = \left|g_{I,\Delta}\right|^2 + 1 \tag{2.121}$$

2.5.2. Power saturation

We discarded the non-linear terms of equation 2.115, but for larger signal amplitudes this approximation will no longer be valid. In that case, the signal will influence the photon number in the amplifier significantly. This means that more parts have to be taken into account. In fact, there will then no longer be four wave mixing and the stiff pump approximation will break down.

In Eichler and Wallraff [11] they use a mean field approach to calculate the result and find a decrease in amplification. Since the stiff pump approach is valid as long as the pump power is much larger than the

signal power, but the critical power for the pump is constant, to expand the dynamic range one would need to increase the critical pump power, which is what they indeed find:

$$G \propto \left(\frac{P_{out}\kappa}{P_p K} \right)^2 \tag{2.122}$$

So one can increase the dynamic range by decreasing the non-linearity, as $\frac{K}{\kappa}$

2.6. Microwave calibration theory

There are multiple ways to Calibrate, each with there own pros and cons.[30] We have a couple of things to consider. First, the JPA will be in a fridge, the He7 as described in section 9.3.1, operated at mK temperatures, so we cannot change parts within the system one after another, we need to use a switch so we can use multiple loads, but it is still limited, in our case six, including the device. Secondly we have a reflection cavity, so we do not need to measure a through. We do use a different in and output line though, but as it turns out, this is not a problem, as it can still be modeled as a reflection cavity, as can be read in subsection 9.2.1 and 9.2.2. Due to these considerations and its simplicity, we decided to go for a Short Open Load(SOL) calibration.

2.6.1. Reflection cavity

The reflection of a component attached to a transmission line is given as such:

$$\Gamma = \frac{Z_L - Z_0}{Z_L + Z_0} \tag{2.123}$$

Now we have three samples, the first one being the Short. The signal will not have any resistivity here, so everything is transferred to the ground, as the impedance is zero. This will make all voltage differences have an opposite sign, and will thus invert the wave. The second one, the open, makes sure the signal cannot pass through, it is entirely reflected, or one could say its impedance is infinite. The final one is the load, which can either be matched so the reflection is zero, or just a value of the order of the input impedance. These impedance will result in this for the reflection coefficient.

$$\Gamma_s = -1 \qquad Z_s = 0 \tag{2.124}$$

$$\Gamma_o = 1 \qquad Z_o = \tag{2.125}$$

$$\Gamma_l = 0 \qquad Z_l = Z_0 \tag{2.126}$$

This tactic heavily relies on these values to be ideal, and what that may mean for experiments is discussed later. We do not measure this directly however, as there can be for example interference in the system. For a single port, every combination of electrical components can be modeled as such:

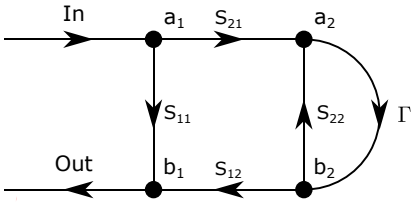

Figure 2.26: Simple model for Reflection Cavity

With some basic linear algebra one can find that the measured reflection Γ' depends on the system and the actual reflection as:

$$\Gamma' = S_{11} + \frac{S_{21}S_{12}\Gamma}{1 - S_{22}\Gamma} \tag{2.127}$$

Measuring the short, open and load will give information about this system in the following way:

$$\Gamma'_s = S_{11} - \frac{S_{21}S_{12}}{1+S_{22}} \tag{2.128}$$

$$\Gamma'_o = S_{11} + \frac{S_{21}S_{12}}{1-S_{22}} \tag{2.129}$$

$$\Gamma'_l = S_{11} \tag{2.130}$$

We now have enough information to calibrate this system, due note that here one can see that the importance of the fact that the load are ideal.

$$S_{11} = \Gamma'_l \tag{2.131}$$

$$S_{22} = \frac{\Gamma'_o + \Gamma'_s - 2\Gamma'_l}{\Gamma'_o - \Gamma'_s} \tag{2.132}$$

$$S_{21}S_{12} = \frac{2(\Gamma'_l - \Gamma'_s)(\Gamma'_o - \Gamma'_l)}{\Gamma'_o - \Gamma'_s} \tag{2.133}$$

Using this information we can get the actual reflection from the measured one:

$$\Gamma_{DUT} = \frac{\Gamma'_{DUT} - S_{11}}{S_{21}S_{12} + S_{22}(\Gamma'_{DUT} - S_{11})} = \frac{(\Gamma'_o - \Gamma'_s)(\Gamma'_{DUT} - \Gamma'_l)}{\Gamma'_{DUT}(\Gamma'_o + \Gamma'_s - 2\Gamma'_l) + \Gamma'_l(\Gamma'_o + \Gamma'_s) - 2\Gamma'_s\Gamma'_o} \tag{2.134}$$

Now for the complex amplitudes, A_1 and A_4 are known, however the others will not, and as our element is non-linear, there is still an unknown:

$$A_2 = \frac{S_{21}}{1 - S_{22}\Gamma} \tag{2.135}$$

$$A_3 = \frac{S_{21}\Gamma}{1 - S_{22}\Gamma} \tag{2.136}$$

This could mean that we cannot know what the critical power for our JPA is exactly.

2.6.2. Differing pathlengths

Though we could use a calibration kit with calibrated pathlengths, others that do not have calibrated pathlengths might be more practical in the fridge. We usually know how much their paths differ though, and beyond that the standards are still the same. We take the reference plane at the edge of the switch.

$$Z(l) = Z_0 \frac{Z_L + Z_0 \tanh \gamma l}{Z_0 + Z_L \tanh \gamma l} \tag{2.137}$$

Where l is the optical length, the length the path would be if the waves would travel with the speed of light.

$$\Gamma_A = \frac{(Z_L - Z_0)\left(1 - \tanh \gamma l\right)}{(Z_L + Z_0)\left(1 + \tanh \gamma l\right)} = \Gamma_L e^{-2\gamma l} \tag{2.138}$$

$$\Gamma_s(l_s) = -e^{-2\gamma l_s} \tag{2.139}$$

$$\Gamma_o(l_o) = e^{-2\gamma l_o} \tag{2.140}$$

If we assume a lossless transmission line, it will become slightly simpler:

$$e^{-2\gamma l} \approx e^{-2i\beta l} = e^{\frac{-2il\omega}{c}} \tag{2.141}$$

This may no longer be valid for longer wires, as wires usually have some loss, so in that case we do use loss, though the actual coefficients have to be found.

$$\gamma l = \frac{(i\omega + \alpha)\, l}{c} \tag{2.142}$$

This will mean that our previous equations in 2.6.1 are not suitable anymore, so we will redo some of the math:

$$\Gamma'_s = S_{11} - \frac{S_{21}S_{12}e^{-2\gamma l_s}}{1+S_{22}e^{-2\gamma l_s}} = S_{11} - \frac{S_{21}S_{12}}{e^{2\gamma l_s}+S_{22}} \tag{2.143}$$

$$\Gamma'_o = S_{11} + \frac{S_{21}S_{12}e^{-2\gamma l_o}}{1-S_{22}e^{-2\gamma l_o}} = S_{11} + \frac{S_{21}S_{12}}{e^{2\gamma l_o}-S_{22}} \tag{2.144}$$

$$\Gamma'_l = S_{11} \tag{2.145}$$

This already shows that we cannot simply deal with this change by applying a phase change to our measurement to get the previous. This is due to the bypass remaining the same, and the interference being heavily dependent on this phase.

$$S_{11} = \Gamma'_l \tag{2.146}$$

$$S_{22} = \frac{\Gamma_s(l_s)\left(\Gamma'_o-\Gamma'_l\right)-\Gamma_o(l_o)\left(\Gamma'_s-\Gamma'_l\right)}{\Gamma_o(l_o)\Gamma_s(l_s)\left(\Gamma'_o-\Gamma'_s\right)} \tag{2.147}$$

$$S_{21}S_{12} = \frac{\left(\Gamma_o(l_o)-\Gamma_s(l_s)\right)\left(\Gamma'_o-\Gamma'_l\right)\left(\Gamma'_s-\Gamma'_l\right)}{\Gamma_o(l_o)\Gamma_s(l_s)\left(\Gamma'_o-\Gamma'_s\right)} \tag{2.148}$$

$$\Gamma_{DUT} = \frac{\Gamma'_{DUT}-S_{11}}{S_{22}\left(\Gamma'_{DUT}-S_{11}\right)+S_{21}S_{12}} \tag{2.149}$$

$$= \frac{\left(\Gamma'_{DUT}-\Gamma'_l\right)\Gamma_o(l_o)\Gamma_s(l_s)\left(\Gamma'_o-\Gamma'_s\right)}{\left(\Gamma'_{DUT}-\Gamma'_l\right)\left(\Gamma_s(l_s)\left(\Gamma'_o-\Gamma'_l\right)-\Gamma_o(l_o)\left(\Gamma'_s-\Gamma'_l\right)\right)+\left(\Gamma_o(l_o)-\Gamma_s(l_s)\right)\left(\Gamma'_o-\Gamma'_l\right)\left(\Gamma'_s-\Gamma'_l\right)} \tag{2.150}$$

Though now also loads differing from open and short would be sufficient for calibration, which may be practical for experimental problems coming from the fact that our loads are not ideal. We may also have to account for our imperfect matched load.

2.6.3. JPA internal reflection

The JPA amplification results not only in the amplification of the probe, but also in an idler which frequency is mirrored from the probe around the pump. This is problematic for our calibration, as the probe could be transformed to a signal at the idler frequency, which can be transformed to a signal at the probe frequency. This path is not foreseen by the calibration, and since these proportions are unknown, we are not able to calibrate this out. To get an idea, we can follow both paths by using equation 2.127. For definitions:

$$a_2 = \begin{bmatrix} a_{2,p} \\ a_{2,i} \end{bmatrix} = S_{11}a_1 = \begin{bmatrix} S_{21,p} & 0 \\ 0 & S_{21,i} \end{bmatrix}\begin{bmatrix} a_{1,p} \\ a_{1,i} \end{bmatrix} \tag{2.151}$$

$$b_2 = \Gamma a_2 = \begin{bmatrix} \Gamma_{p,p} & \Gamma_{p,i} \\ \Gamma_{i,p} & \Gamma_{i,i} \end{bmatrix} a_2 \tag{2.152}$$

All S matrices are diagonal, as they do not mix, while the device should do this only when pumped. Equation 2.127 with matrices:

$$\Gamma' = S_{11} + S_{12}\Gamma\left(I - S_{22}\Gamma\right)^{-1}S_{21} \tag{2.153}$$

Although we can find all the values for the S matrices with our calibration, we will still not be able to quantify this behaviour, as we have four unknowns, and only two equations. With our SA measurements, we do have these four equations, but since we only measure magnitude, part of the information is lost. Whether this feedback loop is constructive or destructive is controlled by the phase, so with only magnitude measurements we only know an upper or lower bound.

If one was interested in calibrating this out, one needs to measure the transmission from probe to idler and the reverse. This could in practice be done by using a mixer for the VNA.

2.7. Noise

All resistance generates noise, dependent on temperature. Classically this is Nyquist[26] noise in resistors, which results in white noise, which means the averaged power is distributed uniformly over frequency.

$$P = k_B T \Delta f \tag{2.154}$$

This also gives us the formula to translate noise power to noise temperature, which is clear to compare to the temperatures in the fridge. In an ideal transmission line, this would mean that the noise remains constant over the wire. In fact, even with resistance added, the attenuation adds as much noise as it takes away, as long as the starting noise is Nyquist noise of the same temperature. If the load attached to the transmission line is at a different temperature, the noise approaches the noise temperature of the wire.

But this is no longer the case if the transmission line is impedance matched at its ends, otherwise the noise can go below the Nyquist noise, since not all of it gets transmitted at all frequencies.

These complications mean that when measuring, wires will add uncertainty, and our measurement is a lower limit. Now active components can add non white-noise above the noise temperatures, while loads connected by impedance mismatched transmission lines go below this limit.

However, the power of noise does not follow the Nyquist noise formula at low temperatures, otherwise we would have no energy at zero temperature. Noise at low temperatures with quantum mechanics in mind come to this:[8]

$$P = \int_{\Delta f} \frac{hf}{e^{\frac{hf}{k_B T}} - 1} + \frac{hf}{2} \tag{2.155}$$

If one takes the classical limit we can do a taylor expansion.

$$\lim_{\frac{hf}{k_B T} \to 0} P \approx \int_{\Delta f} \frac{hf}{1 + \frac{hf}{k_B T} - 1} = \int_{\Delta f} k_B T = k_B T \Delta f \tag{2.156}$$

The other limit at low temperature or high frequency will result in:

$$\lim_{\frac{hf}{k_B T} \to \infty} P \approx \int_{\Delta f} \frac{hf}{2} \approx \frac{hf}{2} \Delta f \tag{2.157}$$

Where this refers to the zero point energy. A graph of the transition can be seen in figure 2.27.

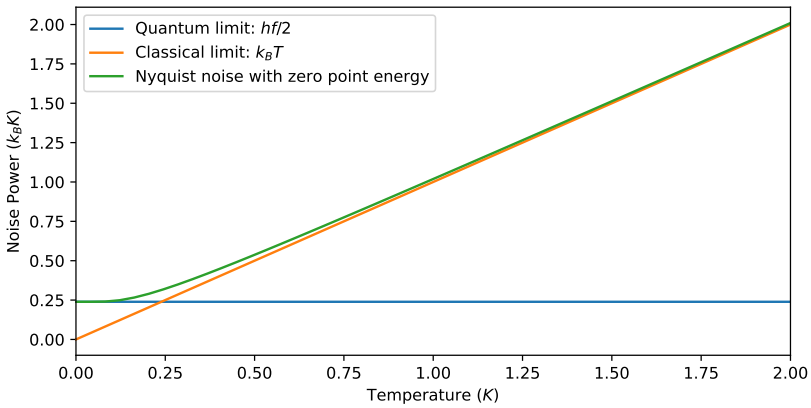

Figure 2.27: Transition from the classical regime to the quantum regime, in the noise power per bandwidth dependence on temperature.

2.7.1. Amplifier noise

Regular amplifiers are active components, and therefore add noise, on top of the noise they add through amplification. This can be described as such:

$$P_{out} = A_{amp}\left(P_{input} + P_{in}\right) \tag{2.158}$$

Where the P_{input} is called the input noise, A_{amp} the amplification factor, P_{in} the ingoing power, and P_{out} the outgoing power. This can also be defined outside the amplification, though the noise temperature will be much higher. In a sequence of amplifiers, the first one usually dominates the outgoing noise. Adding two in sequence and using N for input noise we find:

$$P_{out} = A_2 (N_2 + A_1 (N_1 + P_{in})) = A_2 A_1 (P_{in} + N_1) + A_2 N_2 = A_{tot} (N_{tot} + P_{in}) \tag{2.159}$$

Where the input noise of the entire amplifier chain $N_{tot} = N_1 + N_2 / A_1$ and $A_{tot} = A_2 A_1$. This means that the input noise of the first amplifier is critical to achieve a low Signal to Noise Ration(SNR) later on. This is where the JPA comes in, as it is entirely reactive. One could think that then its input noise would be zero, but since our JPA is a mixer, it will add the noise at the other frequency, as per equations 2.119.

$$\begin{aligned} P_{out}(\omega_p + \Delta) &= A_{JPA}(\omega_p + \Delta) P_{in}(\omega_p + \Delta) + A_{JPA}(\omega_p - \Delta) P_{in}(\omega_p - \Delta) \\ &= A_{JPA}(\omega_p + \Delta) P_{in}(\omega_p + \Delta) + (A_{JPA}(\omega_p + \Delta) - 1) P_{in}(\omega_p - \Delta) \end{aligned} \tag{2.160}$$

So the input noise is not linear, though one can still get an expression from it, with approximation for high power.

$$N_{JPA} = \frac{A_{JPA}(\omega_p + \Delta) - 1}{A_{JPA}(\omega_p + \Delta)} P_{in}(\omega_p - \Delta) \approx P_{in}(\omega_p - \Delta) \tag{2.161}$$

And since the noise at the idler frequency is quantum limited to $\frac{hf}{2}$, so is the minimal value of N_{JPA}. A flux pumped JPA would not have this problem, as it is not a four wave mixer and does not add the idler noise to the output, but it is dependent on flux noise. At higher temperatures, a current pumped JPA would no longer have an advantage over other types of low noise amplifiers, as the noise added is the Nyquist noise at that temperature.

2.7.2. Squeezing

However, utilizing the mixer properties, we can also reduce the noise at specific frequencies, even below the Quantum Noise limit, which is called squeezing. This is done by phase locking the input at the idler and signal frequencies, so the noise they carry cancels.[39] [2] The JPA is in this case used as a noiseless mixer, akin to a partial passable mirror.[15]

3

Methods

3.1. Reflection measurement

The theory of the JPA is written in the basis of transmission parameters, we know how it amplifies or attenuates and adds a certain phase, as described in section 2.5. The reflection depends on the signal frequency and power, in addition to a magnetic field. These three variables could be sweeped to get insight in the properties defining the JPA, as described in 2.5.

The magnetic field only needs to be generated, but to get the transmission we also need to measure at these frequencies. The most straightforward way to measure this, is with a Vector Network Analyzer(VNA), we use a Keysight E5080A, though the basic workings are described in Schwarz [31]. The idea is simple, instead of having a source and measuring the incoming voltage and current, we send out a signal with a specific frequency, and then measure only at that frequency. We can then sweep this frequency to get the reflection behaviour of our device. This way we can also get a clear picture of the phase, since the phase added by (ideal) transmission lines is linear with frequency, we can remove this to get a clear view of the phase shifts of our cavity.

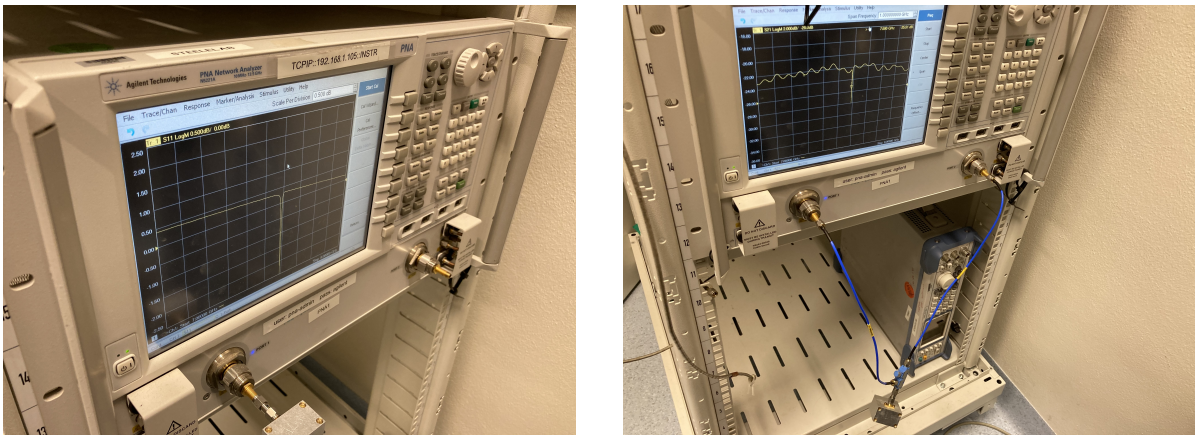

Figure 3.1: On the left one can see an S_{11} measurement with the VNA of the aluminium cavity, at the bottom. The magnitude plot depicted on screen is a flat line with a lorentzian. On the right the same cavity is measured with an S_{21} measurement, in between there is a directional coupler connecting the cavity, the ingoing and outgoing line. The magnitude plot shows some cable resonances now.

We do however have to deal with the technical limitations of our equipment, digitizing at GHz directly is simply not feasible, because the measurement period would be on the order of nanoseconds. Instead, the VNA digitizes at a fixed intermediate frequency(IF), and follows the heterodyne prinicple., as can be seen in figure 3.2.

To get the signal at that frequency, it demodulates using a mixer and the local oscillator. For the comparison needed to get transmission values, this procedure is used on both the input and the output signal after a bandpass filter. The heterodyne tactic may result in the a contribution from the image frequency, as derived

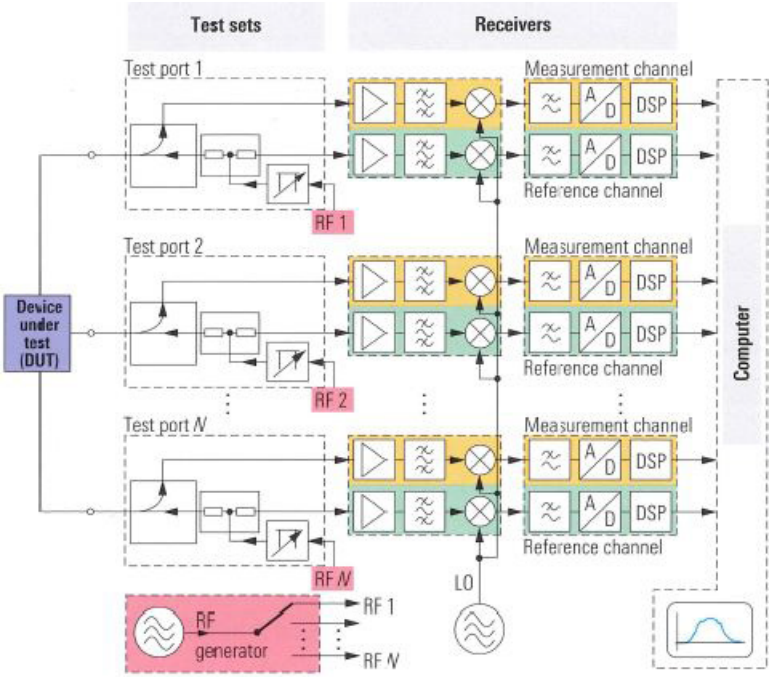

Figure 3.2: Schematic of an n port vector network analyzer, taken from Schwarz [31].

below. We start with our signal and our local oscillator:

$$v_{IS} = A\cos(\omega_S t + \phi_S) \qquad v_{LO} = B\cos(\omega_{LO} t + \phi_{LO}) \tag{3.1}$$

Where $f_{IF} = |f_S - f_{LO}|$, or $\omega_{IF} = |\omega_S - \omega_{LO}|$. A mixer can be idealized as a device that multiplies the two input signals to its output:

$$v_M = v_{IS} v_{LO} = \frac{AB}{2}\left(\cos(\omega_S t + \phi_S + \omega_{LO} t + \phi_{LO}) + \cos(\omega_S t + \phi_S - \omega_{LO} t - \phi_{LO})\right) \tag{3.2}$$

$$v_F = \frac{AB}{2}\cos(\omega_S t + \phi_S - \omega_{LO} t - \phi_{LO}) \tag{3.3}$$

Where only the second term of equation 3.2 will pass the lowpass filter, which is then digitized. To get rid of noise there is instead a band filter, with a variable frequency range, the intermediate frequency bandwidth, or IFBW. As most noise is evenly distributed, it is inversely related with the IFBW. However, smaller bandwidths result in longer measurement times, as the bandwidths position needs to be changed more often, which is usually the dominant contribution to measurement time. We should still keep the bandwidth smaller than the distance between our sweep points, as otherwise the different points can share contributions, in the case of non-linearity's.

To see that a signal at the image frequency, we can instead use the frequency $\omega_P = 2\omega_{LO} - \omega_S$, and see that it gives the exact same result if we put that in equation 3.2, as $\cos(2\omega_{LO} t - \omega_S t - \omega_{LO} t) = \cos(\omega_{LO} t - \omega_S t) = \cos(\omega_S t - \omega_{LO} t)$

3.1.1. Pumped reflection measurement

Our JPA is current pumped, so an additional signal is used to power the device. We now have a five parameter system, with pump power and frequency, probe power and frequency, and magnetic field. Though signal power is no longer relevant for the gain, as only the relative amplitude of it and pump is important. We can use theory and measurement to look for high gain manually, as looking for it in broad sweeps is unfeasable due to the amount of free parameters and the sensitivity of the behaviour, as it is part of a phase change. We can in addition get a broader idea of the gain behaviour by doing these sweeps, but we will have to take due with less gain.

However, the VNA is build around the idea that all it measures is noise, and an altered version of its output signal. Now that we have added a signal generator to our setup though, as can be seen in 4.3, this no longer

holds. One could expect just a spike with a random phase at the pump frequency, but it is actually worse than that. It now also becomes relevant that our mixer is non-ideal, though previously additional contribution would be removed by the filter, this is no longer the case. Let us look again at equation 3.1, and redo the math. Here we use $\alpha = \omega t + \phi$ for clarity.

$$v_{IS} = A\cos(\alpha_S) + C\cos(\alpha_P) \tag{3.4}$$

$$v_{LO} = B\cos(\alpha_{LO}) \tag{3.5}$$

$$\begin{aligned} v_M &= (v_{IS} + v_{LO})^2 = A^2\cos(\alpha_S)^2 + B^2\cos(\alpha_{LO})^2 + C^2\cos(\alpha_P)^2 \\ &\quad + 2AB\cos(\alpha_S)\cos(\alpha_{LO}) + 2AC\cos(\alpha_S)\cos(\alpha_P) + 2BC\cos(\alpha_{LO})\cos(\alpha_P) \\ &= \frac{1}{2}\left(A^2 + B^2 + C^2 + A^2\cos(2\alpha_S) + B^2\cos(2\alpha_{LO}) + C^2\cos(2\alpha_P)\right) + AB\left(\cos(\alpha_S + \alpha_{LO}) + \cos(\alpha_S - \alpha_{LO})\right) \\ &\quad + AC\left(\cos(\alpha_S + \alpha_P) + \cos(\alpha_S - \alpha_P)\right) + BC\left(\cos(\alpha_{LO} + \alpha_P) + \cos(\alpha_{LO} - \alpha_P)\right) \end{aligned} \tag{3.6}$$

$$v_F = AB\cos(\alpha_S - \alpha_{LO}) + AC\cos(\alpha_S - \alpha_P) + BC\cos(\alpha_{LO} - \alpha_P) \tag{3.7}$$

So beside the error when $\omega_p \approx \omega_s$, we will get an error when $\omega_p \approx \omega_o$. We also get problems at image frequencies, we still have the bandpass filter, so we only get errors if $|\alpha_S - \alpha_{LO}| \approx |\alpha_S - \alpha_P|$ or $|\alpha_S - \alpha_{LO}| \approx |\alpha_{LO} - \alpha_P|$. So when $\omega_s - \omega_o \approx \omega_o - \omega_p$ and $\omega_s - \omega_o \approx \omega_p - \omega_s$. All these errors are heavily dependent on the phase of the pump, and can not be easily removed after the measurement. These last two can be removed with a bandpass filter before down conversion. This still leaves us with the case where the pump frequency is close to the one of the local oscillator, which is something we see in our raw measurements, as can be seen in figure 3.3.

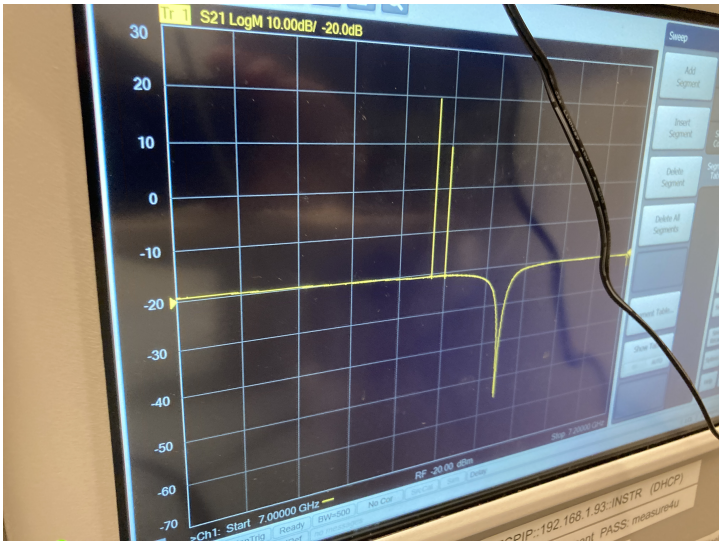

Figure 3.3: A magnitude plot of a S_{21} measurement. The VNA in this case picks up a second peak at a different frequency than the pump. The difference between them in frequency is constant, but differs between different VNA's.

The problem of the image contribution can be circumvented by using a four port VNA, so it can provide both the probe and the pump signal. This may also be a practical way to measure the idler magnitude and phase, as is recommended in 7.2.

3.2. Cryogenic SOL calibration

Instead of having a picture of the gain by subtracting the off from the on state, where a constant subtraction would not be visible, we want a calibrated picture. We can use the VNA to measure our loads, but since the JPA is based on Josephson Junctions, it needs to be cooled down, which means we are not able to manually interchange it with different loads. For this purpose we use a microwave switch, which can be seen in the lower right of the right image in figure 3.4.[29] The switch relies on impulses through coils to latch the different ports to the main node, which are the outer connector and middle connector respectively in the

image. The switch can change the connected ports by applying power to certain connectors, it can be used in different ways, as any number of ports can be connected to the center port. We will use it with only one port connecting, though this might go wrong if the switch does not properly reset, which would result in a combined reflection spectrum. For the SOL calibration to work properly, the different lines should have the same length, and have the same transmission. The current used to use the switch will heat up the sample plate, as the switch works by changing the connection mechanically by induction. So one should not apply the current for longer than necessary, as it will reduce the time our fridge is at base temperature. Since the coil

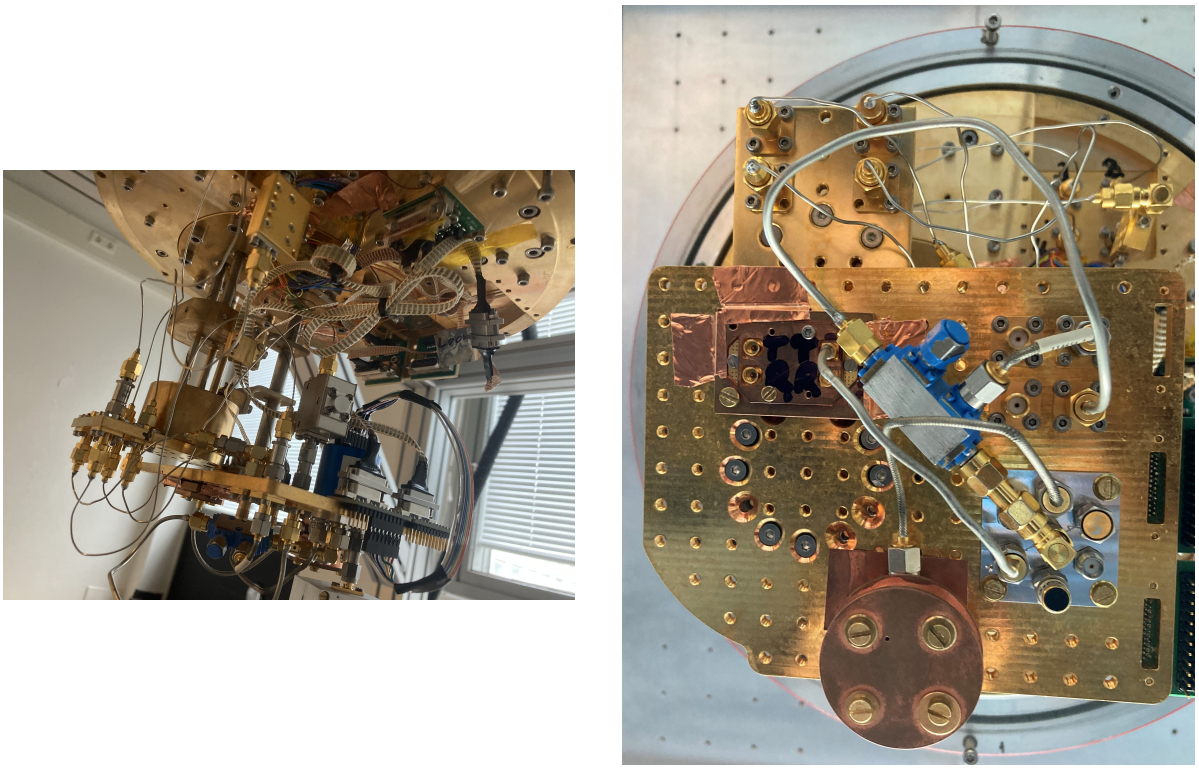

Figure 3.4: On the left one can see the main plate at the top, and the sample plate in the lower half, below which the connections to the switch are, more clearly pictured on the right. The isolator can be seen a the grey brick in the front, while the switch is the blue cylinder in the back. At the top center one can see the HEMT. On the right we can see the devices and the switch connecting to them. The JPA is on the left, while the Grenoble JPA is at the bottom, and the switch is in the right bottom corner. Above the switch are the connections to the input and output line, the short for the input, and the longer one for the output.

we use to induce magnetic flux is wrapped around the entire fridge, it may also impact the transmission of the wires in it, so we can do the calibration with the flux as an additional variable, though this did not seem to influence our measurements(not shown). Also in practice the JPA is not connected directly to the switch, so there will be a wire which we do not remove by calibration. Another thing to keep in mind are the amplifiers, they may contribute something depending on the input power. Near the saturation point, their transmission goes down. We use a different input than output line, which should result in S_{21} and S_{12} being very different. It would have been interesting to also measure both, but the HEMT does not transmit in both directions.

3.3. Noise measurement

To get a picture of the input noise of an amplifier, we need to turn it on, apply a signal, measure the gain, and the noise. The VNA is ideal for measuring the transmission, but now we want to measure the power of the noise originating from the DUT. For this we use a Spectrum Analyzer (SA). The SA is generally better at removing the images of the wanted frequency, as it expects signals at each frequency. The SA uses upconversion at first, with a local oscillator with a frequency above the measurement range. This way, it not only gets rid of the image, but also of the case where $\omega_p - \omega_s \approx \omega_o$, since this is impossible to achieve. When downconverting, this could again be a problem, but since we first use a bandpass filter, we can again use a frequency above our range. Afterwards, it is possible at this low frequency to apply a tight bandpass filter, with $\Delta\omega < |\omega_p - \omega_s|$ which removes the problem. Beyond this, the devices function the same, and although we mostly use the

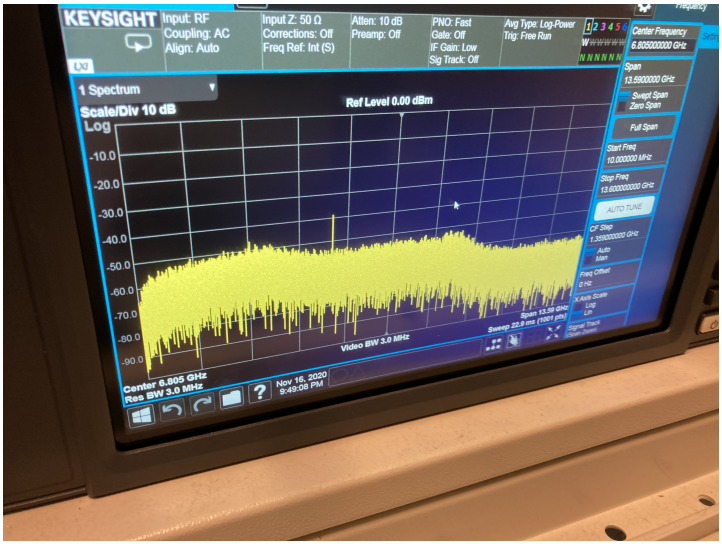

Figure 3.5: A wide range sweep for power as seen on the spectrum analyzer. The small peak seen denotes the probe, and can be seen moving if the VNA is sweeping.

SA to find the magnitude at the incoming frequencies, we can also use IQ demodulation to find the phase, which we can use for the carrier cancellation of our pump. The phase is randomized every time the SA starts measuring, so one can only compare phases at different times in a continuous measurement, and it only measures the phase at one frequency.

3.4. Carrier cancellation

We need to measure the noise of our amplification accurately on our SA, to find if it approximates the quantum limit, which has a problem with the usage of the JPA. Our JPA needs to be pumped for amplification, but this pump can also add a significant amount of noise on the SA. The pump does not only have power at the specified frequency, but will also have side bands, power near the pump frequency, caused by noise from generation. Additionally, the measured noise on the SA can be influenced by a large input power in or outside of the measured frequency range, as described in the specifications document of the Keysight MXA N9020B. So we need to minimize the amount of pump power going into the SA.

To achieve this, we can make use of carrier cancellation [35], with the carrier referring to the pump, although its name comes from radio technology. In that case they use a known radio frequency, and use a different source and shift it with half a phase shift to cancel out the incoming carrier. We could do the same thing, but this would not get rid of the side bands. We will use the same source for the carrier cancellation, we split it of from the output of the signal generator. Now we need to alter it before adding it to the signal going into the SA, to remove as much pump as possible. The system from input to output line will change the phase and power of the pump, which we need to copy with our carrier cancellation in addition to a π phase shift.

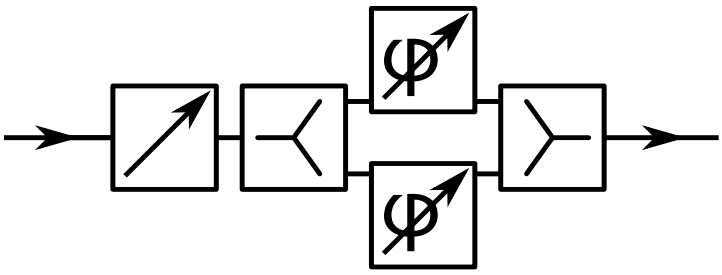

Figure 3.6: Simple depiction of the carrier cancellation circuit. A part of the carrier is put through the variable attenuator, then a splitter, then two phase shifters, then another splitter. The result is added to the received signal to cancel the carrier in it before measuring.

We will use the circuit depicted in figure 3.6, which can be very precise in phase and power. With only the attenuator and phase shifter, we would be able to control our phase shift and attenuation with one degree

and 0.1dB. By using two phase shifters however, we should have much more control. For the phase we'll be able to be change it in half a degree, while for the attenuation with about 0.01dB, in the ideal case.

There are a few things to take into mind with this method. First there is the fact that the phase shift and attenuation caused by the system is heavily dependent on frequency, which means we can only optimize the carrier cancellation for one frequency, so if the side bands are very wide and noisy, this would not be sufficient. Second, the MITEQ its amplification will decrease significantly beyond a certain amount of input power, as the amplifier saturates. So we will add the carrier cancellation signal before the MITEQ. Third, the JPA is not a linear element, the phase shift it adds to the pump is dependent on the power of said pump, which means the carrier cancellation needs to be adjusted accordingly. Finally, the phase shifters and the variable attenuator have errors that are larger than their own step size, let alone the one we can use for this circuit.

Since we do expect the correlation between the actual phase shift or attenuation and the set one to be always positive. With this in mind, we can try to find the ideal carrier cancellation settings organically. We measure the power and phase at the pump frequency at the SA, with which we can make an initial estimate of the right component values. Hereafter, we will measure the pump power at the SA, and then change one of the circuit settings. If it the power of the pump at the SA decreases, we change it to this setting and then repeat, with the code located in section 9.6. This can result in a local optimum however, as the precision in attenuation by the phase shifters is dependent on whether they constructively or destructively interfere. This may be prevented by finding the initial settings based on switching to the load in the fridge. If one would want more precision in phase with similar components, a third phase shifter in parallel would give that freedom.

3.5. Thermal noise calibration procedure

We have a similar problem with the noise measurements as we initially had with the transmission measurements. We only know the noise at the SA, and not at the port of the JPA. To be able to distinguish between the added noise by the JPA and the rest of the system, we need to know the noise at the reference plane of the JPA. If everything would be exactly linear this would not be much of a problem, but our amplification line will definitely add noise on its own: $N_{out} = A\left(N_{in} + N_{input}\right)$ Where A is the amplification and N denotes the noise power, two amplifiers together can be described as one amplifier this way.

Our SOL calibration will not help us here, as it cannot distinguish between the input and output line. The solution comes again in the form of calibration, this time using temperature, of which a simplified diagram can be seen in figure 3.7.

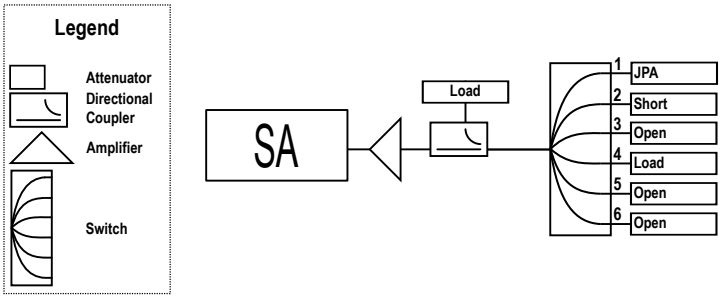

Figure 3.7: In this simplified version of our setup one can see the different noise sources, the SA will measure the load at the switch plus the input noise of the amplifier amplified. Or it will measure the noise from the load connected to the directional coupler, altered by the component selected by the switch, and then added to the input noise of the amplifier and then amplified.

We make use of the Nyquist noise created by resistance $N = k_B T \Delta f$ [26], though this no longer holds near the quantum limit, so we should make sure that $k_B T \gg hf$. By heating the noise source, be it attenuation or a load, we can find a linear dependence of the noise on the temperature. $N_{in} = c k_B T$ where c is related to transmission from the noise source to the amplifier chain. Depending on the location of our heated load, we will get different values for A and N, though one should realize that at zero temperature, we should always get the same value of noise at the SA, so AN is constant. This would mean the relation between the different reference planes is quite simple, but in reality, the relation of the noise between these points is complicated. This is due to the fact that cable resonances and impedance mismatches can reduce the amount of noise by multiplication, while attenuation will add noise by addition. Since we cannot find these transmission values by SOL calibration, this poses a limit to the accuracy of our results. One could use heated attenuation to circumvent part of the problem, since we then control its temperature to make sure it dominates the noise

going into the JPA. A closer look into a more precise and practical way for thermal calibration is in section 7.3

In our case we have no heated load, but we can heat up the HE3 stage in the fridge. An upside is that it should make sure the calibration also includes the wires in this stage, though the wires between this stage and the next may change the deferred linear dependence. However, with our fridge this is not a trivial matter, as the fridge does not cool continuously, but remains cool by gassing Helium3, which only gives us one static temperature. We are able to change the coupling between our helium3 and our sample plate though, so we've used that to control the temperature. This is temperature dependent however, so it could have an impact on our results, a detailed description is therefore given in section 9.3.1.

4

Setups

4.1. Setup for room temperature SOL calibration

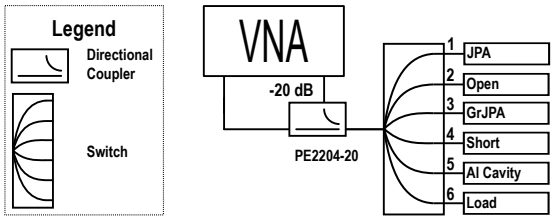

Figure 4.1: Diagram of setup for RT transmission measurements, with SOL calibration

Early on in this project, we were interested in getting the reflection spectrum of the device without all the cables in between. We found that SOL calibration promised just that, as described in section 2.6. Though we will use it in our cryogenic fridge, the He7 Entropy, as described in section 9.3.1, we first want to test this, and we do this at RT with this setup. Though we would be able to switch load by reassembly now, since we are aiming to use it in the fridge, we will use a microwave switch, the Radiall R591763600, as can be seen in figure 4.1.

The calibration plane will lie at the connecters on the switch. There are two things we should pay attention to with its use for calibration. The electrical lengths should be the same, as its absorption spectra. If not, this can result in a frequency dependent difference between the different spots, and would result in the short and open being non-ideal, as we expect an exact pi phase difference between them. If the electrical lengths are different but known, we could account for it within our calibration, as described in subsection 2.6.2.

We will use a aluminium cavity for testing, with a resonant frequency of the same order as the JPA. Within the cryogenic, we also need a separate in and output line, as the HEMT (the SN 506ZLNF-4_8C) transmits only in one way. With Jasper's project, a circulator was used to connect these two lines to the device, but we'll try a directional coupler as well, as it should result in less interference, which is what is seen in figure 4.1.

We will also test it with just one port, and remove the directional coupler. In one case we keep the switch, in the other we switch by reassembly.

4.2. Setup for calibrated reflection measurement

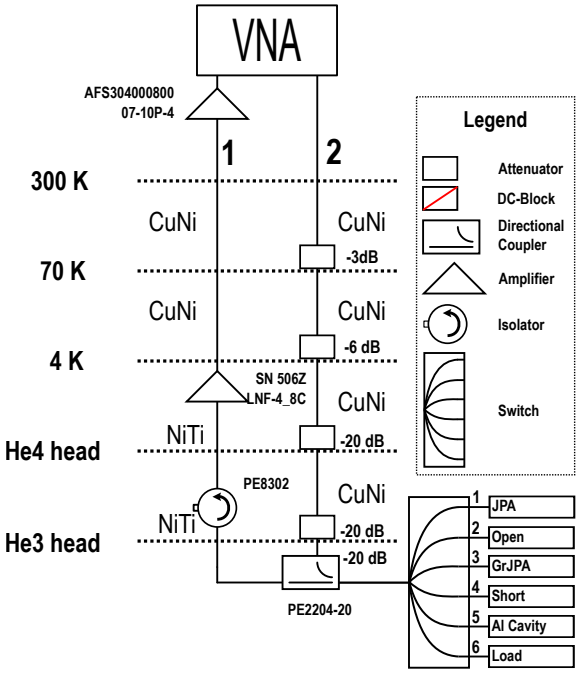

Figure 4.2: Diagram of setup for cryogenic transmission measurements, with SOL calibration and flux sweeping.

To be able to calibrate the JPA when it is superconducting, the calibration kit connected to the RF switch and be placed inside the fridge, as can be seen in figure 4.2. The JPA only becomes functional below $1K$, while the base temperature of the fridge is $300mK$. We assume that the lengths of the paths inside the switch are equal, and the short, open and load are chosen so that there reference plane lies at the connection to the switch. This means that for the open we can leave a port empty.

To test the calibration itself, the Al Cavity is connected directly to the switch, as the reflection spectrum of this cavity is relatively well known, as we used it in previous measurements and know at what frequency its resonance lies. Finally we also attach the JPA from Grenoble, as we know how it behaves, and its sensitivity to a magnetic field. There is a wire between the JPA and the switch, and the Grenoble and the switch, which will not be calibrated out. They are further attached to the sample plate, to be thermally connected.

On the outside around the fridge is a coil to create magnetic flux, which may not only affect the JPA, but also the other loads and wiring. We did not find this in any SOL calibration however(not shown). The flux is in the vertical direction, which should make it perpendicular to the SQUIDs, maximizing its desired impact.

Again a directional coupler is used to minimize the amount of interference from the input line, and to also keep the output of the switch amplitude as high as possible. This results in total of-69dB attenuation on the input line to the sample, so on the outside no more is needed. A HEMT (SN 506Z LNF-4_8C) is used to amplify the signal by about 30dB, and a miteq (AFS304000800 07-10p-4) for 30dB on top of that. We tried to get a less noisy vna measurement by adding another miteq of the same type, but the power was too high for a reliable usage. The HEMT should add very little noise to the signal $< 3K$, however, in our measurements we found that changing between different power supplies could result in a high amount of noise at specific frequencies $\ll 3K$. (not shown)

With this setup we can measure the reflection spectrum of the JPA, which is calibrated to the plane of the switch, and its dependence on the magnetic field and the power of the incoming signal, by sweeping these parameters.

4.3. Setup for calibrated pumped reflection measurement

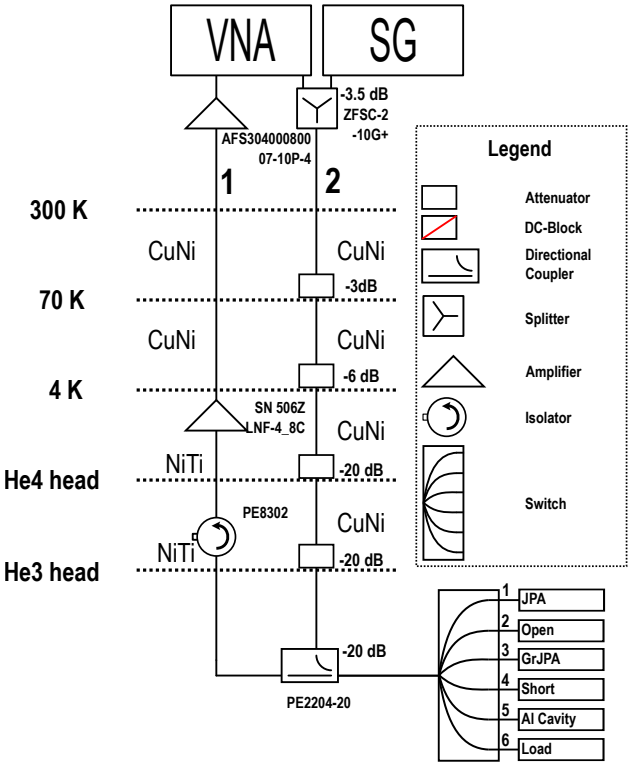

Figure 4.3: Diagram of setup for cryogenic transmission measurements, with SOL calibration, flux sweeping and pumping.

To do pump measurements, we include a Signal generator, the Keysight_N5183B, to provide the pump, as can be seen in figure 4.3. We connect this with a splitter to the VNA input, which results in both of them have less max power. One problem that may arise here is the fact that the pump can be seen in the spectrum found by the VNA. Even worse, due to the way the VNA mixes signals, it can actually see the pump at multiple frequencies, as described in subsection 3.1.1. This will have to be filtered out afterwards, and since the width peak of the pump is smaller than the space between datapoints, it will not make the data unusable, as it will only affect either one or two datapoints. We took these measurements at two different cooldowns, where we in between tried to reduce the reflection back into the JPA, this did not help with that, as can be seen in figure 9.16 and 9.17. With some measurements there was a strange shape in the reflection spectrum, which only appeared for some measurements.(not shown)

4.4. Setup for noise measurement

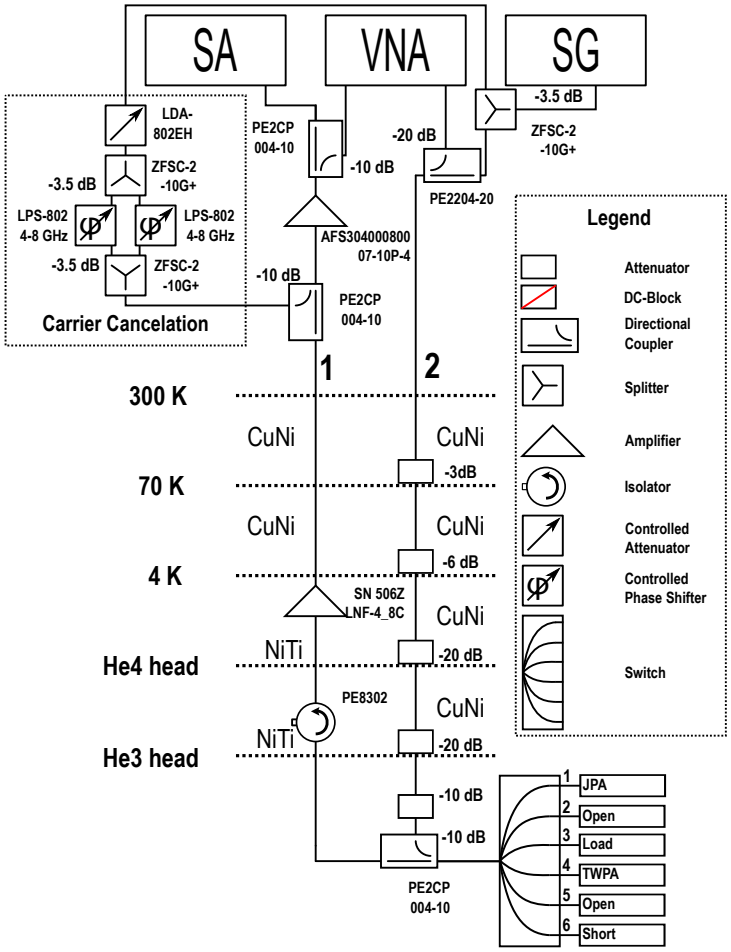

Figure 4.4: Diagram of setup for cryogenic noise measurements, with carrier cancellation and used with thermal calibration. Can also still be used for SOL calibration, flux sweeping and pumping.

For our final experiment we want to measure the noise contribution of the JPA when it amplifies. To measure the noise, we will use a spectrum analyzer (the Keysight_MXA_N9020B). A high power signal can however distort the measurement of a SA, even outside the field of the measurement.[20] The pump also provides extra noise that will be picked up by the SA, and since the JPA amplifies in a small range near the pump when optimally pumped, this can alter our results.

To circumvent this, we will use carrier cancellation to prevent the pump and its noise to reach the SA and VNA, as can be seen in figure 4.4, and described in section 3.4.

One problem that may arise is that there is a leak backwards trough the carrier cancellation circuit, which will alter the results and will also change the measurement of the SOL. Since the pump at the SA is heavily dependent on the state of the JPA itself, the carrier cancellation is specific for only one setting of pump frequency and power, which will limit the use of the calibration in this setting. This entire problem could be negligible, but this turns out to not be the case, as described in subsection 6.5.3.

With this setup we will also use thermal calibration, as described in section 3.5. Since we do not have a heated load, we will heat up the entire sample plate, which is everything below the lowest dotted line in figure 4.4, a procedure further described in section 9.3.1. For this it is important to realize that the HEMT is not on the sample plate, but at the main plate, and will thus be at that temperature.

5

Results I: Calibrated reflection measurements

5.1. Simulations of SOL calibration with ideal and non ideal components

To test our calibration method we will simulate our system. We used a simulation program for circuits, Quite Universal Circuit Simulator(QUCS),[6] to simulate an imperfect connection to a cavity. We start from the ideal setup and work towards the setup we actually have. The setup will include a system to do the SOL calibration, so with these simulations we can test whether it works simulated, one of these setups is the one in figure 4.1.

5.1.1. One Port Calibration

One port calibration is the simplest, we have two cases, one for when there is no difference in the optical wavelengths of the loads, and one where there is. We will account for that, as described in the theory section 5.1.2.

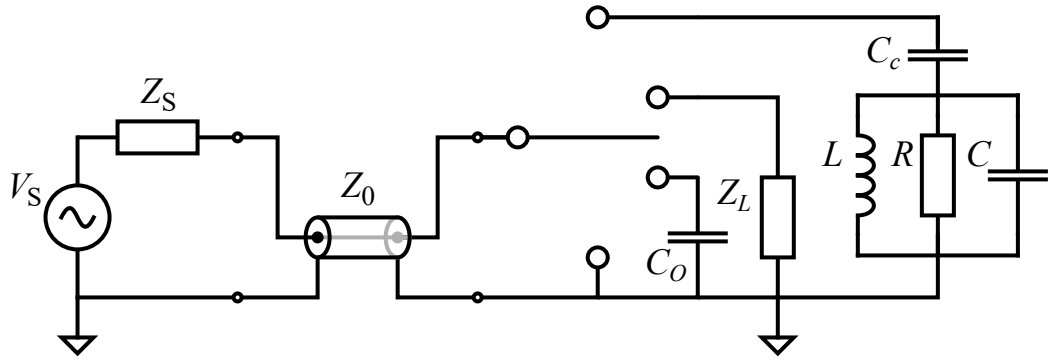

Figure 5.1: The circuit for simulating the ideal case for SOL calibration, for our purposes there is an impedance mismatch between the source and the transmission line on the left, but not between the load and the transmission line, so $Z_L = Z_S$. The switch can connect to a short, open, load and a resonator, in that order from bottom to top.

Our simulation circuit looks like in figure 5.1, we use a lossy transmission line with a different impedance to get a frequency dependent background. The simulation with QUCS uses a separate ground for everything, but this should not matter, and this is a closer depiction to the experiment. On the right is the our resonator, a capacitively coupled parallel RLC circuit. To use the different loads, we are using the switch to connect to a single load, in the simulation, this will be done by changing the resistance of that line to zero, while the others are set to infinity. We find the results in figure 5.2 (blue, green and purple lines), which are the measured reflection for the open, short and load respectively.

The raw phase, as seen in figure 5.2.b has a lot of discontinuities, so we unwrap it, to subplot b. Afterwards, there is a linear dependence of the phase on the frequency, which is caused by the increased accumulation of phase with frequency over electrical length. We remove the linear dependence to a reference level, in this case at the plane of the connections from the switch, which results in the graphs in figure 5.2.d.

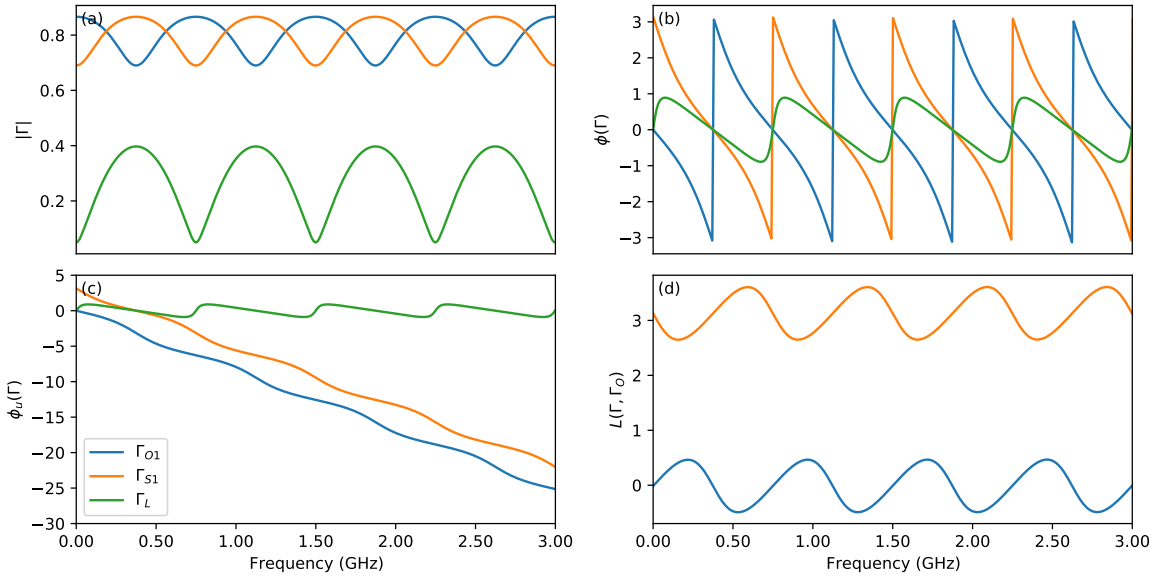

Figure 5.2: Simulated response of the Short, Open and Load for the circuits in figure 5.1, using orange, blue and green. Magnitude in subplot a, phase in subplot b, unwrapped phase in c, and unwrapped phase with the removal of a linear phase in d. The

Using this data and equation 2.134, we get the results shown in 5.3(green), which is indistinguishable from the actual response function of the pure resonator(orange).

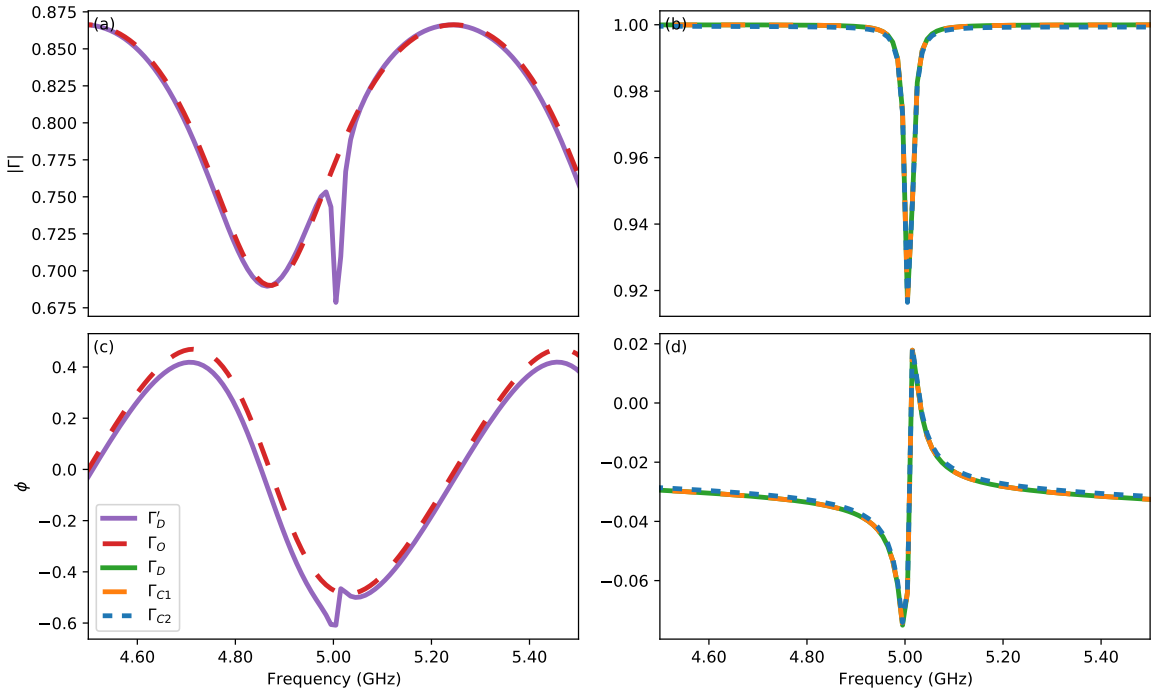

Figure 5.3: Comparison between the uncalibrated cavity response on the left, and calibrated and pure cavity response on the right, using the simulation circuit in figure 5.1 and 5.4. Visible is the deviation between the two calibrated magnitude plots, this is due to the phase difference between the Open and Short decreasing. We can see this even better at higher frequencies, in the appendix in figure 9.12

As one can see, the peak of the cavity is much smaller than the background. Yet when we calibrate, the cavity becomes clear. One can also notice that the magnitude of the measured reflection of the Open exactly follows the cavity save from frequencies near resonance. This may be used to find the difference in wire length between the two, and the loss, if applicable. This is due to the fact that our resonator can be approximated as an open far from resonance.

5.1.2. Differing path lengths

As not all our calibration kits are build to have equal electrical distances, and small differences may be significant, as we can later see with the experiments, we model them into our simulation, as seen in figure 5.4, with an additional transmission line for the Open and the Short. The ground is still the same for every part, which differs for the simulation, where they are all separate, and the experiment, where they are connected by the transmission line to the ground of the source.

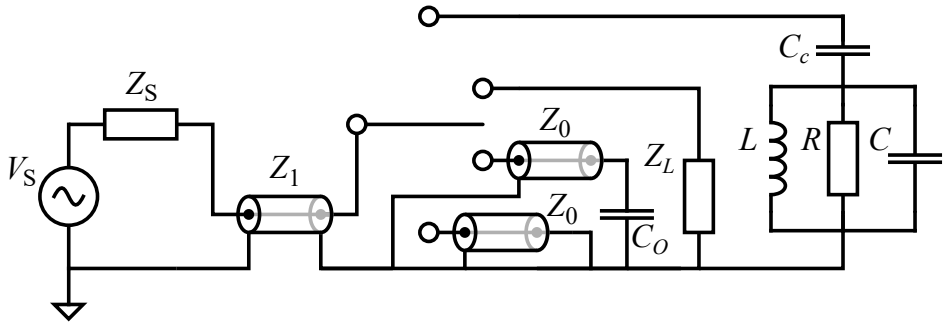

Figure 5.4: The circuit for the second simulation, with as difference from figure 5.1, the transmission lines in front of the open and short. These are not lossy and have matching impedance to the source, so $Z_S = Z_L = Z_0$.

The effects of this difference can be seen in figure 5.5.

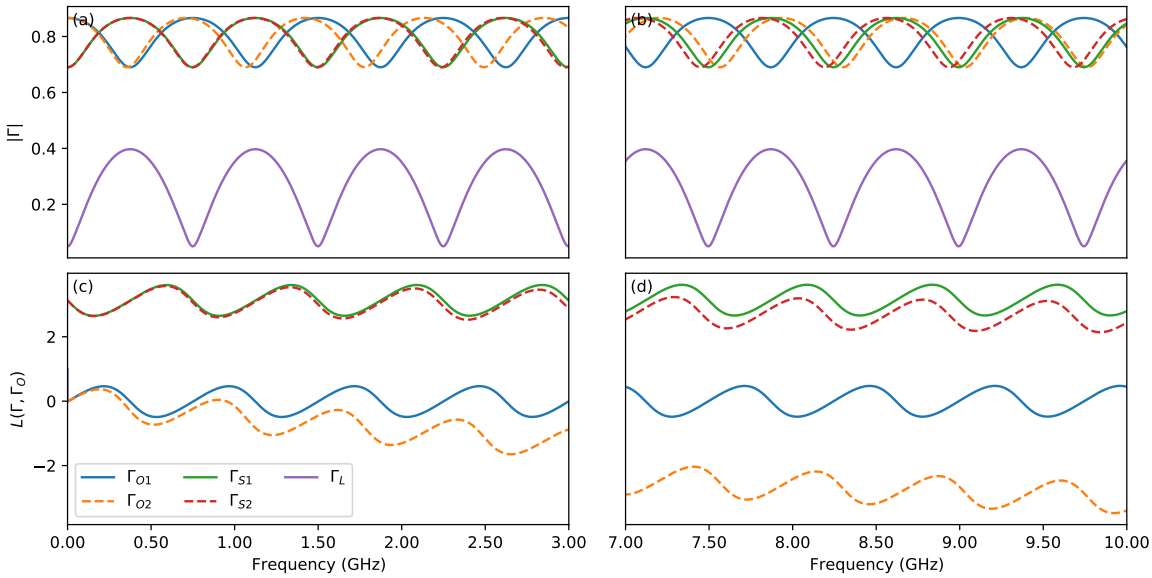

Figure 5.5: Simulated response of the Short, Open and Load for the circuits in figure 5.1, using green, blue and purple, and 5.4, using red, orange and purple. Magnitude in the top row, phase in the bottom row, with the left and right having two different frequency ranges. The phase difference increases for larger frequency, and at some point the Short and Open will have the same phase response, as seen in subplot d. The magnitude also shifts, which shows that we can't simply multiply our measurement with a phase.

We can see that its pattern has a smaller period than with the previous simulation, and that this is also different between the Short and Open. Though at first the difference is small, as we can see at 10 GHz, the difference between the short and open in phase is nearly 2π, while it should be 1π. The difference will be approximately 2π at $\approx$ 14GHz, and here is where our calibration breaks down. We need different loads to completely define our system. At much lower frequency the effects of this can already be seen, as one can see in figure 5.3.b, where we can see that for increasing frequency the found solution deviates increasingly from the pure response function. We are still way below the frequency at which are calibration breaks down completely though, so we look at the found S-parameters to see what is going wrong, in figure 5.6.

Though the differences are small, they are significant, and increase with higher frequency. As we get near the point where $\Gamma_O(l_O) = \Gamma_S(l_S)$ and in conjunction $\Gamma'_O = \Gamma'_S$ in equation 2.134. Let's look into this limit by taking $\Gamma_O(l_O) = \Delta\Gamma_S(l_S)$ and $\Gamma'_O = \Delta'\Gamma'_S$. The Delta's are a dimensionless parameter for taking the limit, if there

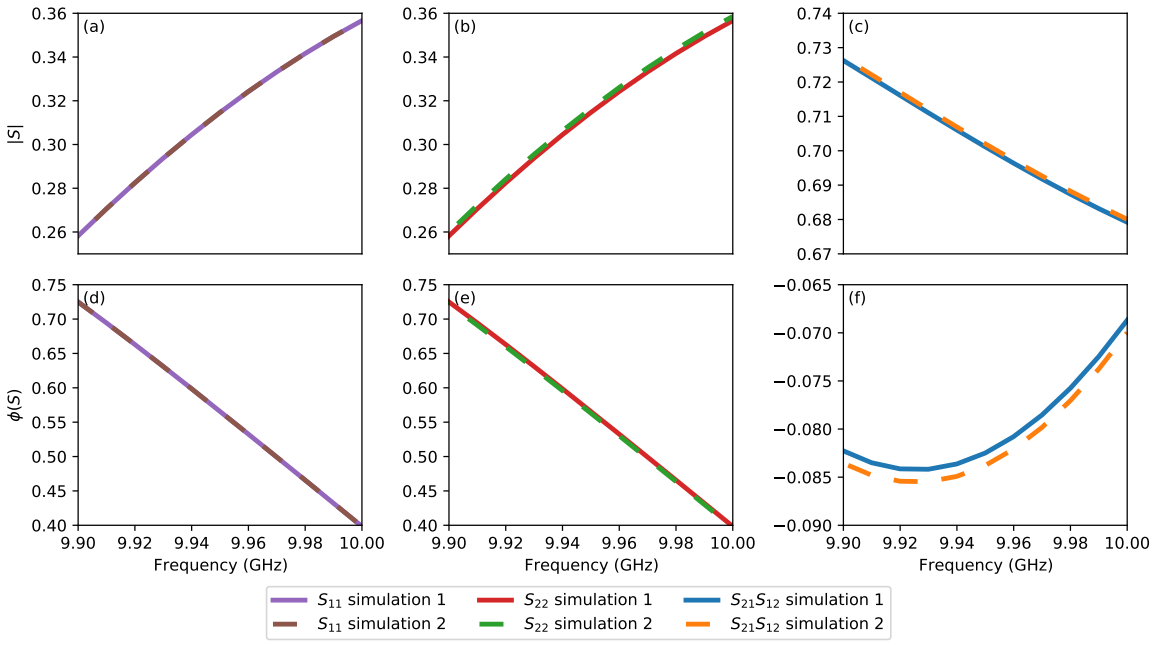

Figure 5.6: These are zoomed in, so one can see the deviation in the found system parameters. Another thing to notice is that S_{22} and S_{11} are exactly alike, which makes sense, since the transmission line should reflect in both directions equally. A wide frequency plot can be found in the appendix in figure 9.13.

is an analytical solution, the limits should give the same answer. Now taking different limits will show it's poorly defined:

$$\lim_{\Delta \to 1} \Gamma_D = \Gamma_S \tag{5.1}$$

$$\lim_{\Delta' \to 1} \Gamma_D = 0 \tag{5.2}$$

We may be able to find the error with the derivative in frequency of the measured loads, but this will probably not be practical in experiments. As it turns out, a change in electrical length of only a few micrometers will remove the deviation we see, as can be seen in figure 9.14. In our experiments, we will not know the difference between our electrical length with this certainty though. This is only relevant when the difference in the response of the Short and Open at the reference plane is significantly less than π. To get the same deviation when the difference is π, we would need an error in mm for the difference in electrical lengths, as can also be seen in figure 9.14.

There are other things to see with the scattering parameters in figure 5.6. S_{22} and S_{11} are exactly alike, which makes sense, since the transmission line should reflect in both directions equally. They are also inversely related to $S_{21}S_{12}$, which makes sense, since reflection will reduce transmission. They do not add to 1 though, as there is attenuation in the line.

5.1.3. Ideal Circulator

In the previous examples we only had to worry about the reflection of the wires, since we only did a S_{11} measurement. Our actual setup has a one way amplifier, and thus uses different input and output line connected to our cavity with a connector, which interference we will address now. We will use the simulated circuit in figure 5.7.

We can change the S parameters of the component that we use for connecting the three transmission lines. We start with an ideal circulator, where the entire signal at a port is transmitted perfectly to the next port in a clockwise pattern. If we name these three ports A to C, where S_{ba} means the transmission from a to b, we get:

$$S_c = \begin{bmatrix} S_{aa} & S_{ab} & S_{ac} \\ S_{ba} & S_{bb} & S_{bc} \\ S_{ca} & S_{cb} & S_{cc} \end{bmatrix} = \begin{bmatrix} 0 & 0 & 1 \\ 1 & 0 & 0 \\ 0 & 1 & 0 \end{bmatrix} \tag{5.3}$$

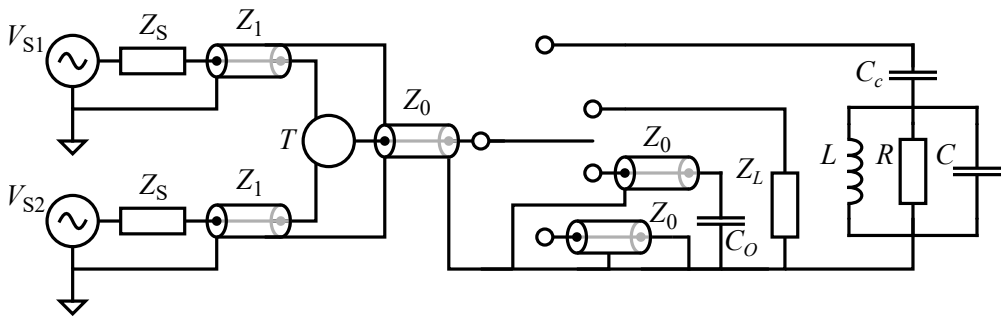

Figure 5.7: The third simulation circuit, with a three port component with variable transmission parameters, between the left three transmission lines, with differing impedances. By changing the transmission parameters of this component, we can model an ideal or non ideal circulator, or even a directional coupler.

But even now, there will be some interference due to the reflection in the wires. This can then be passed back to the other channel of the circulator than the supposed one, though there should not be any bypass. We use different impedances and lengths for the different transmission lines, all in all resulting in figure 5.8.

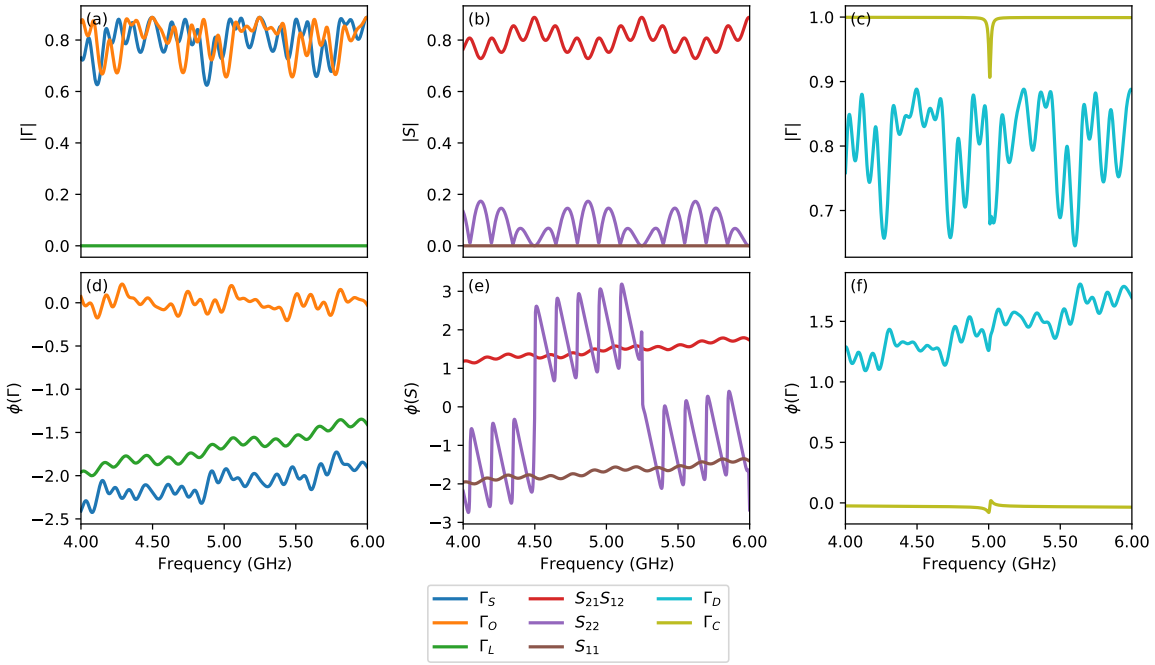

Figure 5.8: The results of the SOL calibration of the ideal circulator, with on the top row, the magnitude and the bottom row the phase. From left column to right, the measured loads, the S-parameters, and a comparison between the calibrated and measured device. There is no bypass, and the cavity cannot be discerned from the raw plot.

It is no longer possible to find the resonator in the raw plot, and the measured loads also seem a chaotic mess. We can see in the S_{11} magnitude in figure 5.8.b, that there is indeed no bypass, as one would expect from an ideal circulator, which can also be deferred from the reflection of the load in 5.8.a, though the simulation still finds a phase. There is also little internal reflection, but still enough to make the cavity discernable from the raw plot. With the calibration, the peak again comes forward, this time without visible tapering, though this is probably due to our frequency range. The measured cavity also does not align well with the measured open any longer.

5.1.4. Non ideal Circulator

We now change the parameters of the circulator and add a transmission from a port of it to the port in the counter clockwise direction, and itself. We do however keep the squared S-parameters adding to 1, so no

power is lost in the circulator, so:

$$S_c = \begin{bmatrix} S_{aa} & S_{ab} & S_{ac} \\ S_{ba} & S_{bb} & S_{bc} \\ S_{ca} & S_{cb} & S_{cc} \end{bmatrix} = \begin{bmatrix} x & x & \sqrt{1-2|x|^2} \\ \sqrt{1-2|x|^2} & x & x \\ x & \sqrt{1-2|x|^2} & x \end{bmatrix} \tag{5.4}$$

With $x = 0.3$, so in this case the interference should be much worse, as now not only does a part reflect back, another part is transmitted to the wrong channel, though our simulated circulator still has no loss. The results can be seen in figure 5.9.

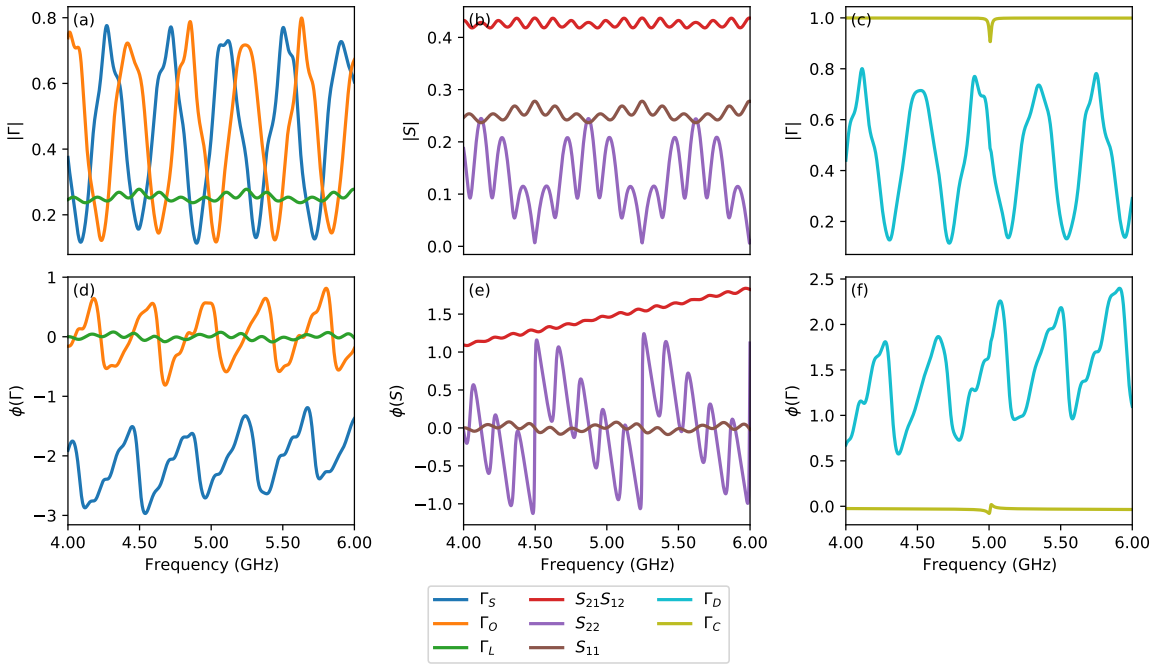

Figure 5.9: The results of the SOL calibration of the non-ideal circulator, with on the top row, the magnitude and the bottom row the phase. From left column to right, the measured loads, the S-parameters, and a comparison between the calibrated and measured device. With a non-ideal circulator, we now do have bypass, as can be seen in subplot a and b, as the load and S_{11} are non-zero.

In the figure, there is now a lot of internal reflection, as S_{22} is much higher than before. There is now bypass as well, as not all of the signal has to go trough the switch, as one can see in S_{11}. The peak is now of the order of the background dependence, but the result remains the same as in the previous simulation.

5.2. Room temperature experiments of SOL calibration.

Since we do a SOL calibration, we need an ideal Short, Open and Load. We have only access to regular Short, Open and Loads though in our real world experiment. The deviation of the Short and Open from the ideal case is not significant of influence. The Loads is however, as any signal it does reflect will result in the calibration overestimating the amount of reflection, and the loads will reflect a bit, depending on frequency. We have multiple kits, each consisting of a short, open and load. The first one is the keysight 3.5mm hanger[19], with equal pathlengths, but since they cannot be separated, they cannot be connected to the switch all at once without wires. Another one is a SMA kit[17] which does consist of separate objects but will still need connectors to the switch, as this kit as well as the previously mentioned consists of female connectors, just as the switch. This kit also has differing pathlengths between the components, which need to be taken into account to get sensible results. Finally, we have a short and two loads nobs, which make two kits if we add an open site as the open, these would be more practical to use, especially in the fridge, as these have male connectors. The differing path lengths can be modeled as lossless transmission lines, but that seemed only valid for small path differences. This is no longer the case when the path length differ in the order of dms, which happens if we want to calibrate out the wire to the device.

5.2.1. Reflection at VNA

First we attach the loads directly to the VNA, either by a small connector if the kit has female connectors, or without one if male. Now we only have to worry about the path differences between the Short and Open, and neglect the path to the device.

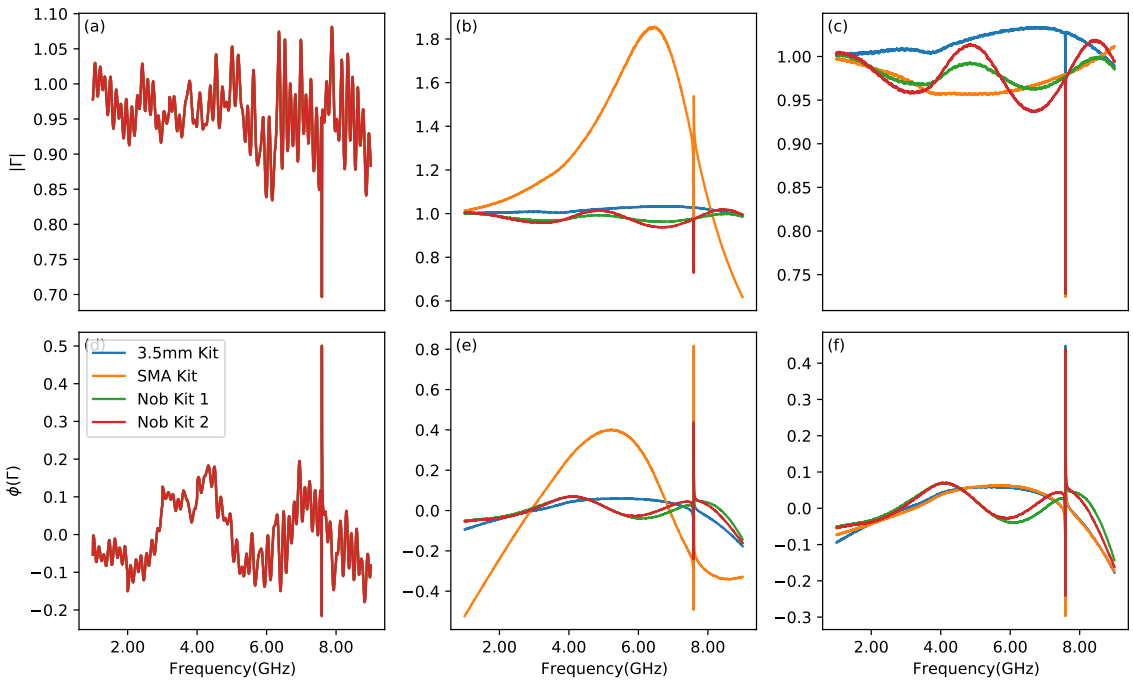

Figure 5.10: SOL measurements directly at the VNA, where we can see the difference between the different kits. Top row is the magnitude, while bottom is the phase. From left column to right, raw measurement, calibration result without adjusting for pathlenghts, and with adjusting for pathlengths. Note that the phases are without their linear component, so they are not to be compared that way.

As one can see in figure 5.10, with the subplot b and c, we immediately run into problems for the SMA kit. This is due to the differing pathlengths for the short and open, changing the difference in the reflected phase at the reference plane. The pathlengths are given by the manufacterer, but we can also try to discern them ourselves. We can look at the linear dependence of the phase on frequency, as given in table 5.1, since the accumulated phase will increase with distance and frequency. This is not entirely accurate however, as some of the signal will be reflected in the wire, thus decreasing the average electrical length. If the device is well known, one can discern the lengths from the total picture. Adjusting for the differing paths makes the calibration fare much better for the SMA kit, as can be seen in subplot c and f in figure 5.10.

Table 5.1: Electrical lengths in cm when connecting the kits and device directly to the VNA. Values are found by looking at the phase accumulation with increasing frequency, and will underestimate due to reflection in the wire.

	Short	Open	Load	Device	Calibrated
3.5mm Kit	5.2	5.2	0.1	6.0	0.8
SMA Kit	5.1	5.6	2.6	6.0	1.1
Nob Kit 1	2.0	2.0	1.6	6.0	4.0
Nob Kit 2	2.0	2.0	1.9	6.0	4.0

5.2.2. Reflection with Switch

The main advantage is that we do not have to remove and attach a different component, a downside is however that the Al-cavity and the other components cannot all be connected directly at the same time, as it does not fit, at least not for each kit. This will also more closely resemble our cryogenic setup though, as our device cannot be connected directly to switch at all, as seen in figure 3.4 on the right, resulting in the setup used for figure 5.11. Most important for testing the switch is whether the pathlengths to the different ports are equal, just as there transmission values. We can calculate the electrical distance difference by looking at the phase change by frequency, resulting in table 5.2. We have to be careful though, as the phase may not be that reliable, as any reflection in the wire will decrease the measured pathlength. Afterwards one can find a value for the loss over the transmission line distance, as long as we know the general behaviour of our device, which is what is finally used. This may no longer be relevant for the fridge calibration however, as we may not have a loss over this wire anymore, as they should be superconducting.

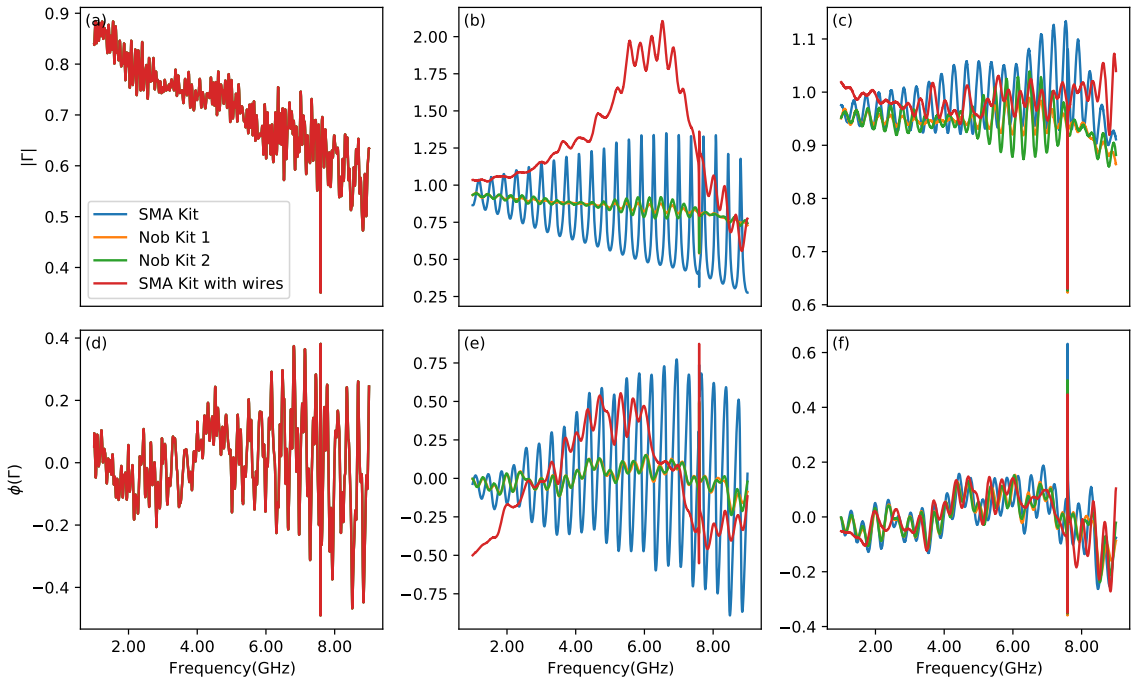

Figure 5.11: Calibration using the microwave switch, where the device is connected to the switch using a wire with an electrical length of about 40cm. On the left is the raw data, while in the middle calibration directly, and on the right with taking different path lengths effects on phase and magnitude into account. The red plot is made with the components connected to the switch with wires of equal length as the device. Note that the phases are without their linear component, so they are not to be compared that way.

This outcome seen in subplot b and e in figure 5.11 seems strange, as the calibration outcome is much worse than expected for the nob kits, as they do not have problems with differing electrical pathlengths. We expect the SMA kit to have trouble due to differing electrical lengths, but the nob kits (green and orange) do much worse than in figure 5.10 due to the wire connecting the device. It is important to realize we calibrate to the plane of the switch, so we have the device with its wire reflection spectrum as our calibrated reflection spectrum. The SMA kit(blue) actually does better than before, if the differing pathlengths are not taken into

Table 5.2: Electrical lengths in cm when connecting the kits and device via switch to the VNA. Values are found by looking at the phase accumulation with increasing frequency, and will underestimate due to reflection in the wire.

	Short	Open	Load	Device	Calibrated
SMA Kit	96.7	97.2	71.5	138.3	41.3
Nob Kit 1	93.7	93.6	60.4	138.3	44.6
Nob Kit 2	93.7	93.6	59.7	138.3	44.6
SMA Kit with Wires	137.3	137.8	76.0	138.3	1.1

account, as seen in figure 5.10.b. This is due to the same wire connecting to the device, as the pathlength difference is smaller on the new scale. The red curve actual fares very similar to the SMA kit in the previous figure. This is due to its components also being connected by wires, as can be seen in table 5.2, they are near the length of the wire connecting to the device. So now the differences are between the short and open are larger relative to the device. Small errors can have drastic consequences at high frequency, as they get nearer to half a wavelenght, as is describe in section 5.1.2.

With taking the pathlengths into account the red curve actually fares best. For this kit we do not have to know anything about the loss of the wires, which we used for the results to get rid of the slope in their magnitude, and get the result close to 1, as seen in figure 5.11 from subplot b and c. The magnitude gets above 1 sometimes though, due to the fact that differences between the wires result in a more chaotic reflection spectrum. One can also decrease the wobbles of the nob kits by making assumptions about the wire to the device, and the tiny pathlength difference between the Short and Open.

5.2.3. Circulator and Directional Coupler

Here we use the SMA kit for this experiment, testing only for the differences between the use of different connectors, though we will use a nob kit for later experiments out of practicality, these are less well known. We now always include the different pathlengths in our calibration. We expect the directional coupler to fare better than the circulator, as we expect the bypass S_{22} to be 20dB less due to the design of the directional coupler, and the backreflection S_{11} to be less as well. The experiment to test this, resulted in figure 5.12 and table 5.3.

Table 5.3: Electrical lengths in cm when connecting the device via switch and the coupler, while using the SMA kit. Values are found by looking at the phase accumulation with increasing frequency, and will underestimate due to reflection in the wire.

	Short	Open	Load	Device	Calibrated
SMA Kit Directional Coupler	189.0	189.5	144.8	190.0	1.1
SMA Kit Circulator	190.7	193.6	148.6	193.9	1.1

The result is actually fairly similar, though at $f < 4GHz$ the circulator fares much worse. The difference in subplot c is caused by differing found electrical pathlenght, and is actually not large for frequencies above 4GHZ. One difference that is significant, is that the dip in the calibrated magnitude is much deeper for the directional coupler. This convinced us to choose for the directional coupler in our setup, as we expected more of the detail of the cavity to remain through calibration. However, if one compares them with the previous graph, as in figure 5.10.c or 5.11.c, it would seem that the value found by the circulator is more accurate. This turns out to be due to a too large stepsize in our frequency, and means that this difference is not due to differences in components, but our VNA settings. Secondly, since the frequencies below 4 GHz are not relevant in our case, the choice for the directional coupler is somewhat arbitrary. Not realizing at the time, we stuck with the directional coupler, since it should theoretically fare better, and we do not know how much the case at room temperature deviates from the one at base temperature. It also was the most often used connector with our setups. However a closer look shows that this reasoning is a bit misguided in hindsight, as we discuss the S-parameters in the next section.

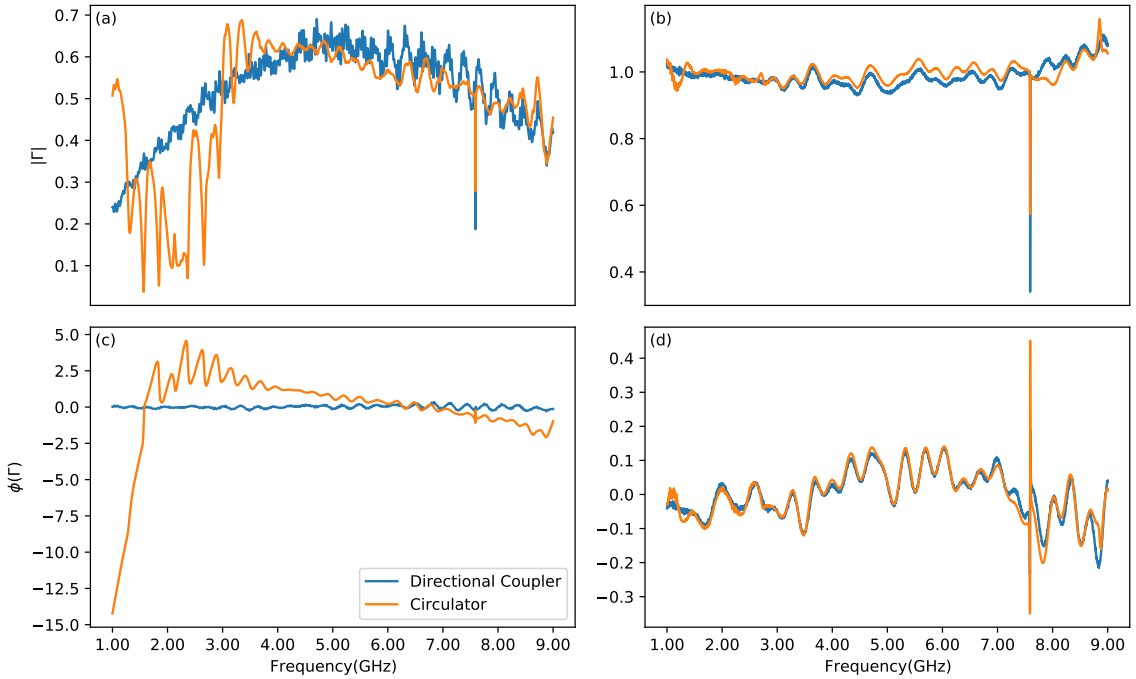

Figure 5.12: Calibration using the microwave switch, with either the circulator or directional coupler to transform the S_{11} measurement in a S_{21} measurement. Left column are the raw device measurement, while on the right the calibrated, at the top row the magnitude, bottom phase, the phases are without their linear component, so they are not to be compared that way. Note that Γ_D is multiplied by 10 for the directional coupler case, to account for the attenuation. A close up of the cavity can be found in the appendix, figure 9.15.

5.2.4. S-Parameters

We now take a look at the S-parameters of the circuit with a directional coupler or an circulator, which will give us more insight in the details of transmission, as can be seen in figure 5.13. We will discuss this with the knowledge gained in hindsight here, as may be relevant for readers of this document, though this was not used for the design of our circuit.

Now a quick glance at the values for the parameters would make the directional coupler fare much better. However, when multiplying S_{11} and $S_{21}S_{12}$ of the DC with 20dB for better comparison, we find that these are actually comparable! Only at the outer frequencies does the DC fare much better, and this is not relevant for our device. The bypass should be much lower for the DC with a coupling of -20dB, as it should be twice the coupling, -40dB.

One of the main reasons for doing the comparison between directional coupler and circulator was the observation from Franse [13] subsection 3.1.3, that reflection from the circulator causes backreflection. Which was found later to be the upper limit for the amount of calibrated gain we can show, as can be seen in section 6.4.1. Here the directional coupler does not give a significant advantage, and might even be slightly worse.

In hindsight there is even another factor, because we found that at certain frequencies the pump power is a limiting factor. The directional coupler increases the attenuation on the input line, which is disadvantageous in this regard, further limiting our power.

The last problem would not be hard to deal with though, as one could simply remove some attenuation on the input line. The backreflection could also probably be decreased by adding attenuation in front of the switch, and if that is not an option, one could try to find the culprit of the reflection and change the component or the wire. This does show the great advantage of doing this analysis and measuring the S-parameters of a system, as the bypass, backreflection and transmission are clearly very relevant for measuring a device quantitatively.

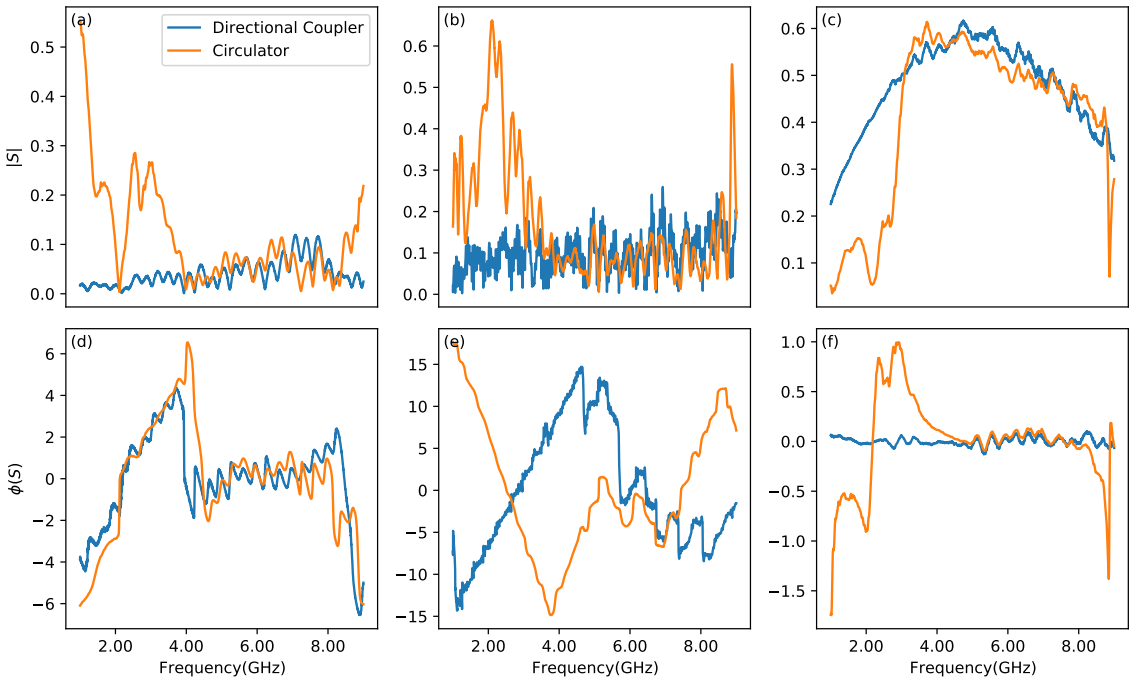

Figure 5.13: S parameters found with the previous calibration, with from left to right S_{11}, S_{22} and $S_{21}S_{12}$, with at the top row magnitude and bottom row phase. For S_{11} and $S_{21}S_{12}$ the magnitude of the directional coupler is case is multiplied by 10, for ease of comparison. From these plots, one could say that a directional coupler does not provide a significant advantage at the relevant frequencies, as S_{11} and S_{22} are similar. However, S_{22} is with a magnitude of 0.1, or -20dB sufficiently small to show high gain. Note that the transmission values are the square root of power, and so a factor 10 is 20 dB.

6

Results part II: Calibrated measurements of a nanobridge JPA

The main goal of the experiments is to quantify characteristics of the device, the JPA, such as amplification, resonant frequency and magnetic susceptibility. By using our SOL calibration we can get an absolute number for amplification, and with thermal calibration, for input noise. As described in Eichler and Wallraff [11], or in equation 2.103:

$$\delta \equiv \frac{\omega_\delta}{\kappa+\gamma}, \qquad \tilde{\alpha}_{in} \equiv \frac{\sqrt{\kappa}\alpha_{in}}{\kappa+\gamma}, \qquad \xi \equiv \frac{|\tilde{\alpha}_{in}|^2 K}{\kappa+\gamma}, \qquad n \equiv \frac{|\alpha|^2}{|\tilde{\alpha}_{in}|^2} \tag{6.1}$$

$$1 = \left(\delta^2 + \frac{1}{4}\right) n - 2\delta\xi n^2 + \xi^2 n^3 \tag{6.2}$$

The system actually mainly depends on these four dimensionless parameters, though they can not be directly measured. A variable that defines the state of the JPA is the photon number, but that can not be measured directly either. We are also not able to distinguish between the ingoing power and the non-linearity, we can only make an estimation since we do not know the transmission value of the ingoing and outgoing line separately. However, with our calibrations, we can find a close estimate of the absolute amplification and the input noise of the JPA, and thus a good idea of its practicality.

6.1. Overview of chip

Though our chip has multiple ports, we focus on one device on one port, denoted as 6.3GHz in this report, Franse [13] in mostly section 3.4, while additional info on the SQUID reference cavity can be found in section 3.3. This device has two resonators, both made from aluminium, meaning it becomes superconducting below approximately 1K.[9]

One of which is a side coupled capacitively coupled RLC resonator, with as inductor a single nanobridge SQUID in addition to a linear one, as seen in figure 6.1, the SQREF cavity. This one is nearly critically coupled, so at resonance nearly all power should be dissipated. The device consists of two capacitors connecting the center to ground in parallel, while a linear inductor and then a single SQUID also connect this point to ground, in sequence. This point is then connected to the transmission line with another capacitor, which is made by a bar of aluminium running parallel to the tranmission line, and with a gap in between. Each of the other capacitors are made with two sets of fingers, to increase the surface between them.

Secondly there is a capacitively coupled RLC resonator, with as inductor a nanobridge SQUID array, as seen in figure 6.2, the SQARR cavity. This one should be overcoupled, with approximately no dissipation at superconducting temperatures. This device has less parts, it has a fingered capacitor connecting a central point to the transmission line. This point is also connected by a similar designed capacitor and the SQUID array in parallel to ground. The properties are summarized in table 6.1

These are only estimates, and the actual values will be different, though should be on the same order of magnitude. The inductances can be estimated based on the geometry of the SQUIDS, where the total area increases the linear inductance, the total area of the SQUIDS increases the loop inductance, and the critical current of the nanobrdige junctions control the Josephson Inductance.

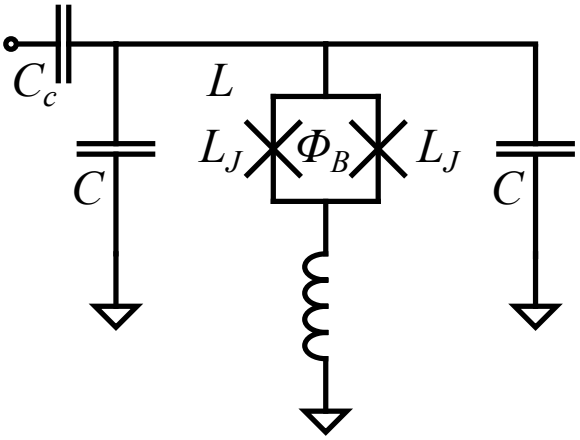

Figure 6.1: Schematic of the side couple reference cavity measured. Note that here we can find the only capacitor not made by intertwining fingers, as the C_c is a bar side to side with the transmission line.

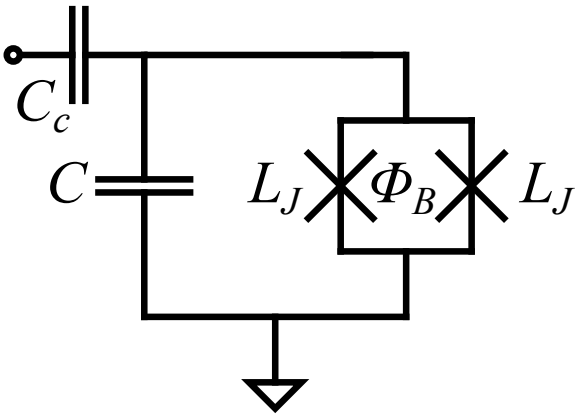

Figure 6.2: Schematic of the SQUID array cavity, though the single SQUID seen here represents the entire array of 20 SQUIDS.

Table 6.1: Estimated characteristics of the devices, when designed. Note that for the SQREF, the design was slightly changed for this version after the values were calculated.

Device	C_c(fF)	C(fF)	L_l(pH)	L_{loop}(pH)	L_{SQUID}(pH)	n	K(kHz)	$\omega_0(GHz)$
SQREF	13.88	0.764	501		44	1	−90.8	7.54
SQARR	108	1082	273	143	250	20	−28.3	6.3

This does however have an impact on the modulation depth. This is relevant for the influence of the magnetic field, and in this case, a larger critical current may be detrimental. In other ways, it may have a positive impact, could be that aging effects are reduced for nanobridges in comparison to SIS junctions. Another benefit may be the reduction of noise due to the absence of the isolator at the junction. The nanobridges themselves are 3D, and while the rest of the SQUID is 70nm thick and 1μm wide, the nanobridges are only 15 nm thick, 50 wide and 200 long.

6.2. Calibrated measurement of SQUID reference cavity

The first type of measurement is a VNA measurement of the device, with an applied magnetic field, next to the power and frequency of the VNA. Magnetic flux introduces another parameter, as it will change the resonance frequency and the non-linearity, though the couplings may also depend on frequency. We look into the reflection of the signal, the phase shift follows the resonant frequency, and thus we can see how the resonant frequency depends on the magnetic field and the power. The flexibility of the resonant frequency will determine how practical the device is, as JPA only amplifies in a small range but which can be moved with flux. This is mainly dependent on the SQUIDS, so we can expect clearer results here, as there is only one SQUID in this cavity. With the SQUID array one can expect more chaotic behaviour due to differences between the different junctions.

Secondly, by looking at the shape of the curve of the magnitude of the reflection, we should be able to to derive the values of κ and γ in relation to one another, which denote the coupling to the input line and the environment from the device respectively. This should be straightforward for the reference cavity of the device, as that one should be nearly critically coupled.

6.2.1. Uncalibrated versus calibrated reflection trace.

One can spot the cavity on the absolute and phase reflection spectrum, as seen in figure 6.3, as they are indicated by a minimum of magnitude and a phase shift. The cavity frequencies follows arcs to lower frequencies, and at a nearly constant frequency snaps to a new arc with increasing flux. The pattern of overlapping arcs depend on self inductance, and is related to the inductance of the SQUID loop and the SQUID junctions. It depends on the power in the device how stable these arcs are, as with the SQARR cavity in section 6.3, the pump power.

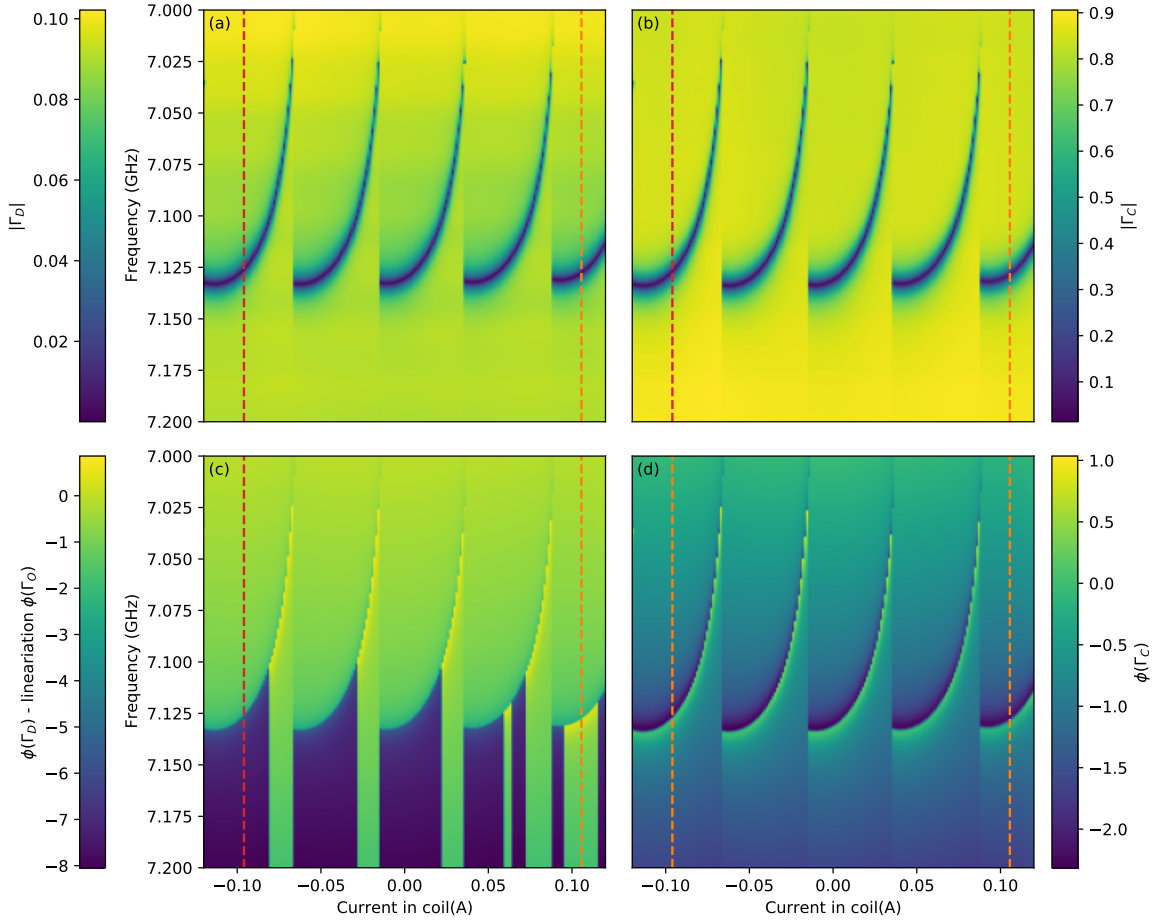

Figure 6.3: The effects of calibration and flux on the reflection spectrum of the SQREF. Where the left column is the raw data, while the right is calibrated. The top shows the magnitude of the spectrum, and the bottom the phase linearized to the same reference. The different dotted lines denote the cuts that are shown in figure 6.4

The unwrapping of the phase seems to have been malfunctioning in the phase plot of the raw reflection spectrum, subplot c, as there seem to be discontinuities at high frequency and increasing flux, which is absent in the calibrated phase plot subplot d. This is not due to our analysis though, and a further look into our way of unwrapping and linearilizing of the phase can be seen in section 9.4.1.

In the magnitude plots, the difference between raw to calibrated has some visible results. There is a slope in the raw magnitude plot coming from increased attenuation in the wires with increasing frequency, which is removed for the calibrated plot. In fact, in the calibrated plot it is the other way around, probably due to the cable resonances of the wire connecting the switch to the device. Another aspect is the range of magnitudes we see in the spectrum, as in the calibrated plot it is 9 times larger, so again attenuation is removed.

The phase plot seems to be more interesting, the calibrated plot shows the cavity clearly with only a small slope, probably due to the aforementioned wire. The raw plot has the same slope, due to using the Open, which is an open spot on the switch, as reference. Sweeping past the cavity seems to either result in a large decrease of phase, or to decrease and increase to result in a similar value as before. This seems to be mostly dependent on the resonance frequency at that point, though not entirely, as there sometimes is a difference between the sweeps at different flux points even though the resonance frequency is similar. The linecuts of this plot can be seen in figure 6.4.

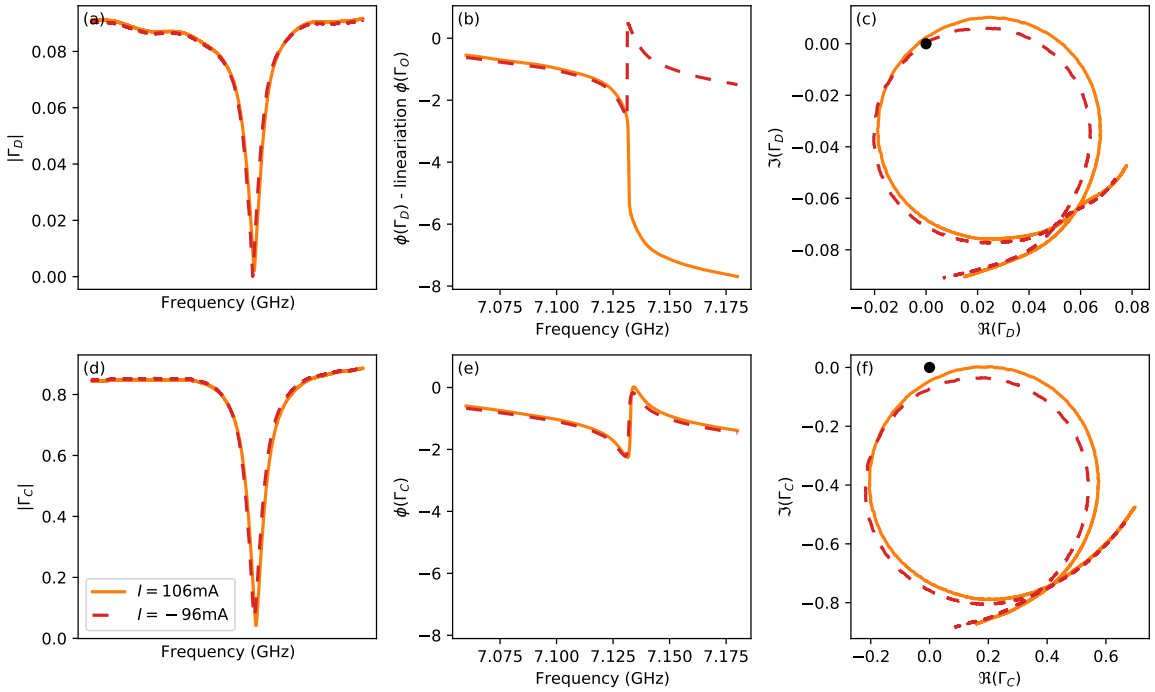

Figure 6.4: Plot of SQREF reflection spectrum for two different magnetic flux points, left column raw to right column calibrated. Middle row shows either a 2π or a 1π phase shift, denoting whether the origin is surrounded by the spectrum, as seen in the bottom row.

In figure 6.4 one can see more clearly what is happening, the phase shift is either 2π, or only 1π in the raw plot, subplot c, while in the calibrated plot we only see a phase shift of one, subplot d. This reflects whether the cavity is over or under coupled, as seen in the bottom row, where overcoupling happens when the origin is surrounded by the spectrum, while with undercoupling it lies entirely outside of the origin. At critical coupling, only a small change in the resonator parameters will change the coupling from under or over. This can be caused by FANO or by general wire resonances, and these can be calibrated out, as long as the source of the effect is before the switch, as described in section 2.6.1.

6.2.2. Cavity resonance of SQUID reference with magnetic field sweep

The cavity resonance can be found in different ways, we know that the phase shift and the minimum of the reflection spectrum coincides with the resonance frequency at low power. This is what we use mainly, and a detailed inspection is given in the appendix, subsection 9.4.2.

Another way is to fit the spectrum to the theoretical expectation, which can give us the parameters of the cavity. This is what we do in the next figure, figure 6.5. The parameters for this fit are found as in table 6.2.

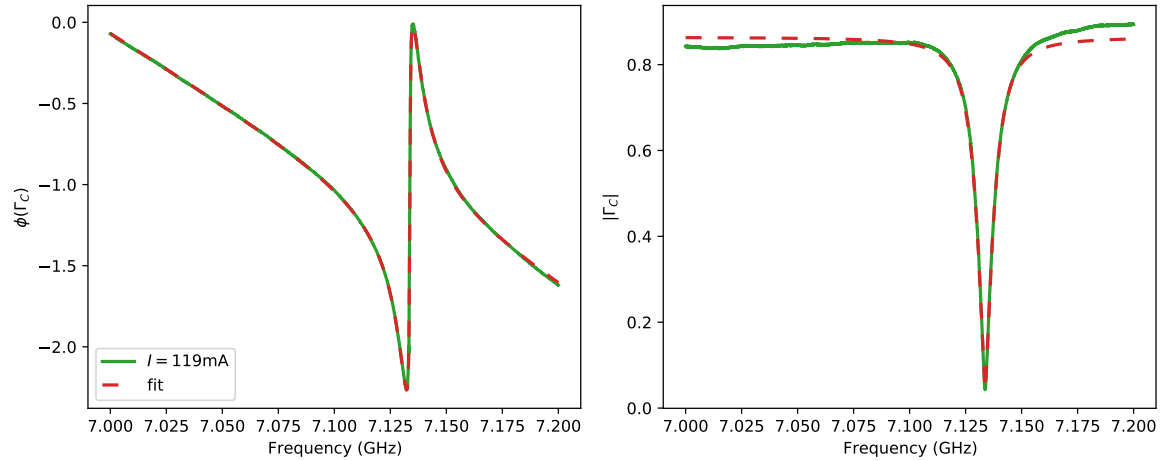

Figure 6.5: A plot of the SQREF response at current $I = 106$mA with a fit. Magnitude in (a) while phase in (b), green being the data while red is the fit.

Table 6.2: Characteristics of the fit from figure 6.5

ω_0(GHz)	κ(MHz)	γ(MHz)
7.134	6.190	6.824

Most of these parameters stay approximately the same for flux, except for the cavity resonance frequency, as can be seen in figure 6.6.

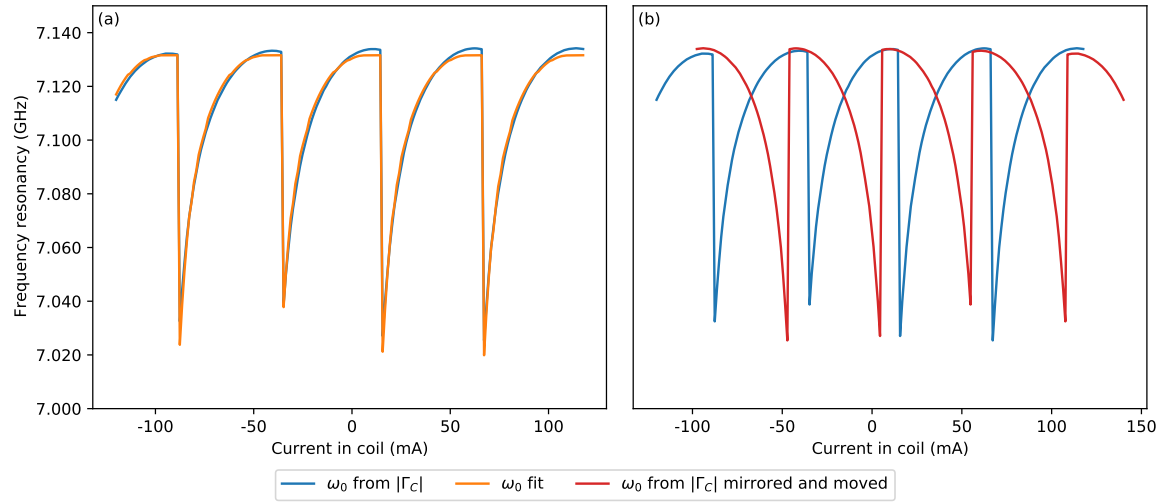

Figure 6.6: A plot of the resonant frequency of the reference cavity in a magnetic field. In subplot (a) this is shown in conjunction with a fit, while in subplot (b) the plot is mirrored to show the width of the flux arc.

Next we can try to find parameters for the behaviour of the resonance frequency in a magnetic field, which is shown in figure 6.6, and denoted by formula 2.87. This is clearly not the behaviour we expect from a SQUID resonator according to the theory, as in figure 2.21.

The arcs are assymetric. In fact they seem to be overlapping, as sweeping in different directions give the other side of the flux arcs we do expect, also the period of the data is different from the width of the flux arcs. Another aspect is the shape of the path, with the theory being much sharper, the flux arcs are now much wider at the top. Our arcs also do not reach zero frequency.

The first difference is due to self-inductance[18], which will result in a different flux going trough the SQUID than the one applied. From the convolution of the resonance frequency in flux, we can find the flux

quantum, and by overlapping the signal with its mirror, we can find the width of the flux arc. Using these values we find a screening parameter $\beta_L = \frac{2L_l I_c}{\Phi_0}$. We find a value in this way of $\beta_L = 2.48$.

The second difference is due to the fact that the inductance does not go to infinity as fast as foreseen. This can be seen as of an inductance outside of the SQUIDs, so our new function becomes:

$$\omega_r = \frac{\omega_0 \cos \pi \frac{\Phi}{\Phi_0}}{\Lambda \cos \pi \frac{\Phi}{\Phi_0} + 1 - \Lambda} \tag{6.3}$$

Where $\Lambda = \frac{L_l}{L_S Q + L_l}$ denotes the fraction of inductance that is not tunable. This inductance can also be caused by small differences in the design of the different SQUID's, or maybe a SQUID with only one functioning arm, as it also results in a different inductance at resonance.

The last aspect, the fact that our frequency does not reach zero can be explained by premature jumping, the value for β_L is only a lower estimate. If there is premature jumping, the arcs will overlap more, but we would not see it. Taking all these factors into account, we get the fit in figure 6.6.a. This is with the values in table 6.3

Table 6.3: Characteristics of the fit from figure 6.6.a

ω_0(GHz)	β_L	Λ
7.132	2.97	0.974

6.3. Calibrated reflection of JPA

In this section we will look at the reflection of the JPA, and its dependence on flux and probe power, beside frequency. The cavity should be overcoupled, and should thus only be visible in the phase of the reflection. Additionally, the cavity should also move with increasing power, which will be dependent on power at the cavity. We do not know the transmission from the VNA to the device, so we do not know its dependence on frequency.

6.3.1. Reflection response of the SQARR at low power

To start simple, we will use a lowpower(-15dBm at VNA) VNA measurment with changing flux, so the influence of the non-linearity will not have a significant impact on the resonancy, and our lorentzian should be symmetric. The outcoming measurement can be seen in figure 6.7.a and 6.7.b.

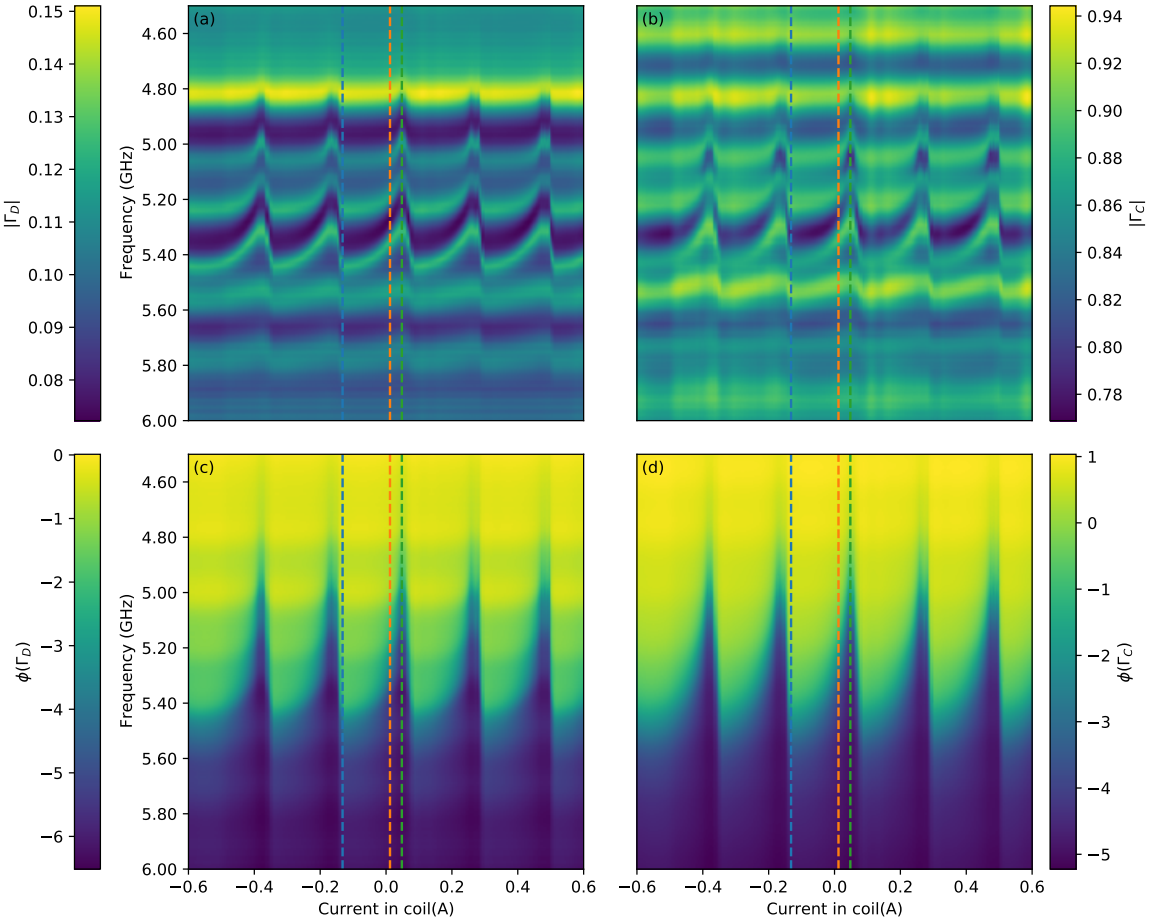

Figure 6.7: SQARR frequency spectrum in a magnetic field, left column uncalibrated right column calibrated, upper row magnitude lower row phase.

In subplot c and d, one can see the resonator frequency move, with flux, in a shape similar to SQREF, although the jumps are at a different point, a smaller part of the entire arc is visible. The attainable shift in frequency seems to be much larger, and the arcs are larger in current, and so the Flux Quantum is larger in magnetic field. Another thing to notice is that the resonancy does not decrease trough the entire flux arc, near the next jump it jitters somewhat upwards, as can be seen in figure 6.10. The magnitude plots do show a dependence on flux, but not in a way resembling a moving cavity, as can be seen better in figure 6.8, which has some linecuts of the 2D plots. Here the phase shifts can be seen more clearly.

The magnitude plots show a dependence on the flux, but not as a moving cavity would, which would increase the reflection on one end while decreasing it on the other. Instead the probable cause is resonances of the wire connecting the JPA to the switch, by changing the phase of the device, which frequencies are constructive or destructive will also change.

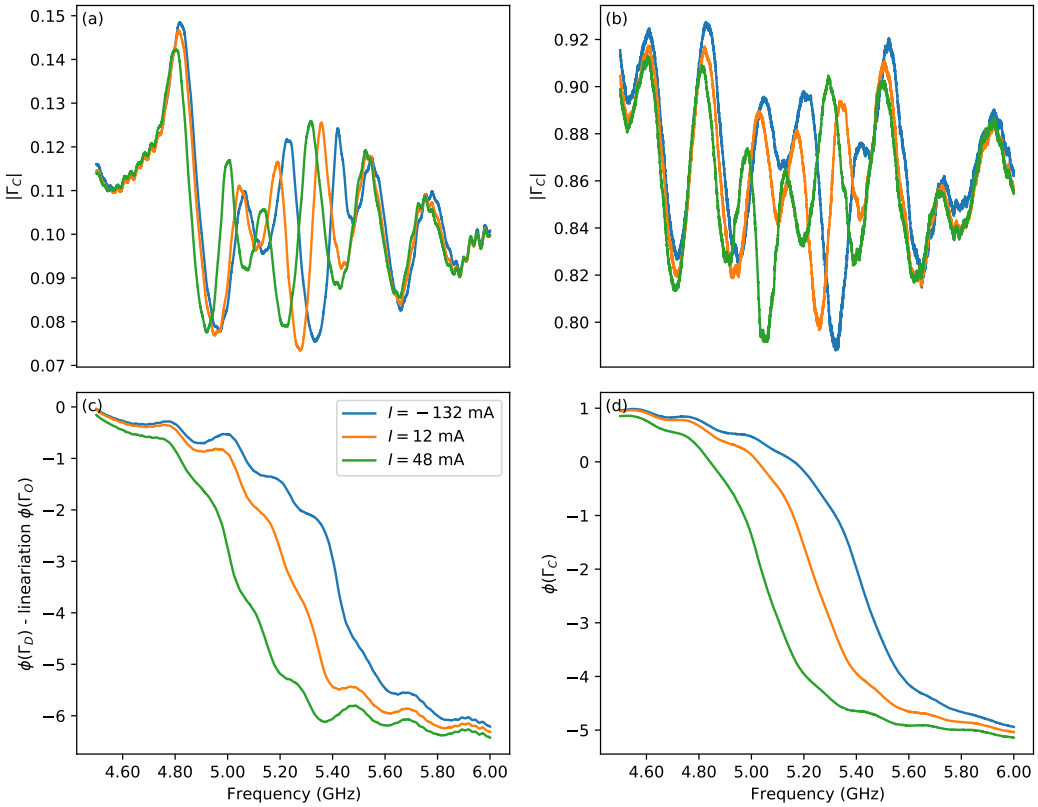

Figure 6.8: Response of the SQARR cavity for various values of flux. The phase plots(c,d) show the movement of the cavity more clearly. The magnitude plots do show a dependence on cavity frequency.

Table 6.4: Characteristics of the fit from figure 6.10.b

ω_0(GHz)	β_L	Λ
5.486	3.13	0.8

Even if it were caused by the cavity, the maximum calibrated absolute reflection difference is on the order of 10%, which gives an upper bound $\gamma < \kappa/20$, so it would still be overcoupled.

The resonance frequency of the SQUID array can still be deduced from the phase though as seen in 6.8 in subplot d, as the phase drop is relatively clear, in addition to the added value of κ to γ. Still, it is harder to get a precise value, as the quality factor is very low, so the entire measurement falls within the cavity, and one cannot get a linear approximation of the phase dependence on frequency of the system in the same way. We will do with fits for the quality factor, and the methods described in subsection 9.4.2 for the resonance frequency.

6.3.2. Cavity resonance dependence of the JPA on magnetic flux at low power

With an additional measurement with the flux sweep reversed, we will look at the resonance frequency flux dependence in detail here. We will also go further to parameterize the flux arcs than with the SQREF. The result can be seen in figure 6.9, in subplot a.

Though with the SQREF they overlap, here they stop a bit short of it, only at the edges overlap the different sweeps. This is due to the screening parameter being larger, resulting in certain flux points having three stable solutions, as depicted in figure 6.10, with the numbers in table 6.4. Back in figure 6.9, we can see the joint fit in subplot b, which seems to accurately fit the two different sweeps.

One question remaining is the jitter at the edges of flux arcs, as can be seen in the measurement data of figure 6.10, which seems to reduce our tuning range. This is because again, our previous formula 6.3 was an approximation, the resonance frequency does not actually go to zero because the inductance only goes to

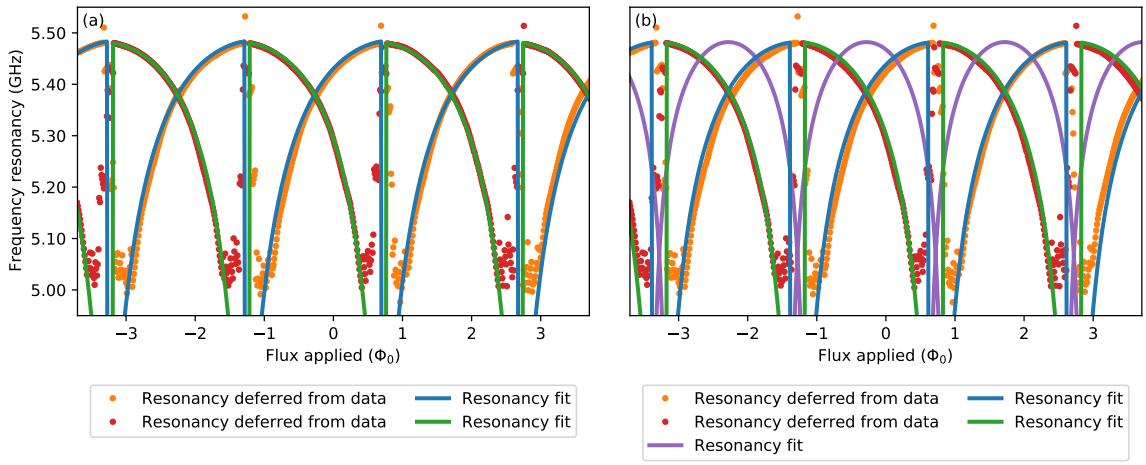

Figure 6.9: Lowpower flux dependence of the SQARR resonance frequency in two different directions. In subplot a two seperate fits for the directions, and in subplot b they are joined together in one fit by self inductance.

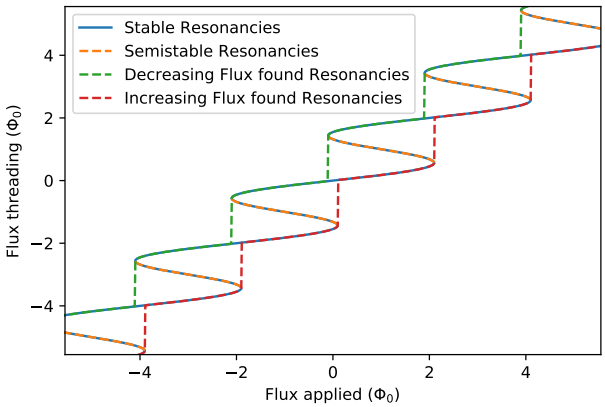

Figure 6.10: Effect of self inductance on the flux arcs for the SQARR, there are at least two stable solutions, and at most three. Sweeping left will result in the Green solution, while sweeping right will result in the red solution. Orange is metastable.

infinity for some solutions to our resonator. This means there are normal modes active at these frequencies, as described in Kim et al. [21].

This problem can not be entirely circumvented, but the effect can be reduced by changing the relation of the Josephson inductance and capacitance to the total inductance and capacitance. This is further described in the recommendations section 7.1.

6.3.3. JPA response change with increasing power

Increasing the photon number of the JPA should decrease the cavity resonance frequency, and make its shape asymmetric. The photon number is however also dependent on the frequency of the VNA, and the power at the device. Since the transmission from the VNA is dependent on frequency, two points of equal power but different frequency at the VNA, might not be equal in power at the JPA. Taking a constant flux and increasing the power of the VNA will get the result in figure 6.11.

The phase shift due to increasing power can most clearly seen in the phase plots at the bottom, while in the magnitude plots one can most clearly see a collapse in the reflection spectrum at high power. This can be from heat generation from putting too much power through, and so is dependent on power at the JPA, and so is dependent on cable resonances, as can be seen in figure 6.12,[23] though an instability may also be at fault. This would entail that the phase change caused by a photon state change in the JPA would cause the interference to be either constructive or destructive.

In the raw magnitude plot we can see that the collapse coincides with a point of high transmission. This

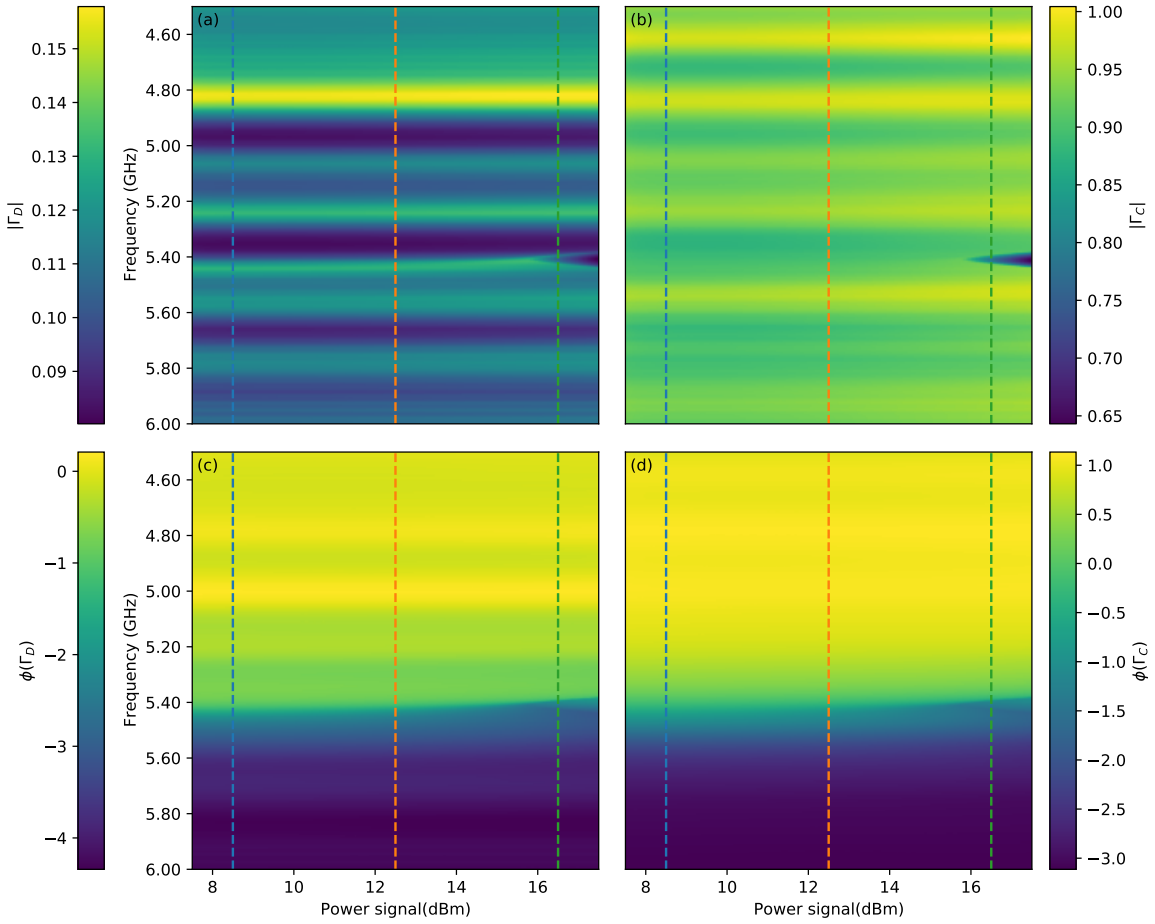

Figure 6.11: Reflection spectrum of the JPA with constant flux and increasing power, on the left column uncalibrated, while on the right column calibrated.

is true for other flux points as well, and so indicates that this is dependent on absolute power, and thus, cable resonances and flux.

Due to the fact that the JPA is non-linear, and the calibration method only measures $S_{21}S_{12}$ as a whole, we cannot get a good measurement of how much power this exactly is, and how it is altered by frequency. This makes the characterisation of the JPA difficult, as this makes the frequency shift dependent on power. We can gain some information from this though, if we assume that at every frequency the JPA has the same phase shift for the same power, we should be able to get transmission coefficients for the in and out line. A more robust approach would be to calibrate this out, which demands an altered setup. The collapse is due to large power influencing the non-linear behaviour, as in Kurter et al. [23], for now, we will take a closer inspection of the phase, as seen in figure 6.12.

We see in the phase plot of figure 6.12.d that the collapse happens far before the bifurcation regime, which would have an almost vertical phase slope, and thus before we can reach a photon number state necessary for high gain. Following the phase shift and its slope, we can however find a value for the photon number state, as of formula $\delta = 4\xi$, 2.105. Doing this for each flux points should give us enough information deduce the five parameters of the JPA, though there maybe an impact by a differing coupling to the environment. The result can be found in the next section.

6.3.4. Cavity frequency dependence of JPA on power and magnetic flux

Using our way to find the resonance frequency, we can get graphs for the different power, as seen in figure 6.13.

We can still see the dependence on flux, but now also the shift due to the power of the JPA. At some point we will have a collapse, which is dependent on the cable resonances, if too much power will go trough the device, there will be heat generation. Question is whether this will limit our photon number state, but this

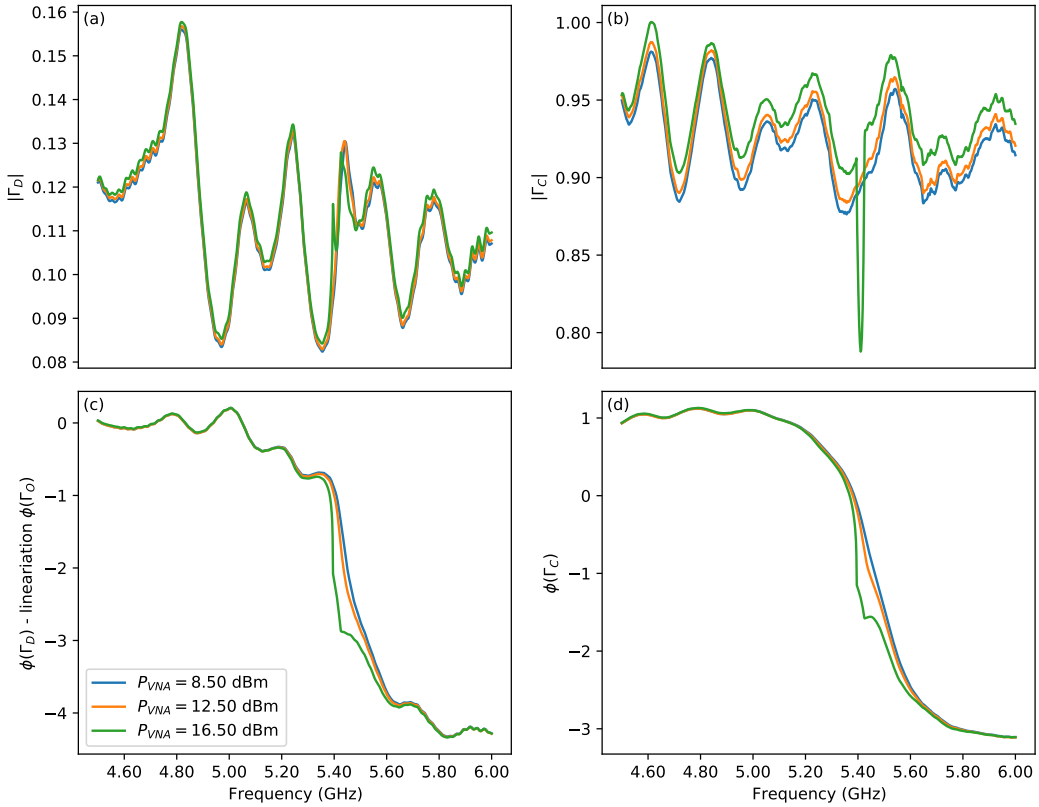

Figure 6.12: In these plots we can see linecuts with one value of flux but several values of power, we can see the collapse(a,b) and phase(c,d) shifts move more clearly, they also seem to depend on the cable resonances. This is true even with calibration, since the JPA its spectrum is dependent on power at the device.

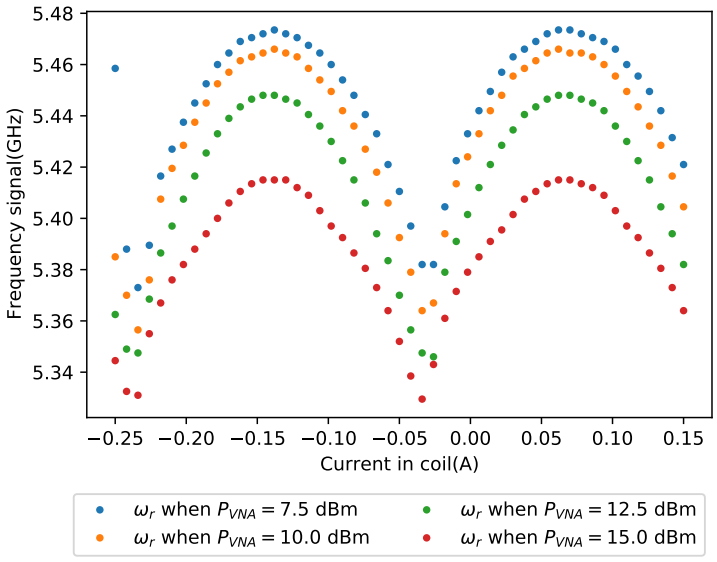

Figure 6.13: Resonance frequency of the JPA for different flux and power of VNA.

does not seem to be the case, as different flux points have different points at which the collapse happens, the blue line in figure 6.14.

To find the JPA parameters, we can look at the changing shape of the phase shift, and deduce the parameters from there. The result is in the right subplot in figure 6.14, where the orange line denotes the critical power. As one can see, we never reach the bifurcation regime, limited by our setup or the heat generation in

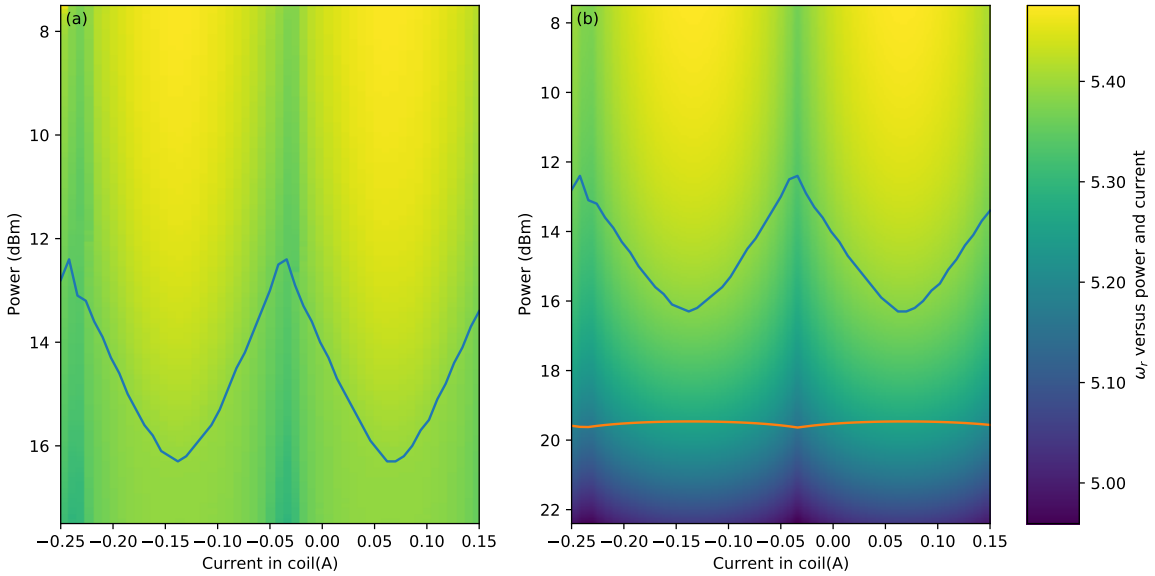

Figure 6.14: Resonance frequency of the JPA for different flux and power of VNA. On the left is the calibrated data, and on the right a fit with extended power. Blue line denotes the power at which point the collapse becomes apparent, while the orange denotes the critical power. The fit does not take the dependence of K on flux into account.

the JPA. According to the fits, we still would need to double our power, which would also limit our gain to be below 10 dB, as per equation 2.119. A way to improve our setup to reduce or remove this problem is discussed in section 7.1.

6.4. SQARR transmission measurement with pump applied

The second type of measurement is a VNA measurement with a signal generator standing in for the pump. Now we can actually do gain measurements, and we should be able to check the parameters of the system as deduces in the previous section. Though in previous work the gain was just gained by subtracting the pump-on measurement by the pump-off measurement, here we use the calibration to get a different picture of the gain. This will negate the problem of the device having a loss when the pump is off, since it practical use depends on the net gain of the entire chip.

6.4.1. Calibrated versus uncalibrated gain

First we started to look for gain manually, increasing the pump power when the pump is at the resonant frequency, and then decreasing the pump frequency to the cavity. We were able to find a "raw" amplification of about 25dB directly on the VNA, by subtracting the spectrum without pump from the spectrum with pump in figure 6.15.a. We were limited by either the maximum power of the signal generator or the collapse through heat generation, depending on frequency. We never reach the bifurcation regime of the JPA. We were aiming for about 20dB of gain.

We can see the in the uncalibrated phase plot in figure 6.15.b that the phase shift appears almost vertical, this would indicate that we are close to the maximum attainable gain for this frequency, beyond this we would get in the bifurcation regime. We have not tried to gain additional insight in this regime, as we have not sweeped in both directions in frequency. The semi stable middle state is hard to reach, as it cannot be entered by simply sweeping from one side, though it is possible to find it by increasing the pump at the right frequency. The calibrated phase plot reduce the angle at resonance, so the bifurcation regime is actually not that close. Because we were limited in both pump power and power through the JPA, it was not possible with this setup, though it might not even be possible with this device.

However, when calibrating the raw data, more than half of the gain vanishes. Taking a look at the calibration data in figure 6.16.a shows why: there is a lot of reflection back into the device S_{22}. Note that for the power, one has to square S_{22}, which means at least about 10% gets reflected back. If this is amplified again, then the output will become boundless if amplification is on or above 10dB. In the setup described in section 4.3, anything between the switch, the directional coupler and the isolator is suspicious. Though another

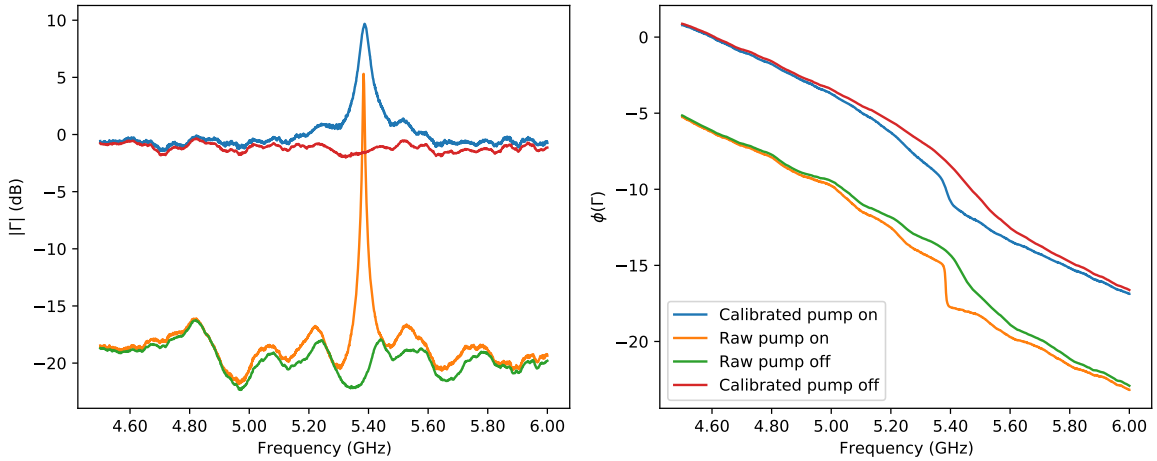

Figure 6.15: Amplification by the JPA, with manually chosen magnetic field($I = 0.34$A) and pump($\omega_p = 5.384$GHz, $P_p = 15.48 dBm$).

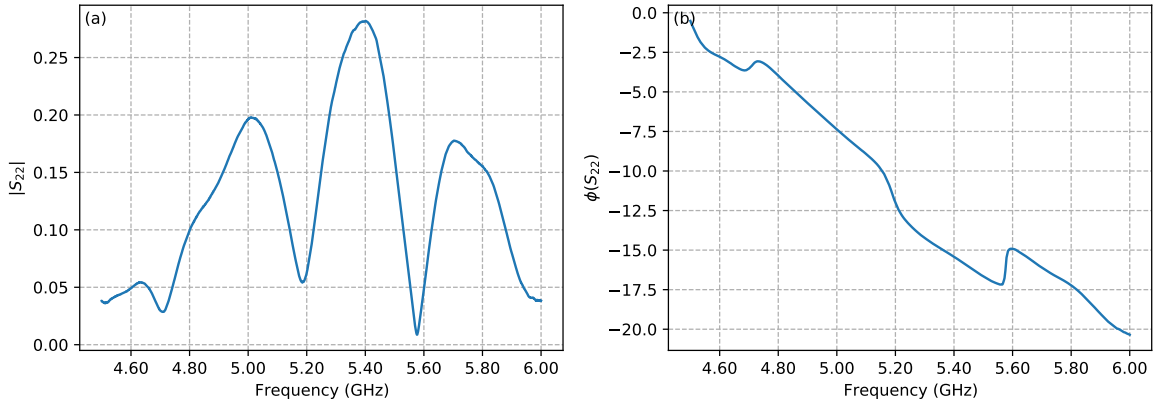

Figure 6.16: S_{22} is the reflection back into the JPA, which limits the maximum calibrated gain, depending on whether it is constructive.

try was made after replacing these parts and the wires between them, and checking at RT whether the S_{22} was sufficiently low, after cooldown the values were unsuitable again, as can be seen in figure 6.23. Looking at the parts we can see we may have been optimistic, as the isolator has a denoted isolation of -18dB, so at most 18dB could be measured if no other parts would play a role. Another slight change in the setup could solve this problem, though these parts need to be tested at the fridge base temperature. A way this may have been subverted is by applying some attenuation in front of the switch, which will be calibrated out, though the "actual" amplification is obviously less, which may be a problem for other purposes. We cannot make a definite conclusion about how much gain can actually be achieved with this device, though we know it is at least about 10dB. One could rely on destructive interference to find a higher calibrated gain, but that only works for certain frequencies, and getting the JPA pumped optimally at a specific frequency is difficult, as we need to pump close to the ideal value with about 1 MHz, and in power with about 0.1dB, at 15.5 dBm. Also the magnetic flux used to change the resonance frequency changes the JPA parameters, beside the fact that the transmission value is different. So, a broader approach would not be useful to find a higher calibrated gain. Its dependence on the resonant frequency, and thus, the reflection coefficients, can be seen in figure 6.19

6.4.2. Calibrated gain at different flux points.

Since the resonance frequency is dependent on photon number and magnetic flux, it is not trivial to ideally pump the system at different flux points. So we use a workaround, we sweep the flux and for each flux point the pump frequency, while keeping the pump power constantly high. This will result in less gain then in the previous section, due to being less accurate in nature. We expect the flux tunable range to be similar to the amount we could shift the resonancy, as seen in figure 6.9, being about 8 GHz. If we do this measurement and then look for the highest peak, we can get the 2D plots seen in figure 6.17.

Though there is a lot going on in the subplots, in each the effect of flux can be seen, with in the middle and at the edges nearing an integer flux quantum. One might see in figure 6.17 that the flux arcs do not align with the previous plots in current for example figure 6.7, these data was taken during a later cooldown, and the magnet needs to be connected and disconnected each time, so the direction of the field might have been swapped. Another thing are the strange blobs that are black and yellow at certain frequencies and magnetic fluxes, this is due to the found peaks being outside the range of the 2D plots. This happens when the reflection spectrum collapses due to heat generation, which practically limits the state of our JPA.

Secondly, it is quite clear that the resonance frequency is much lower than the frequency of the peak, as seen in the top two subplots, which means that it is not optimally pumped. In hindsight sweeping pump frequency downward instead of upward would have been preferable when looking for high gain, since increasing photon number means a lower resonance frequency, as can be seen in section 2.5 With increasing frequency, when the pump gets closer to the optimum, the resonant frequency decreases due to the larger photon number, which can cause it to move past the pump. If near or in the bifurcation regime, this could provide instability as the resonant frequency will increase again, though it is unlikely it moves back before the pump. This is probably the reason for the jump in resonance and peak frequency between 5.4 and 5.47 GHz.

Thirdly there is a band of amplification where the pump frequency is close to the peak frequency, but there is also at certain magnetic flux amplification when the pump is near 5.35 GHz. One could think that the device reaches a photon state where the resonance frequency decreases enough to be stable, but that does not explain the lower amplification between the blobs and the band. It also does not follow the same band as the other amplification structure. It is also much to low to be explained by flux tunability, as the difference is more than 100 MHz as can be more clearly seen in figure 6.18, while we could tune the resonance by at most 80MHz without jumping, as can be seen in figure 6.9.

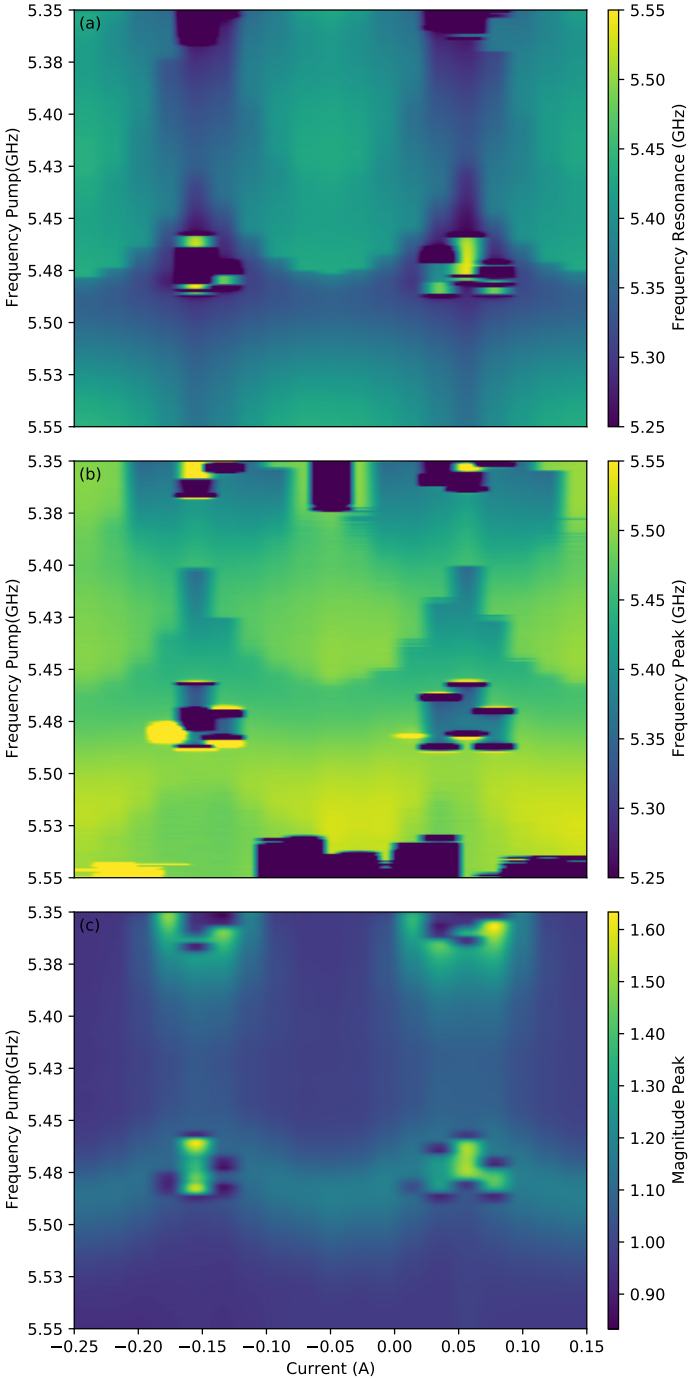

Figure 6.17: With changing magnetic field and increasing pump frequency, we can find the resonance frequency at the top, the peak frequency at the middle and the peak amplitude at the bottom.

The problem is probably due to the fact that the photon number state of the JPA depends on and is sensitive to absolute power. So even if the detuning is larger, if pump power is larger at the device, it can show higher gain. We explore this idea in subsection 6.4.3

With all the trouble mentioned in the previous paraghraphs, it is difficult to show any flux tunability. But within the lower bands most clearly seen in figure 6.17 subplot c, we can find the green and orange linecut of figure 6.18, which give us a tunabilty of about 12 MHz. The shape of the gain peak is also very different from the asymmetric Lorentzian we expect, which we dive into in the next subsection.

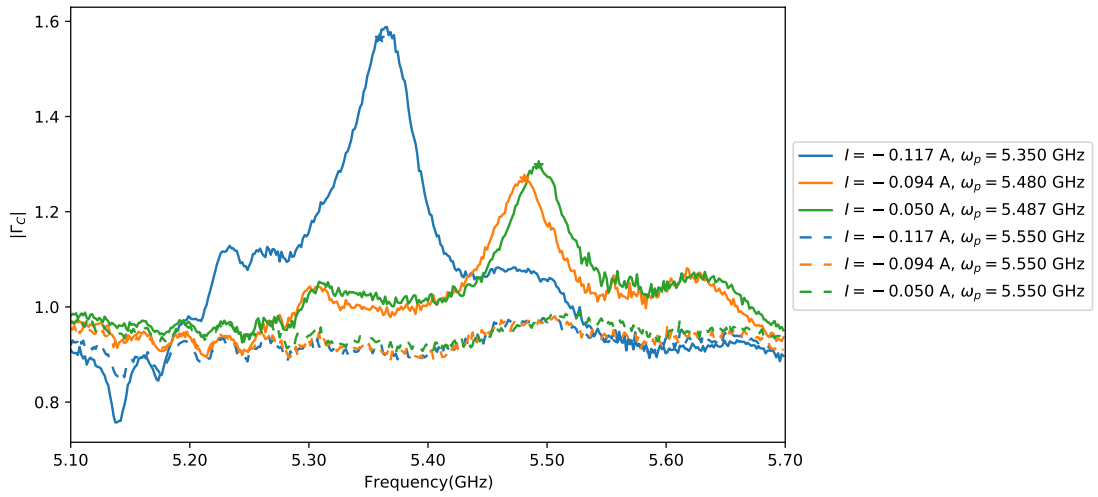

Figure 6.18: The calibrated absolute reflection spectrum for three different flux and pump frequency settings. The start denote the peaks, where the flux tunability can be seen between the green and orange linecut, while the difference with the blue is due other reasons. The dotted lines are comparisons with low photon number states, as they are very far detuned.

6.4.3. Calibrated gain with increasing pump frequency

We still have two questions: Are the two different gain bands due to higher pump power at the device? And why are we not getting a Lorentzian shape for the gain peak? We will start answering these questions by looking at the data of one flux point, the resulting 2D plot can be seen in figure 6.19.

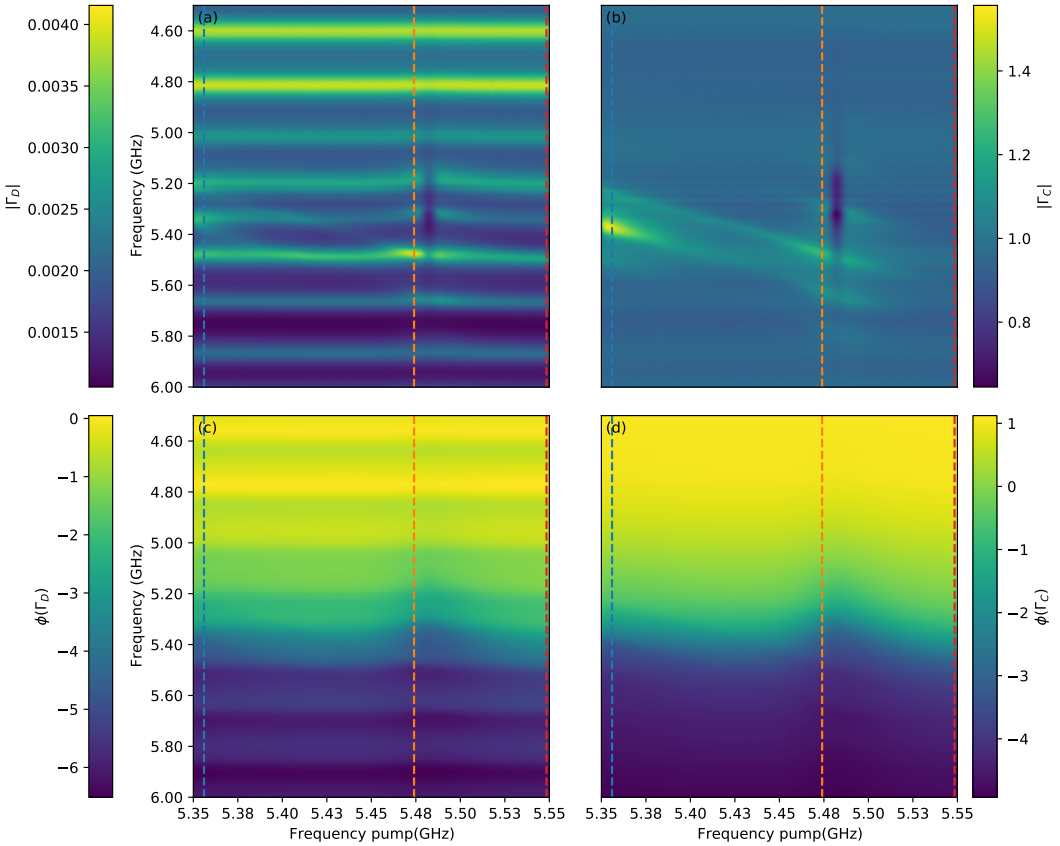

Figure 6.19: Amplification by the JPA, with changing pump frequency. We can see a collapse in both the magnitude plots, a,b, and we can also see that the two peaks actually follow the pump, and not the resonances. In the phase plot the resonance frequency seems to reset, which could be due to a flux jump.

In the figure we can see the pump frequencies where the high gain happens, which indeed seems to be near the points where the raw reflection spectrum is at its maximum! We take two linecuts, the blue and the orange, to see this more clearly, and the green one to compare, which can be seen in figure 6.20, and we can see they exactly align with frequencies where the transmission peaks. This results in the raw reflection data to be apparent in the calibrated reflection data,

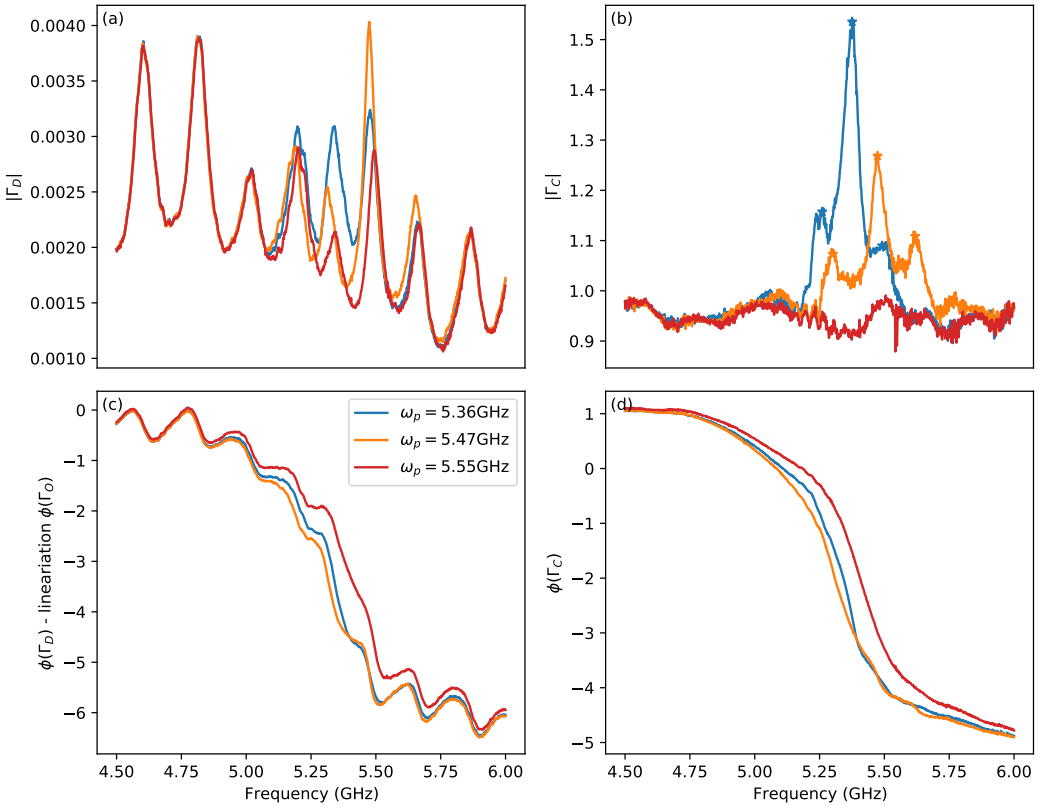

Figure 6.20: Amplification by the JPA. By moving the pump closer, we can see the gain increase in the absolute magnitude plots(a,b), while in the phase plots, we expect to see a slight phase shift, but this is not clearly visible.

In figure 6.19 we can also see a collapse, which is probably due to heat generation, even though higher gain was achieved at a different pump frequency, which may indicate that the point at which heat generation starts could be dependent on frequency, and thus the gain achievable would be dependent on frequency.

The question of the shape of the gain peak does seem a bit harder though, as it seems there are side peaks, which follow the main peak and thus the pump frequency in an almost linear fashion. This means that the transmission of the system cannot explain this, as that is independent on the pump. It does not follow the pump frequency exactly though, as the peak frequency increases about twice as fast as the pump frequency. Which makes it even stranger, why would the gain peak not follow the pump frequency?

It may have something to do with faults in the design, though that may be hard to test. Another possible solution is the backreflection, if this results in a feedback loop this would cause larger gain for frequencies where it is constructive. Since there is a linear phase increase with increasing frequency over a wire, this would result in sidepeaks being exactly 2π in phase apart, and a fairly constant difference in frequency.

We test this idea by finding the peaks of all our frequency sweeps in this measurement, and than looking for the difference between neighbouring peaks, this results in figure 6.21. The frequency difference is straightforward, but the phase difference is found by adding S_{22} and Γ_c their phase and calculating the difference at the frequencies of the peaks. The phase of S_{22} can be seen in figure 6.23.

Which agrees quite well with our hypothesis! The question is, why? Since we get the phase difference from our calibrated phase and our S_{22} phase, this should be removed by our SOL calibration, as we have seen with our gain plot in figure 6.15. The answer might lie in what we cannot see, the idler gain. If the idler gain of the idler gain constructively interferes with the signal gain, we would expect to see higher calibrated gain, as this path is not calibrated out by the SOL calibration. This may also explain why the amplification peak changes

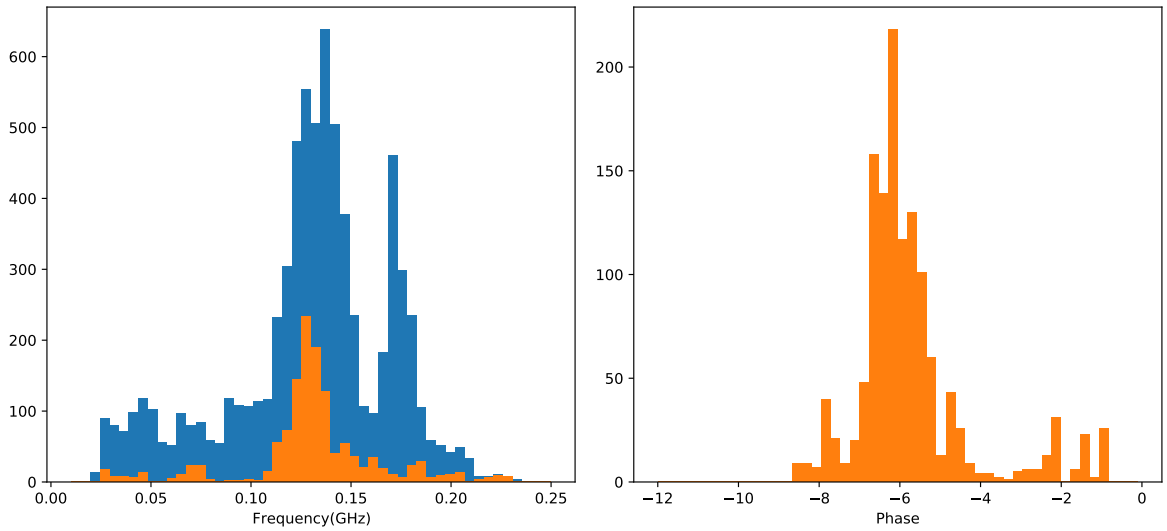

Figure 6.21: The difference in between the peaks of the gain measurement, with on the left in frequency. The difference between the blue and orange is the minimal height to consider it a peak. On the right the same peaks, but now the difference in phase, with $\phi(\Gamma_c)+\phi(S_{22})$.

with pump frequency, as just constructive feedback on one frequency remains at fairly constant frequencies. We look into the phase of the idler in figure 6.22

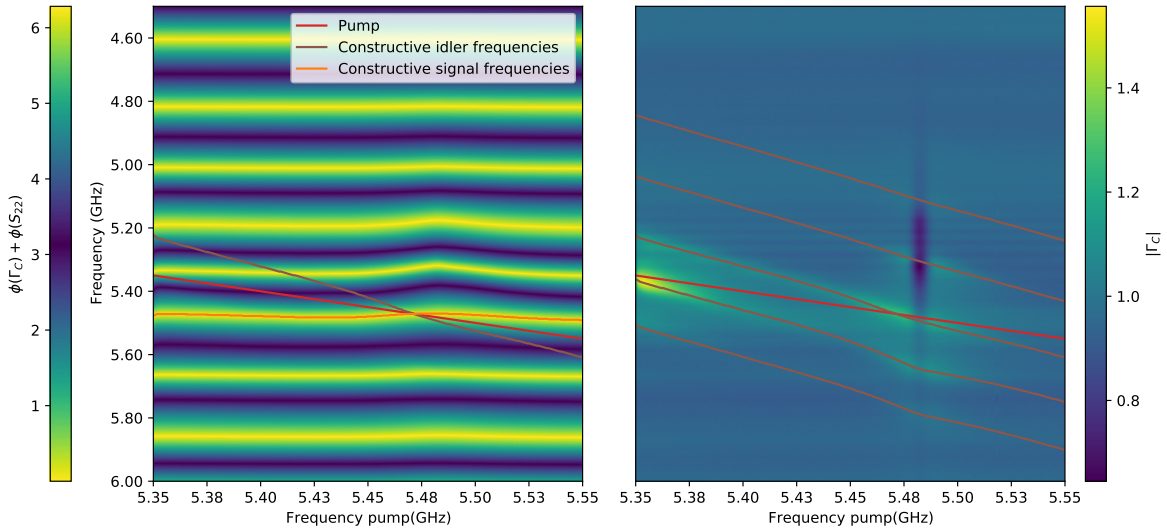

Figure 6.22: On the left the phase plot of the path of interference, with the orange line frequencies with a constructive signal frequency and brown frequencies which have a constructive idler frequency. These are also shown on the right together with a magnitude gain plot.

In the figure we can see on the left the phase of the path of the backreflection, where constructive interference is reached near 0 or 2π of added phase. One of these frequency points results in the orange line. But the frequencies mirrored around the pump have an idler frequency that has constructive interference, the brown line. We can see that these frequencies also result in lines 2π in phase apart, and coincide nicely with our magnitude plot, seen on the right. This answers the question of why the gain peaks are shaped oddly, but this also means that the gain further from the pump is inaccurate, despite our calibration.

We cannot calibrate this out since we do not have a transmission measurement of the idler gain, as that requires measuring the transmission between two different frequencies, though this can be done in future measurements, as seen in section 7.2.

We can however say that such a JPA is feasible to use for gain and can be tuned by flux, though care must be taken with these flux arcs. JPA's like the one of Planat et al. [28] do not have overlapping flux arcs, which may be easier to achieve with the SIS junctions they use, which results in a lower critical current, while keeping

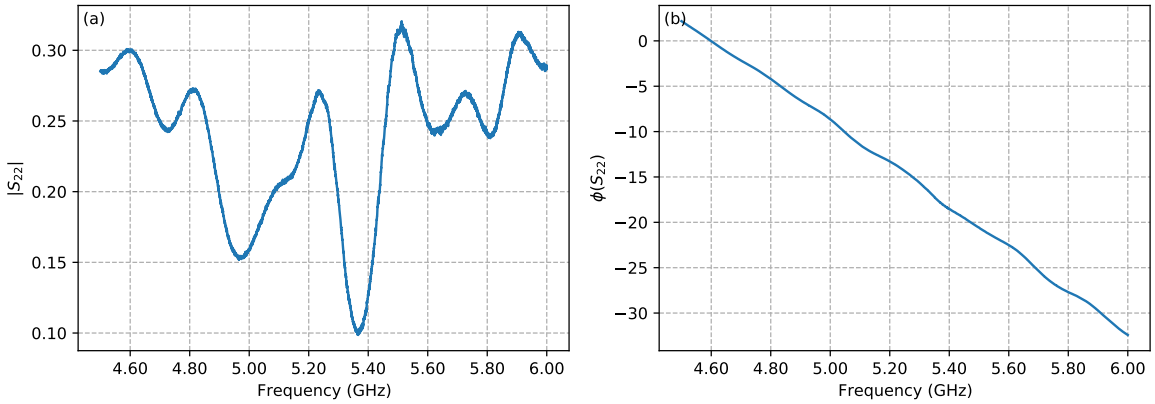

Figure 6.23: S_{22} is the reflection back into the JPA, which limits the maximum calibrated gain, depending on phase. The frequency for a phase shift of 2π is about 270 MHz in S_{22}. This is an upper bound for this frequency range, as one should also take the contribution of the wire from the switch to the JPA into account.

other parameters the same. One can try to reduce the critical current of the nanobridged by changing its dimensions, though the self inductance should be reduced by decreasing the inductance of the loop relative to the junctions. For higher gain one can just tinker with the JPA as well, though a simple solution is to reduce the amount of SQUIDs in the array. A more detailed recommendation is in section 7.1.

6.5. JPA noise

Another aspect of a JPA is that in theory it is a quantum limited amplifier, the lowest amount of noise possible is added before amplification.Aumentado [2] To measure the input noise of our device, setup is changed as follows, carrier cancellation is useful to make sure we do not affect the measurement on the spectrum analyzer by providing too much power, but it also influences the calibration, though that might not be significant, as there is a lot of attenuation in the carrier cancellation circuit. One thing we need is the gain of the JPA, which is taken raw from figure 6.24. We can finally also see the idler gain, though it does not follow the simple rule together with the signal gain, as in equation 2.121.

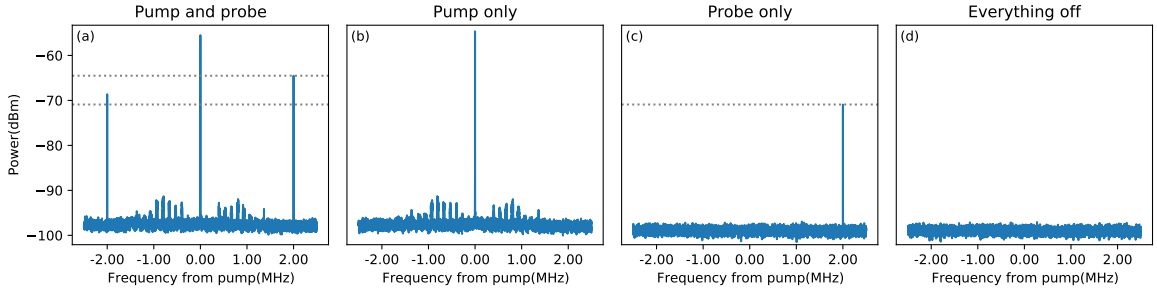

Figure 6.24: SA measurement of the JPA, without calibration, with as pump frequency 5.477 GHz. Gain is deferred from the difference in amplitude of the probe with and without pump, the two gray lines. We can also see here that the probe and idler don't follow equation 2.121.

This is probably due to two things. One, the cable resonances transmit one frequency better than the other, which results in a different relation, this can also result in an idler gain higher than the signal gain, which I have also found in certain cases, not depicted here. Two, the reflection back into the JPA is large for the idler, that it than gets amplified and has its own idler, which is than at signal frequency. Note that this reflection is highly phase dependent, as it means the difference between either constructively or destructively interfering. The same mechanic is behind the behaviour that can be seen in figure 6.22.

6.5.1. System power calibration using noise of load

Now, for the gain of the main line, we run into the same problem, that we cannot distinguish the cable transmission values of the input line from the output line. To circumvent this, we can find the amplification and base noise temperature trough the linear dependence of noise on temperature, as described in section 3.5. We do not have a load of which the temperature can be controlled independently in our setup though, so instead we heat up the entire sample plate of the fridge, depicted as the 300mK line in figure 6.25. The relation of the necessary values for the calculation of the input noise from this figure, are given in the next equations:

$$P_1 = A_{main}\,(N_{main} + P_4) \tag{6.4}$$
$$P_4 = A_D\,(N_D + P_0) \tag{6.5}$$

Where $P_0 = k_B T_0 \Delta f$ is the Nyquist noise, P_x is the power at points depicted in figure 6.28 and A_{main}, A_D denote amplification of the amplifier chain to that point and the device respectively. N_{main} and N_D is used as the input noise of these amplifiers, the noise that remains at zero temperature. We want to know the noise of P_5, but with our noise calibration we can calibrate to either P_4 with switch set to the load or P_8 with it set to the short or open, as these are points where a load is connected to directly. P_8 gets its contribution from the load on the isolator, though there will also be a contribution from P_9. We do not know the transmission values of the connection from the JPA to the switch, so we assume that the transmission and attenuation difference between the short and the JPA does not have an impact on the calibration. With these assumptions, we get the resulting equations for the noise calibration:

$$P_1 = A_{main}\,(N_{main} + P_8) \tag{6.6}$$
$$P_8 \approx P_5 = A_D\,(N_D + P_6) \approx A_D\,(N_D + P_0) \tag{6.7}$$
$$\tag{6.8}$$

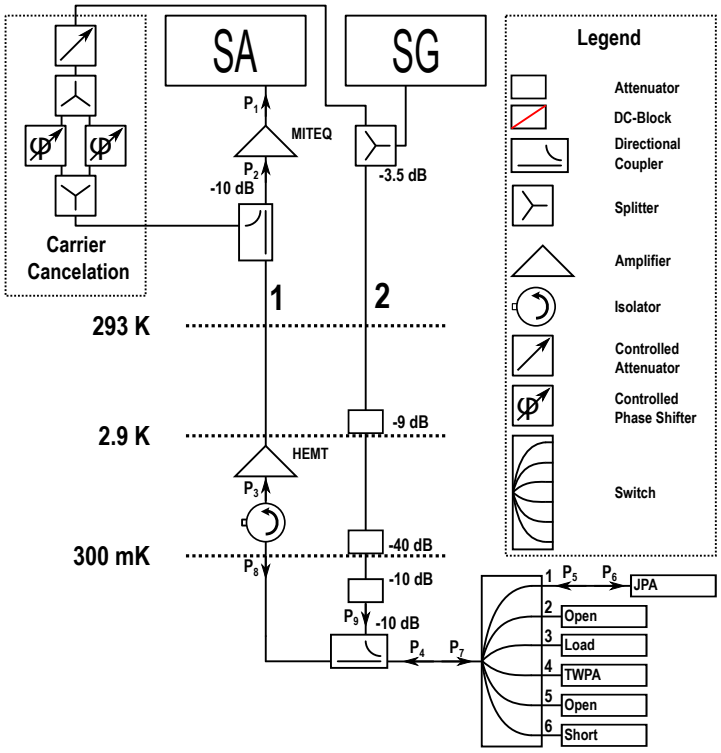

Figure 6.25: Variables for power for the different reference planes used in the noise calibration. P_1 is the measured power on the spectrum analyzer(SA). The VNA is omitted for clarity, the detailed setup can be seen in figure 4.4.

With the values we find with these equations we can calculate the input noise, for a normal amplifier:

$$A_D = \frac{P_5(D_{on})}{P_5(D_{off})} \tag{6.9}$$

$$N_D = P_5(D_{off}) - P_0 \tag{6.10}$$

$$N_D = \frac{P_5(D_{on}) - P_0}{A_D} \tag{6.11}$$

Where $P_x(D_{on})$ is the power with the switch switched to the device, which is on, at location x. The first active part in the main amplifier chain is the HEMT, and so we can assume everything on the sample plate is part of the same noise floor. Since the main plate has a higher temperature, the wire and connectors to it will have a temperature falling between the plates. If they have attenuation, they will contribute some additional noise, =we assume that this noise is at most linearly dependent on the sample plate temperature. The noise source for the short and open is mostly the load connected to the isolator, though there could still be differences between them due to cable resonances. Another option is the load at the switch, which should give a higher noise power at the SA, as there are less wires between them. The short was chosen at this point, because it was used for default, and the dependence of the noise floor on this chosen was not understood completely at this point. For the short we now have a noise measurement at many different values of temperature, while for the load and open we only have two, as seen in figure 6.26.

The results of the separate noise calibration measurements differ enough from what we expect to show one needs to be cautious with deferring a conclusion. The two graphs seen in figure 6.26 a have an offset between each other, though the slope is also slightly different. We expect this to be due to the fact that the main plate temperature differs between the two with about 2.1K. Though the linear dependence of the data seems to agree with the fit, there is still significant deviation, as seen in 6.5. For this we assumed the points are independent beyond temperature, which is approximately true, due to the fact that the procedure in getting the sample plate stable at different temperatures may cause errors to be temperature dependent. A detailed discussion on this can be found in section 9.3.1

With the fits from figure 6.26 we find multiple answers for base noise temperature and amplification of the main amplifier chain, as shown in table 6.5. As mentioned in section 3.5, these are related due to the

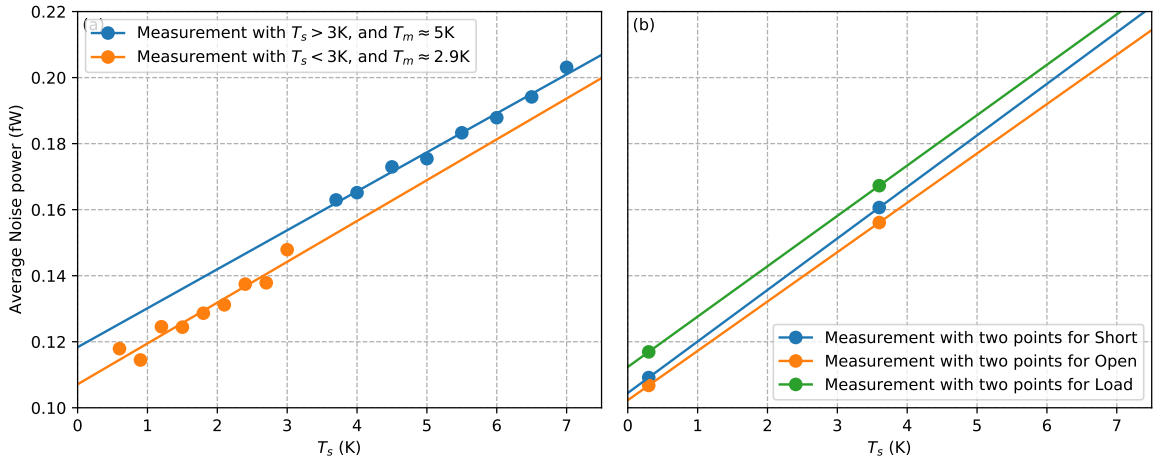

Figure 6.26: Results of temperature versus noise measurement for the purpose of thermal calibration. In subplot a one can see the short at large sample size with different main plate temperatures, while in b for the different loads with sample size of 2.

Table 6.5: The results of the noise calibrations used on short, open and load. For short two measurements at different main plate temperatures with sample size $n > 2$, and the others with sample size $n = 2$. As one can see, N differs much more than AN, where A is the amplification and N is the input noise of the main amplifier chain. The deviations convey the uncertainty of our measurements, though note that with * the deviation is extrapolated from the measurement of the Short at $T_m \approx 5.0$K, taking into account the different sample size.

Measured Device	T_m (K)	n	$\cdot 10^3 A$	N(K)	AN(pW)	σAN(%)	σA(%)
Short	≈ 5.0	8	855	10.03	118.3	2.2	4.1
Short	≈ 2.9	9	895	8.66	107.1	2.3	10
Short	≈ 2.9	2	1130	6.69	104.5	4.9^*	21^*
Open	≈ 2.9	2	1082	6.84	102.3	4.9^*	21^*
Load	≈ 2.9	2	1105	7.37	112.4	4.9^*	21^*

transmission between the reference planes, though cable resonances and attenuation will complicate this relation. Even so, AN_0 should be more or less the same, if we expect the heat independent noise to stem from the amplifier chain. This is not found in the results however, which could be due to the uncertainty of our measurements, as can be seen in table 6.5. Note that this method does not convey the entire picture of transmission, since phase differences can cause a difference in transmission and thus noise, and the JPA its phase reflection depends on whether and how much it is pumped.

6.5.2. Estimation input noise of JPA based on noise calibration

With the noise power at the relevant points in the system found by the noise calibration, we can try to defer the input noise of the device, using the equation in the previous section. The JPA differs from a regular amplifier, as it should not add noise when it is not pumped, as it should then act as a regular overcoupled resonator, with $|\Gamma| = 1$, as can be deferred from equation 2.111.

$$P_5(JPA_{on}) = A_{JPA}\left(P_6 + N_{JPA}\right) \tag{6.12}$$

$$P_5(JPA_{off}) = P_6 \tag{6.13}$$

$$N_{JPA} = \frac{P_5(JPA_{on}) - A_{JPA}P_5(JPA_{off})}{A_{JPA}} \tag{6.14}$$

However, we get nonsensical results, as we get a negative input noise $N_{JPA} = -0.41$K, this is due to errors in our assumptions for our noise calibration. It could for example be due to that the transmission is much higher for the JPA then for the short due to a phase difference due to sheer coincidence. If we take a closer look by putting the equations of the noise calibration into our last equation, we can see more clearly the impact of the values from the noise calculation on the found input noise, as seen in the next equation. By changing the found values with a percentage while keeping the other parameters constant we can get an idea of the impact

of the errors of each parameter, as seen in figure 6.27.

$$N_{JPA} = \frac{P_5(JPA_{on}) - A_{JPA}P_5(JPA_{off})}{A_{JPA}} = \frac{P_1(JPA_{on}) - A_{JPA}P_1(JPA_{off}) + \left(A_{JPA}-1\right)N_{main}}{A_{main}A_{JPA}} \tag{6.15}$$

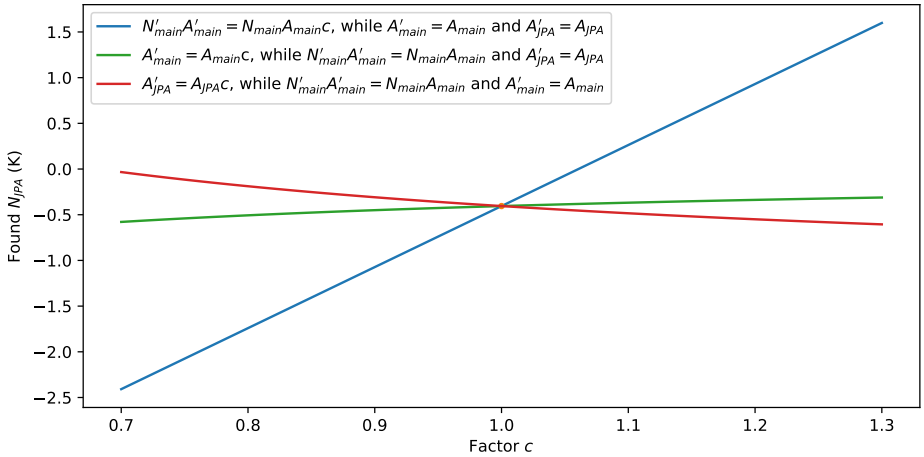

Figure 6.27: The impact of errors in the noise calibration and the amplification of the JPA on the found input noise by equation 6.15. Especially NA has a significant impact(blue line), as it can change the sign and order of magnitude of the result with an error < 5%.

We can see here that this can have two reasons, either we overestimate the amplification of the JPA, or we underestimate the input noise of the main amplifier chain at this phase and frequency. The second one is the most likely case, as only a few percent difference can swap the sign of our result, and this is within one standard deviation of our calibration data, as can be seen in table 6.5.

6.5.3. Carrier cancellation

Beside differences in cable resonances, it could be that the carrier cancellation impacts the amount of noise on the SA, and since it is on when measuring the JPA, and off when it is measuring the rest. In figure 6.25, we assumed the contribution of the carrier cancellation to be constant or negligible, but this is not true, as can be seen in 6.28. This can be deferred from the fact that there is a difference between the measured noise power when the carrier cancellation is on and off, when the pump is off(blue and orange line).

This is probably due to oversights in our carrier cancellation procedure. We switch our carrier cancellation on or off by turning the attenuator from a value of about 20dB to a value of 100dB, as we expected our variable attenuator to behave as an ideal attenuator, this should have had little impact on the noise, and should be constant. However, the variable attenuator has a different impedance mismatch for different values of attenuation[36], and since it is a powered device, its noise output may be different altogether. Since the settings for the carrier cancellation were found organically as denoted in 3.4 and are not unique and may differ with each attempt, the noise calibration was done with the phase shifters and variable attenuator were set to a default value instead of the values used for the JPA measurement in figure 6.24 and 6.28. This means that the offset between the JPA with carrier cancellation and the short can be positive and negative.

If the noise output of the variable attenuator is independent on the signal input, or these differences are small,$< 0.001N_{main}$ we would get a constant contribution to the found N_{main} by our thermal noise calibration procedure, which would be on the order of $0.01N_{main}$. As well as for the noise we see at the SA, independent of temperature of the sample. For this reason, we'll try calculate the N_{JPA} without using the value found for N_{main}. To this extent, we use some additional knowledge on the noise output of the JPA:

$$P_{JPA} = A_{JPA}P_0(\omega_s) + \left(A_{JPA}-1\right)P_0(\omega_i) \tag{6.16}$$

With $A_{JPA} \gg 1$.[2] The JPA is a mixer between the signal and idler frequency, and will add as noise the noise at the idler frequency. Using this equation we can calculate the in going noise without using N_{main}, though it will still depend on the amplification found.

$$P_0 = \frac{P_5(JPA_{on}) - P_5(JPA_{off})}{2A_{JPA}-2} = \frac{P_1(JPA_{on}) - P_1(JPA_{off})}{A_{main}\left(A_{JPA}-1\right)} \tag{6.17}$$

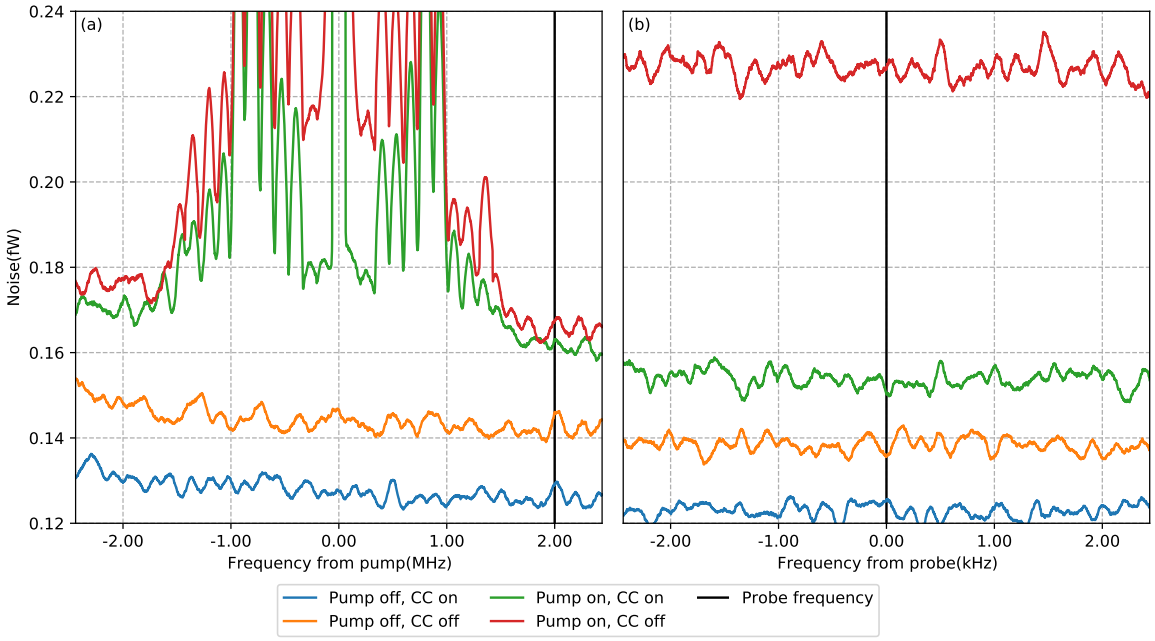

Figure 6.28: Comparison of the smoothed noise of different pump and carrier cancellation settings in two frequency ranges. The smoothing is done with a normal distribution on power, the unsmoothed measurements in the large range with carrier cancellation on can be seen in figure 6.24. The noise seen on the SA depends on whether the carrier cancellation is on or off, even even without pump(blue and orange). Also, one can see that value found on the SA without CC and with pump is differs between the frequency ranges. The small range measurement probably overestimates the amount of noise due to the large pump input outside of its range.

Where we approximated $P_0(\omega_i) \approx P_0(\omega_s) = P_0$ for clarity, based on figure 6.28. The result is no longer dependent on N_{main}, but it is on A_{main}. This is not as detrimental to the significance of our result, as can be seen in 6.29 with the green line, as neither the sign and the order of magnitude changes. If the noise contribution of the carrier cancellation is significant even with the noise calibration, the amplification will be underestimated.

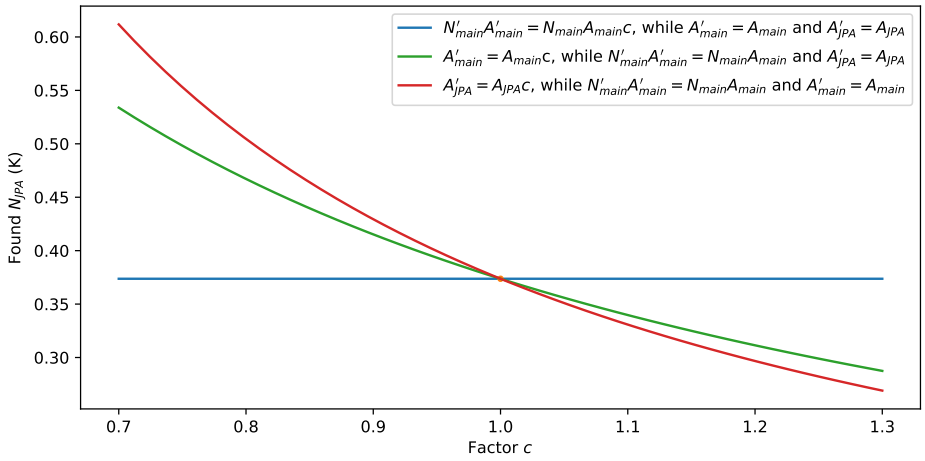

Figure 6.29: Impact of errors on the found input noise by equation 6.17. Compared to figure 6.27, errors in NA have no impact anymore, and the others will not change the order of magnitude or the sign.

We find a value of $N_{JPA} \approx 0.37$K which is close to the expected value of the temperature of the sample plate $T_s \approx 0.3$K. The classical amplifier input noise can then be found as, though for large A_{JPA} it is approximately the same.

$$N_{JPA} = P_0 \frac{A_{JPA} - 1}{A_{JPA}} \tag{6.18}$$

If the difference is not caused by the carrier cancellation, but mostly by transmission differences, the

offset might still be constant, but this is not certain. The reflection of the JPA changes with power, and its phase should have a significant impact.

7

Recommendations

In this report we tried to get a calibrated measurement of a nanobridge, current pumped Josephson parametric amplifier. Throughout this project we learned not only the characteristics of our JPA, but also the limits of our calibration setup. We now come to a few recommendations if one wishes to improve upon this project either on the device itself, or our types of calibration which we used to measure it. These can be read in the next sections, for the JPA, for the SOL calibration and for the thermal calibration, in section 7.1, 7.2 and 7.3 respectively.

7.1. JPA

Our nanobridge JPA showed limited flux tunability, and gain. For practical purposes, these would need to be improved. The limited flexibility of the gain is probably due to a combination of these factors.

Flux tunability

First for the flux tunability, the limiting factor is at this moment the self inductance. At low power, this is less of a problem, but limiting the usage to lower pump power would reduce the dynamic range regardless of the size of the non-linearity. The self inductances introduces hysterisis into the flux behaviour, which can be entirely avoided if the self inductance is low enough. β_L was lower for the single SQUID than the SQUID array, but lower self inductance should be relatively easily achieved by reducing the inductance of the loop compared to the junctions. If one needs more linear inductance, one could move this to a different point.

But even if there would be no hysteresis, the frequency range would still be quite limited. According to paper Kim et al. [21], this is highly dependent on the relative size of the linear and non-linear inductance and capacitance. I would regard experimenting with different amounts of inductance and self inductance as the best course of action, possibly with just a single SQUID.

Gain and heat generation

Secondly the gain was quite limited, which could be due to our setup, but the device needed to be pumped with a lot of power, and even then would not come near its critical state, which is needed for high gain. At other points we saw heat generation, so higher gain could not be achieved anyway. In the previous project, this was not seen, so it could possibly be due to detoriation of the nanobridges, or the breaking of an individual one. The frequency of the JPA has changed in between the projects as well. This detoriation should be mostly be dependent on the design of the nanobridges.

One could always reduce the amount of SQUIDS in the array, which does however reduce the dynamic range. One could also assume it is due to detoriation and retry the design, testing whether one can reach the critical state can be done by using a high power VNA measurement, as the slope of the phase shift indicates the photon number state.

7.2. SOL Calibration

The cryogenic SOL calibration showed great insight in our measurements and the problems with our setup. One of the problems we faced while measuring our JPA however, is that it is dependent on the absolute power

input, which we cannot find with this setup. Normally, one could add a switch and do a short open load through calibration, which would give the ingoing line and outgoing line seperately. However, with our HEMT and isolator in the outgoing line this is not possible.

Setup for getting a picture of the absolute power at the device
One could go around this problem by removing some attenuation of the input line, and then doing an S_{11} measurement, which would give us enough information without even a second switch.

If the reduced attenuation would result in too much noise leakage into the microwave circuit, one can also use a third line and a second switch. The first switch would then be used for the different devices, while the second switch would be used to connect the different lines together. So in that case a much simpler switch would be sufficient. One can also think about a variable attenuator, though one has to account for its differing transmission behaviour by doing certain calibration measurements twice, one each for the atteuator settings.

Getting a picture of the idler gain
At multiple times in this project, the calibrated gain found was distorted by the gain at the idler frequency. This could be circumvented by including this in our SOL calibration. Even without knowing the absolute power as mentioned in the previous section, we could use the JPA itself as a mixer to get the transmission separately, since we know the idler takes two different paths.

A way to do this is by putting a mixer in front of a VNA around the pump frequency, or by simply setting the VNA to measure at the idler frequency. If we had total freedom of the send frequencies of the output and input, we could also get rid of the image the pump makes on a VNA, by letting the VNA be the pump. Next would be to measure at the idler and signal frequency simultaneously.

Reducing backreflection
One of the problems encountered with the JPA was the limited calibrated gain. This turned to be not caused by the device itself, but the setup, as the back reflection results in a feedback loop. Our idea was to measure while the fridge was still warm, adjust things till the back reflection was below $-20dB$, and then cooldown. But this turned out to be insufficient, as the S_{22} spectrum greatly changed when cooling down. And as can be read in section 5.2.3, the difference in this regard between the circulator and directional coupler is not significant.

There are two ways to go about this, of which the easiest is to add some attenuation in front of the device. The closer to the device the smaller the chance is of backreflection to the device, but if one could add it right before the switch it would be calibrated out. It would be useful to test the wire connecting the device to the switch with the SOL calibration, so one has an estimate of its properties.

This also leads to our the second idea, to test the wires using the same setup by either attaching it after the switch and connecting nothing to the other side of the wire to get an idea of the absolute transmission. Or one can attach it before the switch and use the SOL calibration to get a more precise idea. We can also do this for the components used in this setup, though knowledge of the absolute power is possibly required. For starters, the isolator used, Pas [27], would be ideally only suitable up to 18dB of gain, though it is difficult to say if it is the limiting factor at this moment. Testing all these components would be time consuming and difficult, as cooling down changes properties, so adding some attenuation is preferable if one is not looking for large uncalibrated gain.

7.3. Thermal Calibration

As for the thermal calibration, this was quite unwieldy in our current setup, as our sample plate needed to be at a different temperature in its entirety. Since the Entropy does not cool continuously to base temperature, this is not done in the same manner for each temperature. In addition, at higher temperatures but still below the recharge temperature, the temperature is quite instable. Both of these factors lead to uncertainties in whether the temperature gradients are exactly the same, changing the transmission values of our system.

Secondly since the entropy is not continuously cooled, this poses a limit to how many temperature points can be taken for a single recharge.

If one wishes to use a thermal calibration in the future, it is thus highly advisable to have a separate source for the noise at the sample plate. If it is well isolated, and has a seperate temperature sensor, we would lose these uncertainties, in addition to the fact that it would be more practical to the different temperature

measurements, and we could take more of them. We can go in two different directions, we could use a heated load attached to the fridge, or we could use heated attenuation in the input line.

Heated Load
A heated load can be isolated from the sample plate, but still connected to the switch. The wire connecting this load to the switch should be as short as possible, and can change the amount of noise seen from the reference plane of the switch, since the reference plane is at the heated load. The amount of noise can only be used this way, as it cannot be used as input in the device. This means that the problems we encountered due to leakage due to carrier cancellation, or loss due to the wire to the device, would still be problematic.

Heated Attenuator
If one wishes to find the input noise of an amplifier, a better way would be to use a heated attenuator. Because in that case we do not just use the reference plane of our main amplifier chain, we can also take the reference plane of our device. As can be seen in Simbierowicz et al. [32], one can use it in this way to find the input noise. With a current pumped amplifier, one can also find the gain and do the thermal noise calibration, at the same time. In the case of the entropy, switching reduces the time the sample plate can stay at base temperature, and produces temperature gradients of its own, so doing it that way would be more cumbersome.

8

Conclusion

The starting point of this thesis, was the work done by Jasper in Franse [13] on a nanobridge Josephson Parametric Amplifier. Though rough measurements had already been done, a more detailed description of gain and tunability was needed. Beyond this, the noise figure of the device was also of interest.

At the start of measuring the gain we realized though, that for a reliable estimate of the absolute gain, we would need to know what happens at the port of the device, instead of the fridge. To do this, we looked into short-open-load calibration, and tested this at room temperature resulting in chapter 5. We find here that we can get a very close estimate of the actual reflection spectrum of the device.

We started out by looking at the tunability of the resonance frequency by flux, which showed that it is much less than the JPA of Grenoble [28]. The gain could be improved by reducing the hysteric behaviour, or β_L, but this would only about triple the amount. Changing the proportions of the SQUIDS and the resonators should be able to improve the results.

Next up was the gain of the JPA, where we could refind the results from Franse [13], with about 25dB of gain. However using our calibration, this decreased to about 12 dB. Achieving more gain showed to be problematic, as the device seemed to be less sensitive to power than before, and the reflection spectrum collapsed at higher power. This maximum gain peak frequency could also not be tuned in the same manner as the resonancy, as it did not show the same gain at every point.

Using the data from the calibration we found out that this is due to backreflection, and that the setup is the limiting factor in the maximum of calibrated gain. It could also give an idea of the absolute pump power entering the device for differing frequencies and the same data also could provide an estimate of the gain found through the idler frequency. The SOL calibration thus showed to be invaluable to get not only an estimate of the absolute gain, but also to figure out problems in the microwave system. It could be used in a future project to reduce the backreflection to make higher calibrated gain possible. It cannot find the absolute power at the device, but this could be done by changing the setup.

Finally, we wanted an estimate of the input noise of the device, an to do this, we did a thermal calibration. We did this by changing the temperature of the entire sample plate, which can be improved upon by using a heated load or attenuator instead. At first our numbers seemed to be insensible, but we found that the Carrier Cancellation required for accurate noise measuring of the signal of a current pumped JPA, leaked noise in our setup. Since this would provide a constant offset, we redid the calculation in a way to remove the dependence on that, which did show that the JPA approximately had the noise figure we expected. Which would mean a half quantum noise at zero temperature.

Bibliography

[1] Y. Aharonov and D. Bohm. Significance of electromagnetic potentials in the quantum theory. *Phys. Rev.*, 115:485–491, Aug 1959. doi: 10.1103/PhysRev.115.485. URL https://link.aps.org/doi/10.1103/PhysRev.115.485.

[2] Jose Aumentado. Superconducting parametric amplifiers: The state of the art in josephson parametric amplifiers. *IEEE Microwave Magazine*, 21(8):45–59, 2020.

[3] J. Bardeen, L. N. Cooper, and J. R. Schrieffer. Microscopic theory of superconductivity. *Phys. Rev.*, 106:162–164, Apr 1957. doi: 10.1103/PhysRev.106.162. URL https://link.aps.org/doi/10.1103/PhysRev.106.162.

[4] Manuel Angel Castellanos Beltran. *Development of a Josephson Parametric Amplifier for the Preparation and Detection of Nonclassical States of Microwave Fields*. PhD thesis, B.S., Tecnol´ogico de Monterrey, 2002.

[5] D Bothner, IC Rodrigues, and GA Steele. Photon-pressure strong coupling between two superconducting circuits. *Nature Physics*, 17(1):85–91, 2021.

[6] ME Brinson and Stefan Jahn. Qucs: A gpl software package for circuit simulation, compact device modelling and circuit macromodelling from dc to rf and beyond. *International Journal of Numerical Modelling: Electronic Networks, Devices and Fields*, 22(4):297–319, 2009.

[7] Marvin E Cage, Kv Klitzing, AM Chang, F Duncan, M Haldane, Robert B Laughlin, AMM Pruisken, and DJ Thouless. *The quantum Hall effect*. Springer Science & Business Media, 2012.

[8] Herbert B. Callen and Theodore A. Welton. Irreversibility and generalized noise. *Phys. Rev.*, 83:34–40, Jul 1951. doi: 10.1103/PhysRev.83.34. URL https://link.aps.org/doi/10.1103/PhysRev.83.34.

[9] John F Cochran and DE Mapother. Superconducting transition in aluminum. *Physical Review*, 111(1): 132, 1958.

[10] Alexander P. A. Cronheim. A circuit lagrangian formulation of opto-mechanical coupling between two electrical resonators mediated by a squid. Master's thesis, TU Delft, 2018.

[11] Christopher Eichler and Andreas Wallraff. Controlling the dynamic range of a josephson parametric amplifier. *EPJ Quantum Technology*, 1(1):2, Jan 2014. ISSN 2196-0763. doi: 10.1140/epjqt2. URL https://doi.org/10.1140/epjqt2.

[12] Ugo Fano. Effects of configuration interaction on intensities and phase shifts. *Physical Review*, 124(6): 1866, 1961.

[13] W.J.M. Franse. Design and fabrication of a josephson parametric amplifier based on nanobridge junctions. Master's thesis, TU Delft, 2019.

[14] Crispin W Gardiner and Matthew J Collett. Input and output in damped quantum systems: Quantum stochastic differential equations and the master equation. *Physical Review A*, 31(6):3761, 1985.

[15] Christopher Gerry, Peter Knight, and Peter L Knight. *Introductory quantum optics*. Cambridge university press, 2005.

[16] Alexander Golubov and M. Kupriyanov. The current-phase relation in josephson tunnel junctions. *Journal of Experimental and Theoretical Physics Letters*, 81, 04 2005. doi: 10.1134/1.1944074.

[17] *HHF SMA-Calibration-Kit*. Heuermann, 3 2013.

[18] OW Kennedy, J Burnett, JC Fenton, NGN Constantino, PA Warburton, JJL Morton, and E Dupont-Ferrier. Tunable nb superconducting resonator based on a constriction nano-squid fabricated with a ne focused ion beam. *Physical Review Applied*, 11(1):014006, 2019.

[19] *Data Sheet 85521A Cal Kit Type-3.5mm(f) 50 ΩbDC to 26.5 GHz*. Keysight, 4 2014. Issue A.

[20] *N9020B MXA Signal Analyzer Specifications Guide*. Keysight, 11 2021.

[21] Eun-jong Kim, JR Johansson, and Franco Nori. Circuit analog of quadratic optomechanics. *Physical Review A*, 91(3):033835, 2015.

[22] Ivana Kovacic and Michael J Brennan. *The Duffing equation: nonlinear oscillators and their behaviour*. John Wiley & Sons, 2011.

[23] Cihan Kurter, Alexander P. Zhuravel, Alexey V. Ustinov, and Steven M. Anlage. Microscopic examination of hot spots giving rise to nonlinearity in superconducting resonators. *Phys. Rev. B*, 84:104515, Sep 2011. doi: 10.1103/PhysRevB.84.104515. URL `https://link.aps.org/doi/10.1103/PhysRevB.84.104515`.

[24] Jan T. Li. Background interference in q factor measurement of microwave resonators. Bachelor's thesis, TU Delft, 2018.

[25] W. Meissner and R. Ochsenfeld. Ein neuer Effekt bei Eintritt der Supraleitfähigkeit. *Naturwissenschaften*, 21(44):787–788, November 1933. doi: 10.1007/BF01504252.

[26] Harry Nyquist. Thermal agitation of electric charge in conductors. *Physical review*, 32(1):110, 1928.

[27] *Isolator with 18 dB Isolation from 4 GHz to 8 GHz, 10 Watts and SMA Female*. Pasternack, 2020. Rev 1.3.

[28] Luca Planat, Rémy Dassonneville, Javier Puertas Martínez, Farshad Foroughi, Olivier Buisson, Wiebke Hasch-Guichard, Cécile Naud, R. Vijay, Kater Murch, and Nicolas Roch. Understanding the saturation power of josephson parametric amplifiers made from squid arrays. *Phys. Rev. Applied*, 11:034014, Mar 2019. doi: 10.1103/PhysRevApplied.11.034014. URL `https://link.aps.org/doi/10.1103/PhysRevApplied.11.034014`.

[29] *COAXIAL SUBMINIATURE MULTIPORT SWITCHES*. Radiall, 2 2018.

[30] Andrej Rumiantsev and Nick Ridler. Vna calibration. *IEEE Microwave magazine*, 9(3):86–99, 2008.

[31] Rohde & Schwarz. White Paper: Fundamentals of Vector Network Analysis. Technical report, Rohde & Schwarz USA, 11 2018.

[32] Slawomir Simbierowicz, Visa Vesterinen, Joshua Milem, Aleksi Lintunen, Mika Oksanen, Leif Roschier, Leif Grönberg, Juha Hassel, David Gunnarsson, and Russell E Lake. Characterizing cryogenic amplifiers with a matched temperature-variable noise source. *Review of Scientific Instruments*, 92(3):034708, 2021.

[33] Michael Tinkham. *Introduction to superconductivity*. Courier Corporation, 2004.

[34] Rik van der Spek. Quantum features of the driven, dissipative duffing oscillator. Master's thesis, TU Delft, 2020.

[35] J. van Leenen. Carrier cancellation. Bachelor's thesis, TU Delft, 2021.

[36] *Lab Brick® High Resolution Digital Attenuator*. Vaunix, 5 2020. Revision A.

[37] R. Vijay, E. M. Levenson-Falk, D. H. Slichter, and I. Siddiqi. Approaching ideal weak link behavior with three dimensional aluminum nanobridges. *Applied Physics Letters*, 96(22):223112, 2010. doi: 10.1063/1.3443716. URL `https://doi.org/10.1063/1.3443716`.

[38] Uri Vool and Michel Devoret. Introduction to quantum electromagnetic circuits. *International Journal of Circuit Theory and Applications*, 45(7):897–934, 2017.

[39] Bernard Yurke and Eyal Buks. Performance of cavity-parametric amplifiers, employing kerr nonlinearites, in the presence of two-photon loss. *Journal of Lightwave Technology*, 24:5054–5066, 2006.

9

Appendix

9.1. Motivation for calibration

As seen in the theoretical part, we would expect a flat plane with a lorentzian curve that bends to the side for higher power. We should be able to use this to parameterize the actual system.

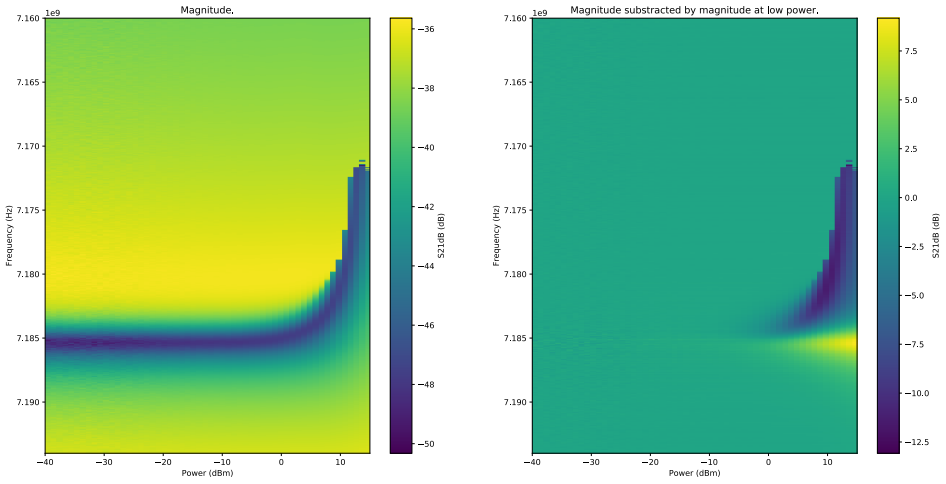

Figure 9.1: A flux frequency measurement of the first JPA by Jasper. The peak can easily be seen to lower frequencies for higher power, as expected.

As it turns out, the data is not that easy to decipher. We have a lot of dependence of the system on the background, in this picture it seems not to be so significant, but on a a larger range this background changes the result with up to 6 dB, and the other cavities used had a much broader but lower peak. I decided to not use the data directly, but use a subtraction. Since for lower powers the magnitude is quite stable, this part is averaged, and then the a new dataset is created by subtracting the original by these values. We get what we expect, since the lorentzian moves away, where it used to be gets a positive value, and where it moves to becomes negative. There were two odd outcomes though by using a fit, first the actual data is much more smeared then the fit, and there was much more loss then expected.

The same process was applied to the second JPA, but now we get some strange results. The peak seems to be inverted, and when using the subtraction, the peak indeed moves away, creating an inverted picture. The reason for this turns out to be probably interference, as the JPA was coupled with a circulator, the outgoing signal could probably reflect against the HEMT back into the cavity.

Using a fit we can try to find the attributes of this interference, and in this case the loss(the part that goes back into the cavity) seems to be on the order of 40%. We could try to use the inverse of this fit to get the

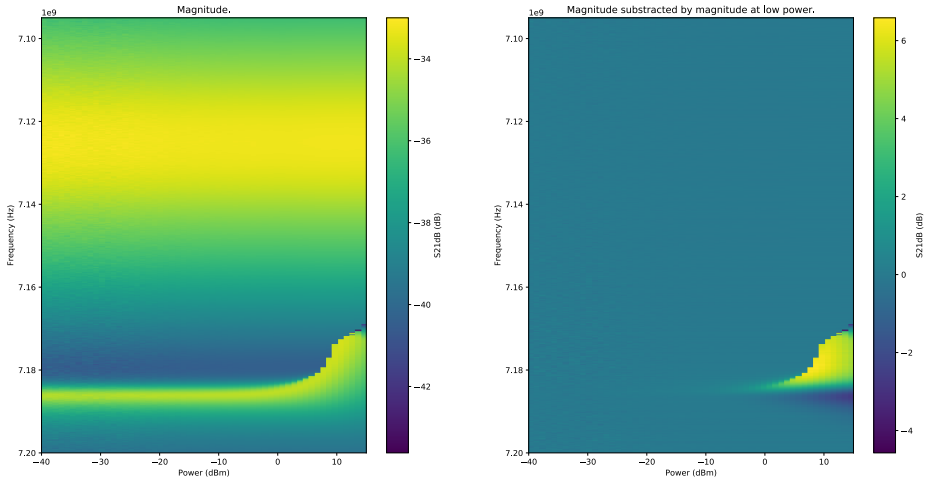

Figure 9.2: A flux frequency measurement of the second JPA by Jasper.

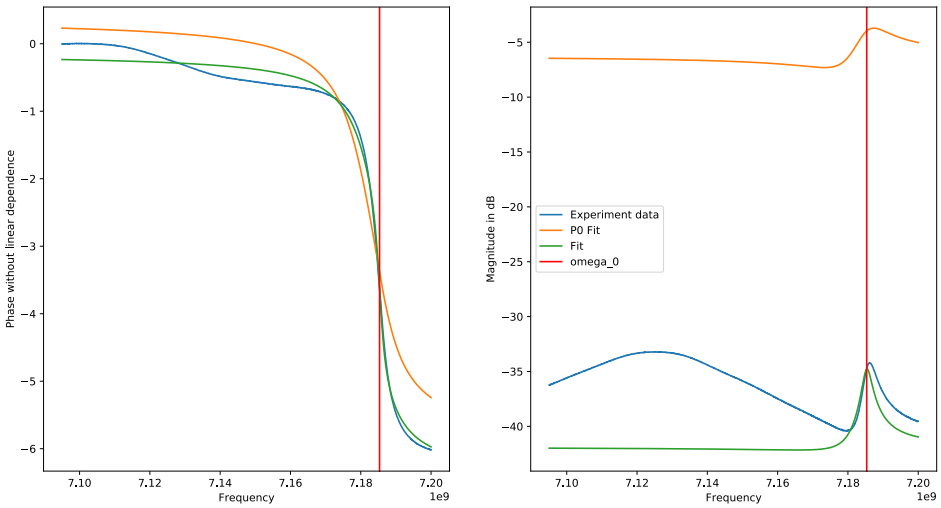

Figure 9.3: A fit for the measurement of the second JPA

original data back, but we run into a problem. As can be seen from the graph this would only work very close to the resonance frequency, while the subtraction only works away from the cavity. And there is another problem, the interference was probably there with the earlier JPA as well, so we did not notice anything there.

There are three graphs in this plot, figure 9.4, the first two describe our previous calculations, one for the fitted plot, and one for what we would expect the cavity to look like without interference. There is a huge difference in size. And another problem can be seen, if the interference is exactly destructive, we would get a much larger peak, but we would be none the wiser. This may have happened in our first attempt, there would be no way to tell.

We came up with two solutions, first is to use a directional coupler instead of a circulator, which would solve most if not all of our interference problems. We would however not get rid of most of our background dependence, since that is also due to our cables. Second is to calibrate the system, so we would be able to get the original data back, we would still have loss due to interference in this case, we would just be able to tell it apart.

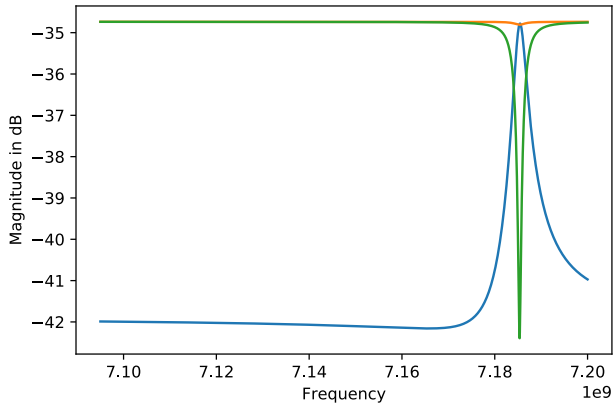

Figure 9.4: Possible effects of Fano on measurements done by Jasper

In the end we decided to do both, the replacement of the circulator with a directional coupler is straightforward enough, although interference may still remain due to its placement, as we don't want much loss. Calibration is more difficult, especially within a fridge, so the coming chapter is about that.

9.2. Theory

9.2.1. Through cavity

However we have two ports, not one, the input and output line are completely different, we could thus model our system as a through cavity.

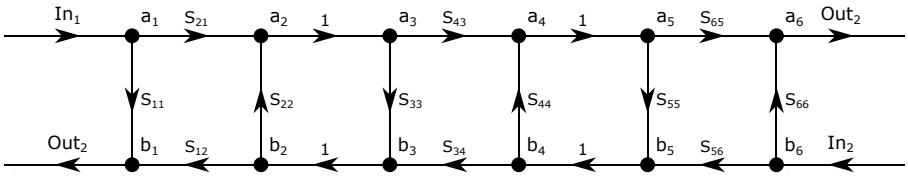

Figure 9.5: Simple model for Through Cavity

We can start doing the algebra immediately, but there are some assumptions we can make to get a clearer answer. First at the input we are not going to measure, so we can take S_{11} and S_{12} to be zero. Second we won't have an income signal from the second port, so we can take S_{56} and S_{66} also to be zero. Let's say that S_{43} is actually our Γ plus some bypass b. All in all this gives:

$$\Gamma' = \frac{S_{21} S_{43} S_{65}}{1 - S_{22} S_{33} - S_{22} S_{34} S_{43} S_{55} - S_{44} S_{55} + S_{22} S_{33} S_{44} S_{55}} \tag{9.1}$$

$$= \frac{S_{21} (\Gamma + b) S_{65}}{1 - S_{22} S_{33} - S_{22} S_{34} (\Gamma + b) S_{55} - S_{44} S_{55} + S_{22} S_{33} S_{44} S_{55}} \tag{9.2}$$

But since we don't care about the values of the parameters in the model we can see that it can be reduced to a simple equation:

$$\Gamma' = \frac{a + b\Gamma}{c + d\Gamma} \tag{9.3}$$

Which can be put in the same form as the equation for the reflection cavity!

9.2.2. Side coupled cavity

We don't have this simple reflection geometry though, we have a side coupled cavity.

Our input with an attenuator is connected to a circulator or a directional coupler, which also has the cavity and the HEMT with the output connected to it. We cannot give an input through the HEMT, so two

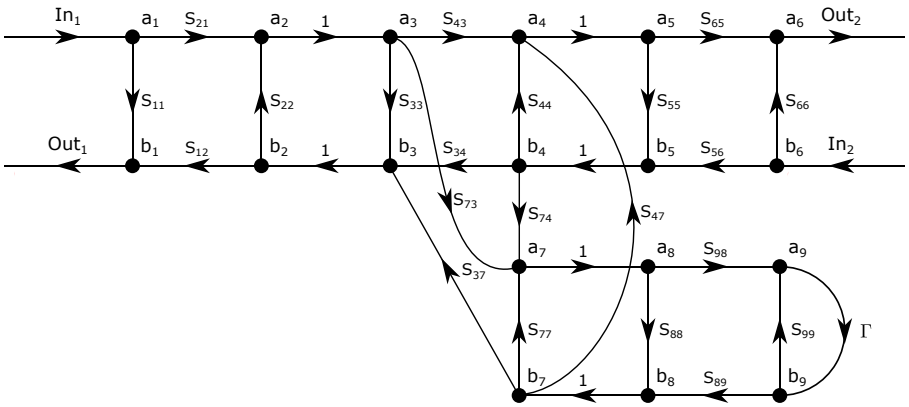

Figure 9.6: Simple model for Side-Coupled Cavity

unknowns won't matter. If the circulator or directional coupler is ideal, we could do with a simple calibration as previously described. This is however not the case for the circulator, so we need to calibrate that as well. We will go for a directional coupler in this case however, so we can assume the non-directional(S_{43} and S_{34}) terms to be negligible. When doing some linear algebra we actually go trough a similar process as the through cavity, resulting in the same form as the reflection cavity. Even with the circulator this happens, though of course interference may still be a problem, in reality loss will often reduce the quality of the signal, though most of this can be mitigated with the calibration.

Note however, that in the first case S_{21} and S_{12} are about equal, and not really significant, with a side-coupled cavity they are very different, as they travel along different wires. This will make an impact due to the fact that the JPA is non-linear. We cannot however find out these values separately without switching out the JPA with a third VNA cable.

9.2.3. RLCC circuit approximation comparison

Here we show a comparison between a few settings for the components of the cavity, with the approximation in figure 9.7, and the exact in 9.8. In these cases, $\omega^2 Z_0^2 C_c^2 \ll 1$ no longer holds. We can however see that the value found for ω_0 is still within an order of magnitude accurate.

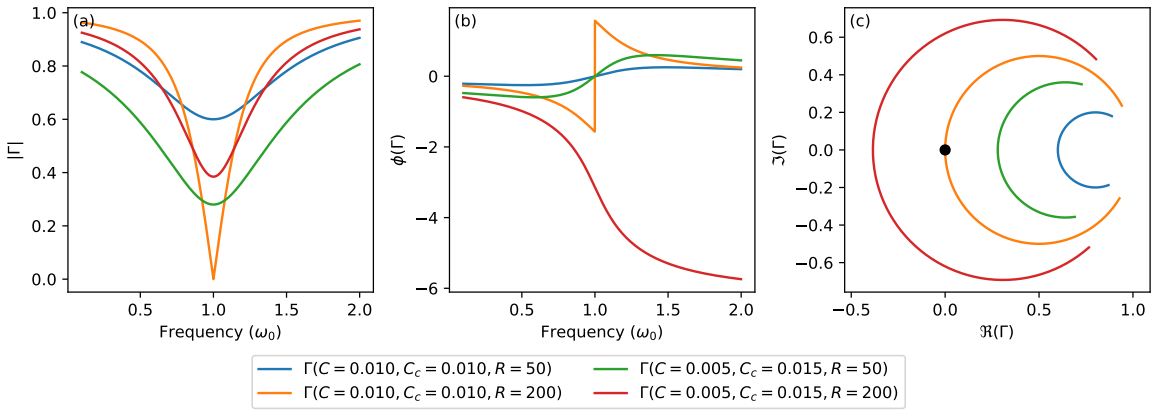

Figure 9.7: From left to right, magnitude, phase and polar plot of the approximate reflection spectrum of the cavity of the RLCC, for different values of capacitance and inductance. Here $Z_0 = 50$ and $\omega_0 = \frac{1}{\sqrt{L(C+C_c)}}$.

9.2.4. JPA pumped gain impact of δ and Δ

In figure 9.9 we show impact of the tuning of signal and pump on the gain. Note that with higher ξ the frequency of ideal pumping decreases.

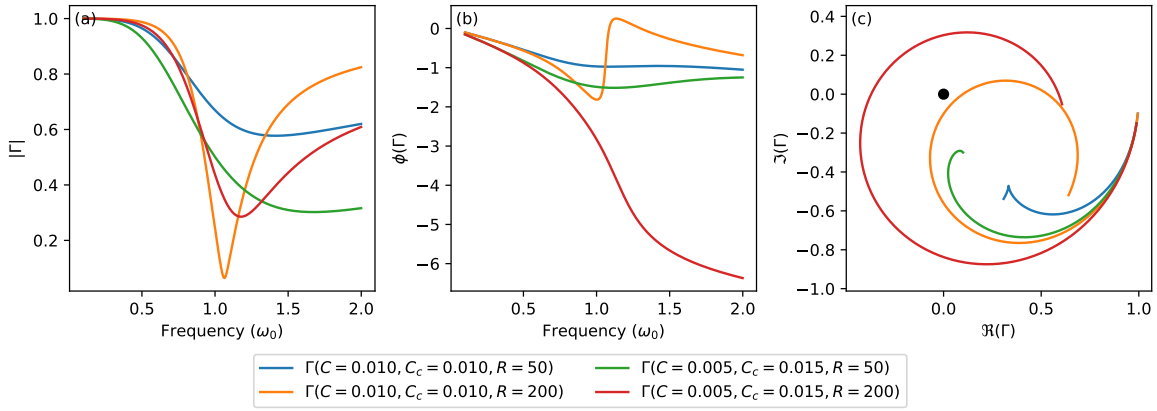

Figure 9.8: From left to right, magnitude, phase and polar plot of the exact reflection spectrum of the cavity of the RLCC, for different values of capacitance and inductance. Here $Z_0 = 50$ and $\omega_0 = \frac{1}{\sqrt{L(C+C_c)}}$.

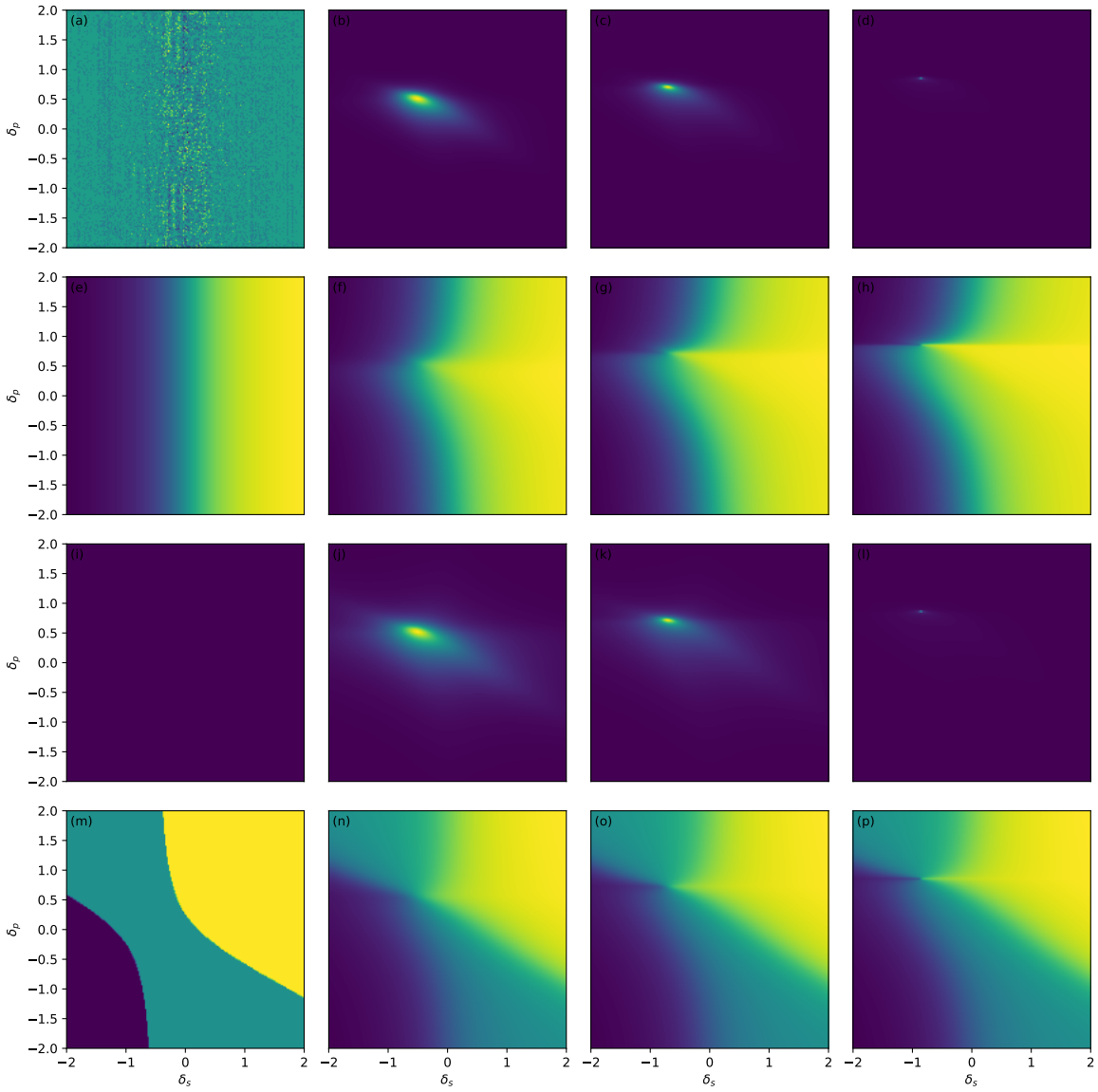

Figure 9.9: Simulated signal response of the JPA, for different settings of ξ, Δ, and δ. With from left to right, $\xi = 0$, $\xi = 0.5\xi_{crit}$, $\xi = 0.75\xi_{crit}$, $\xi = 0.98\xi_{crit}$, and from top to bottom, $|g_s|$, $\phi(g)$, $|g_i|$ and $\phi(g_i)$.

9.3. Components

9.3.1. Fridge

In this project we use the He7 Entropy to hold our device and the switch for calibration, this an be pumped to near vacuum and cooled to near zero, 100pbar, and 0.3K. It consists of multiple stages of which each is continuously cooled except for the last one, the sample plate, as can be seen in figure 4.4, This one is stable at about 2.7K, but can be cooled temporarily to 0.3K by using the Helium contained within the two pumps in the fridge.

For our thermal noise calibration, we need to control the temperature of a certain load. Since we don't have a separately heated load, we change the temperature of the sample plate. We can add heat to the sample and main plate by using a heater. This is not very practical to control these temperatures, as in our setup the base temperate is not achieved by continuous cooling, so we need to alter the conduction to the pumps.

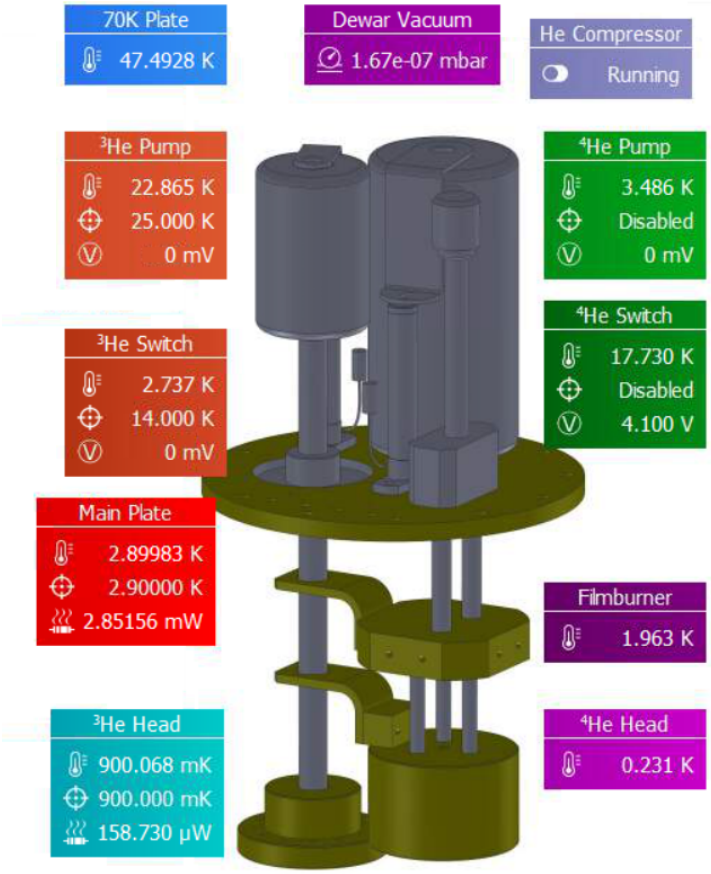

Figure 9.10: Interface of the He7 Entropy.

The cooling power of the fridge is controlled in this manner, there are two pumps, one for He3 and one for He4. These either absorb or output the gas, when hot or cold respectively. These are linked to the plates by the switches, which are open to heat transfer when hot, and closed when cold. He3 has immense cooling power, so when there is He3 to gas, it will keep the fridge at base temperature.

First are the temperatures above $2.7K$, these can be achieved by conventional means, where we keep the Helium gassed. We use the sample plate heater to increase the temperature of this plate, while keeping the main plate temperature constant. This is done as the temperature of the wire between the plates, and the amplifier will influence the noise on the SA. We use a small feedback loop, though this does mean that the actual temperature, and its derivative is temperature dependent and could influence our noise measurement. We also have the HEMT adding heat to the main plate, so that temperature will not be perfectly constant either.

Below this temperature, it is much trickier to control the temperature. Though at first it was proposed to control the temperature of the pumps, this is not feasible, as when the links are open, the heat of the pumps

easily escapes to the main plate. So we did it the other way around, cooling the links, so the cooling power was contained at the pumps. At first I tried to let the temperature descend controlled, however the opening of the links happened in only a small window of temperature, making it though to control.

In the end, we preceded as follows, first we initialized for a regular cooldown. Then we turned off the heaters of the pump while heat the ones of the links only slightly. When the fridge was at or nearing base temperature, we let the links cool off so they closed. Then we could heat up the sample plate, while we expended He4 and He3, which cooled the sample plate as leakage cooling power. This means that our time window is very limited, much shorter than a normal cooldown. It also means that the derivative of temperature is larger at higher temperatures, and very different from temperatures in the other domain.

9.4. Data Analysis

Here I will describe in more detail how I find the values of parameters and the more rudimentary way of making the data accessible. This does not include the SOL calibration, which is described in detail in chapter 5.

9.4.1. Phase Unwrapping

Phase is not trivial to define, but with our data, we can use the equation $\phi = \mathrm{Im}\{\ln s\}$, where s is the signal. But this will result in many discontinuities depending on the branch, which we will remove by 'unwrapping', adding 2pi for each continuity encountered in a spectrum, as seen in figure 9.11, taken from our reference cavity.

Another issue we have is the increased accumulation of phase by increasing frequency and length of the wire. Since we do not change the length of the wire, each load will have a phase in crease with frequency depending on its wirelength. This should be approximately linear, and can thus be easily removed if one knows the spectrum of the device. However, since our device, the JPA, has an incredibly wide cavity, this can be hard to distinguish, since both are antisymmetric around the cavity resonance. But not removing this linear dependence is not an option either, as the behaviour of the JPA cannot be distinguished with it.

We will therefore use a reference, the Open, where the linear dependence can be easily defined. This is also what is inherently used by the SOL calibration, so we can easily compare the raw and the calibrated phase response. This may still result in a lot of phase accumulation due to the wire connecting the device to the switch, where can apply some assumptions and approximations to get an idea of the phase dependence. If the device on the other side is relatively well known, like our JPA, we know the order of the dependence, and we can assume the linear dependence of the phase on frequency dominates, and is the same for each frequency.

9.4.2. Finding the cavity resonance

To pinpoint the location of the cavity, we use the gradient of the phase, as that should be at its maximum, or minimum at the cavity, as can be seen in 9.11, with an undercoupled or overcoupled cavity respectively. One can also see that the inferred resonance frequency is different for the calibrated data, which we expect to be closer to the cavity of the device.

We will have to deal with the inaccuracies though, as the noise influences our found resonance frequency. We use Gaussian distribution to smooth the data, which fits well with the lorentzian shape of our cavity. This should normally not change the cavity resonance, as they should both be symmetric. However, with FANO the cavity shape becomes assymetric, so it can be off. Worse, with high power the shape becomes highly assymetric for the JPA, resulting in an overestimation of the resonance frequency, and thus an underestimation of the phase shift caused by the power.

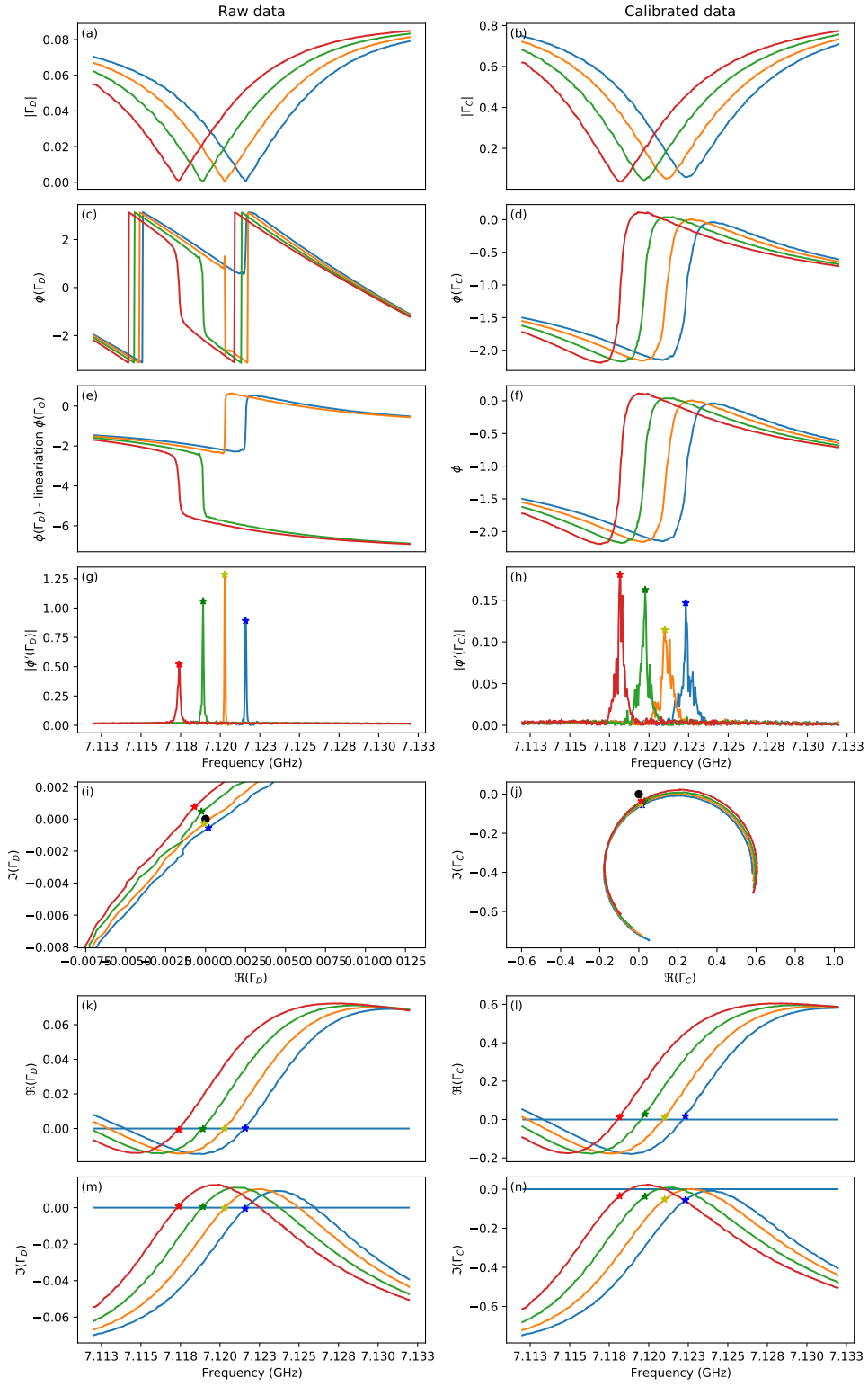

Figure 9.11: Now with four values close to the switch of being shown as over from undercoupled in the raw data.

9.5. Additional plots

9.5.1. Simulations plots

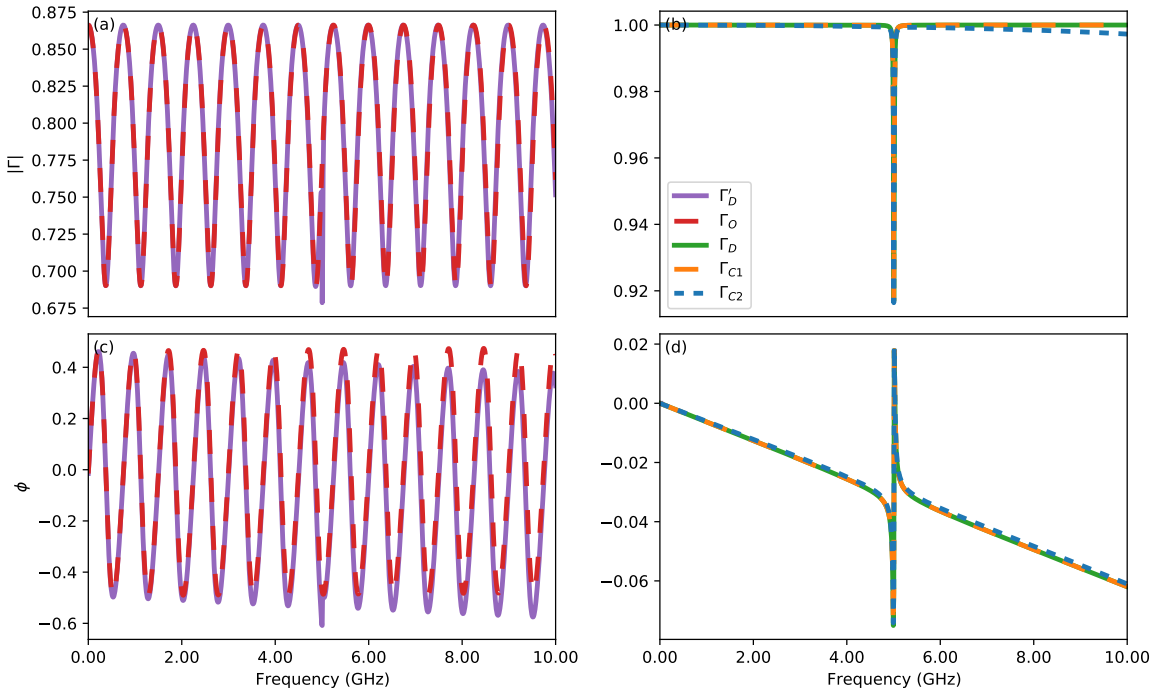

Figure 9.12: Comparison between the uncalibrated cavity response on the left, and calibrated and pure cavity response on the right, using the simulation circuit in figure 5.1 and 5.4. Visible is the deviation between the two calibrated magnitude plots, this is due to the phase difference between the Open and Short decreasing. A zoomed in version can be seen as figure 5.3

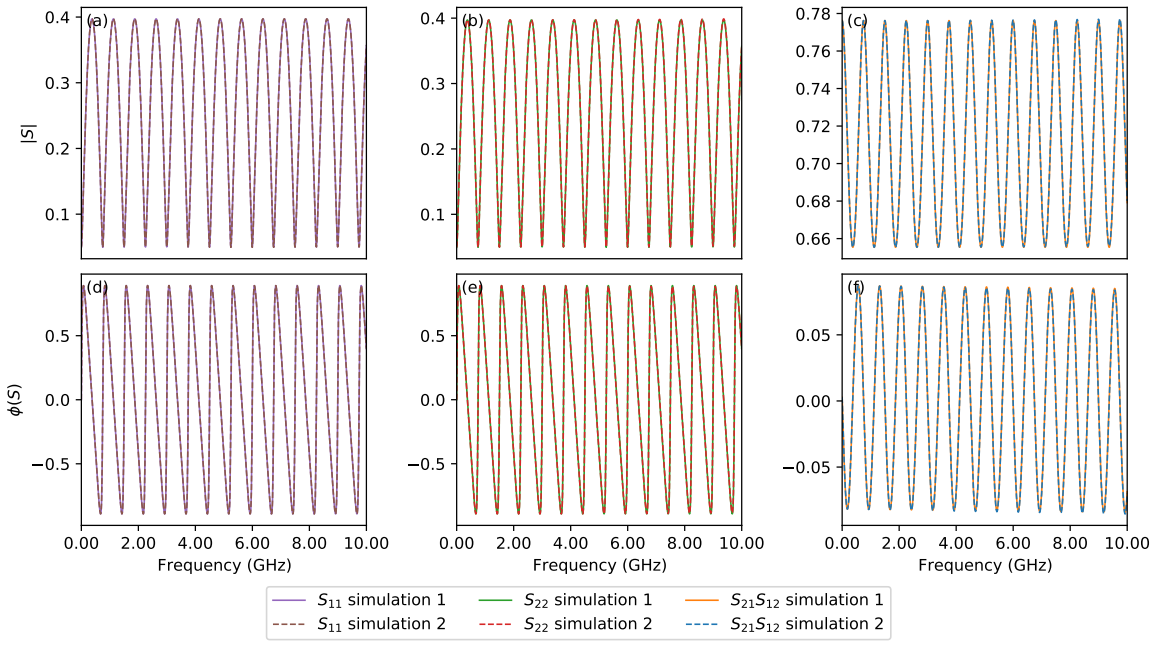

Figure 9.13: A wide frequency plot of the figure 5.6.

9.5.2. Cooldown3

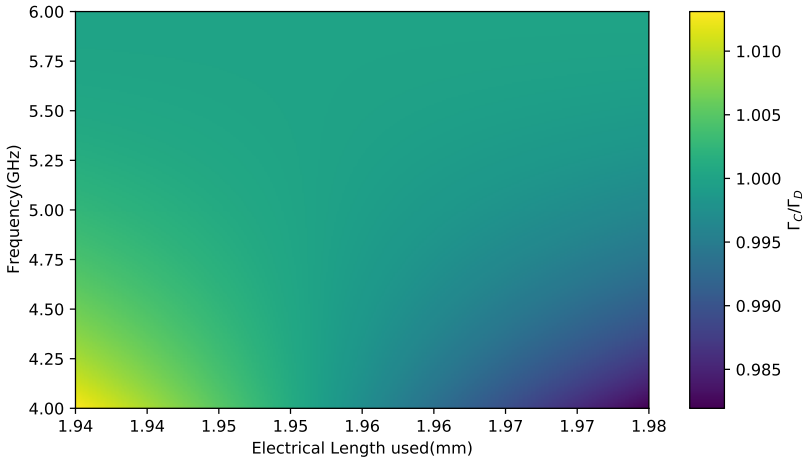

Figure 9.14: In this figure one can see the deviation between the actual resonator response function, Γ_D, and the found calibrated one Γ_C, with the simulation described in section 5.1.2. Notice that the deviation increases with larger frequency and larger pathlength differences.

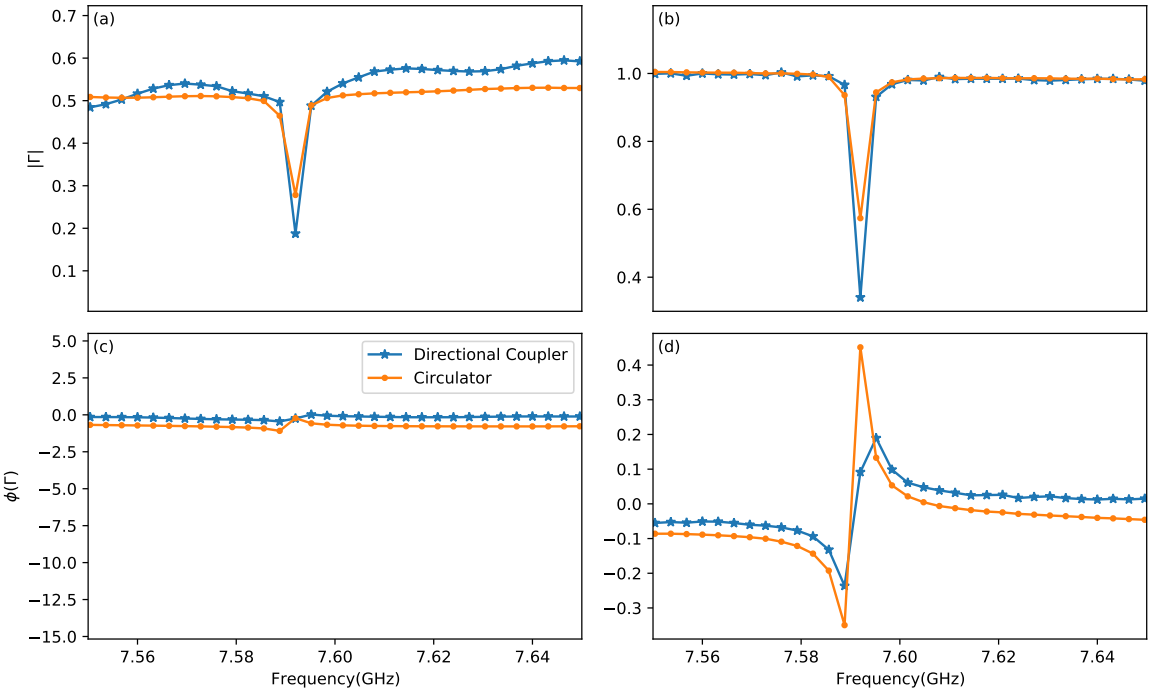

Figure 9.15: Zoom in on the comparison between the use of a directional coupler and a circulator in section 5.2.3. Here we can see that the amount of detail in not sufficient to compare them at cavity resonance.

9.5.3. Cooldown4

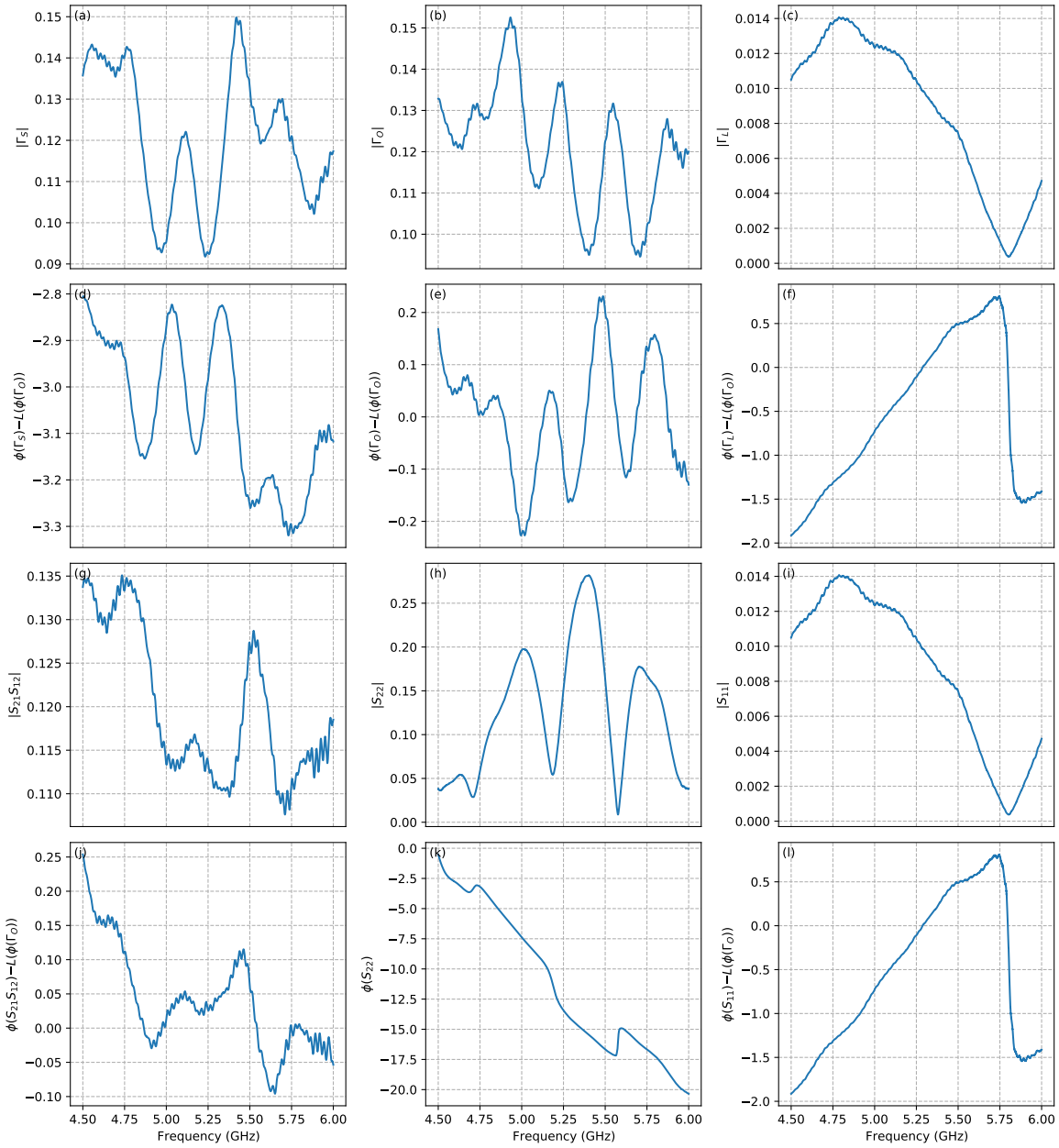

Figure 9.16: The scattering parameters found by calibration used at the third cooldown.

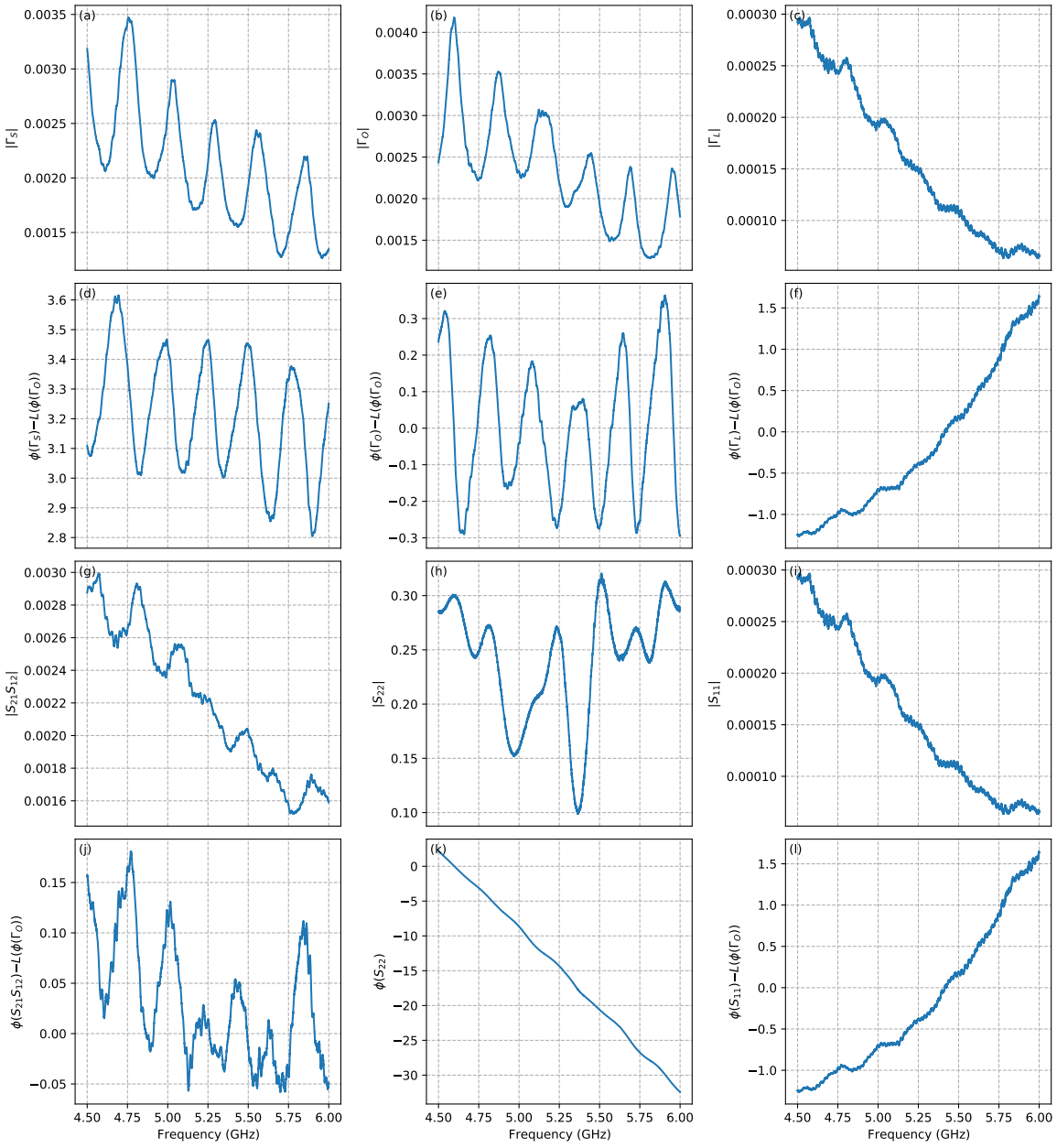

Figure 9.17: The scattering parameters found by calibration used at the fourth cooldown.

9.6. Carrier Cancellation code

```
def GetCarrierCancelationValues(frequency):
        start_att=30

        StartIQ(frequency)
        MeasureIQ(spectrum_analyzer)
        SetCarrierCancelation(100,0,0,frequency)
        sleepTime=3
        time.sleep(sleepTime)
        length=len(MeasureIQ(spectrum_analyzer)[0])
        I,Q=MeasureIQ(spectrum_analyzer)
        pump_vector=np.mean(I)+1j*np.mean(Q)
        print(pump_vector)
        print("Deviation"+str(abs(np.std(I)+1j*np.std(Q))))

        SetCarrierCancelation(start_att,0,0,frequency)

        time.sleep(sleepTime)
        I,Q=MeasureIQ(spectrum_analyzer)
        cancel_vector=np.mean(I)+1j*np.mean(Q)-pump_vector
        print("pump Vector, cancel vector",pump_vector,cancel_vector)
        phase_dif=(540-np.angle(cancel_vector,deg=True)
            +np.angle(pump_vector,deg=True))%360
        print(phase_dif,np.angle(cancel_vector,deg=True),
            np.angle(pump_vector,deg=True) )
        print(phase_dif)
        amplitude_dif=start_att+20*np.log10(abs(cancel_vector)/abs(pump_vector))
        cc_vector=(np.cos(np.deg2rad(phase_dif))+
            1j*np.sin(np.deg2rad(phase_dif)))*10**(-amplitude_dif/20)
        # print(20*np.log10(abs(np.mean(I)+1j*np.mean(Q)-pump_vector)),
            20*np.log10(abs(pump_vector)),amplitude_dif)

        SetCarrierCancelation(amplitude_dif,phase_dif,phase_dif,frequency)
        time.sleep(sleepTime)
        I,Q=MeasureIQ(spectrum_analyzer)
        final_vector=np.mean(I)+1j*np.mean(Q)
        print(20*np.log10(abs(cancel_vector)),20*np.log10(abs(pump_vector)),
            20*np.log10(abs(final_vector)))


        plt.ion()
        plt.show()
        plt.polar(np.angle(pump_vector,deg=True),
            20*np.log10(abs(pump_vector)),'ro')
        plt.polar(np.angle(cancel_vector,deg=True),
            20*np.log10(abs(cancel_vector)),'bo')
        plt.polar(np.angle(final_vector,deg=True),
            20*np.log10(abs(final_vector)),'go')
        plt.draw()
        plt.pause(0.001)

        new_cancel_vector=-pump_vector
        phase_dif=(360+phase_dif+(np.angle(new_cancel_vector,deg=True)-
            np.angle(cancel_vector,deg=True)))%360
        amplitude_dif-=20*np.log10(abs(new_cancel_vector)/abs(cancel_vector))
```

```
new_cc_vector=(np.cos(np.deg2rad(phase_dif))+
    1j*np.sin(np.deg2rad(phase_dif)))*10**(-amplitude_dif/20)
SetCarrierCancelationAdvanced(amplitude_dif,phase_dif,frequency)
time.sleep(sleepTime)
I,Q=MeasureIQ(spectrum_analyzer)
new_final_vector=np.mean(I)+1j*np.mean(Q)


sleepTime=0.1
impactVals=np.ones(400,dtype=complex)
cc_vectors=np.ones(400,dtype=complex)
best_cc=-1+1j
best_final=100
# spectrum_analyzer.set_attenuation(0)
for i in range(200):
        plt.draw()
        plt.pause(0.001)
        print("iteration: "+str(i))

        impact=(new_final_vector-final_vector)/(new_cc_vector-cc_vector)
        impactUsed=impact
        impactVals[i]=impact
        if(i>12):
                impactUsed=np.mean(impactVals[i-10:i-1])
        cc_vectors[i]=new_cc_vector
        next_cc_vector=-new_final_vector/(impactUsed*10)+new_cc_vector

        phase_dif=(360+np.angle(next_cc_vector,deg=True))%360
        print("Impact"+str(impactUsed))
        print(20*np.log10(abs(next_cc_vector)/abs(new_cc_vector)))
        print(phase_dif)
        amplitude_dif=-20*np.log10(abs(next_cc_vector))
        print(amplitude_dif)

        plt.polar(np.angle(new_cancel_vector,deg=True),
            20*np.log10(abs( new_cancel_vector)),'mo')
        plt.polar(np.angle(cancel_vector,deg=True),
            20*np.log10(abs(cancel_vector)),'bo')
        plt.polar(np.angle(final_vector,deg=True),
            20*np.log10(abs(final_vector)),'go')
        # SetCarrierCancelation(amplitude_dif,phase_dif,phase_dif,frequency)
        SetCarrierCancelationAdvanced(amplitude_dif,phase_dif,frequency)
        print("hjer")
        time.sleep(sleepTime)
        I,Q=MeasureIQ(spectrum_analyzer)
        next_final_vector=np.mean(I)+1j*np.mean(Q)
        # if(i>11 and abs(next_final_vector)>abs(1.5*new_final_vector)and
        #    abs(best_cc-new_cc_vector)>0.001 and
        #    abs(best_cc-cc_vector)>0.001):
        #        next_cc_vector=best_cc
        #        phase_dif=(360+np.angle(next_cc_vector,deg=True))%360
        #        amplitude_dif=-20*np.log10(abs(next_cc_vector))
        #        SetCarrierCancelationAdvanced(amplitude_dif,
        #    phase_dif,frequency)
        #        time.sleep(sleepTime)
        #        I,Q=MeasureIQ(spectrum_analyzer)
```

```
            #       next_final_vector=np.mean(I)+1j*np.mean(Q)

            if(abs(next_final_vector)<abs(best_final) ):
                    best_cc=next_cc_vector
                    best_final=next_final_vector

            final_vector=new_final_vector
            new_final_vector=next_final_vector
            cc_vector=new_cc_vector
            new_cc_vector=next_cc_vector
            print(20*np.log10(abs(new_cancel_vector)),
                20*np.log10(abs(pump_vector)),20*np.log10(abs(final_vector)))

    print(20*np.log10(abs(new_cancel_vector)),
        20*np.log10(abs(pump_vector)),20*np.log10(abs(final_vector)))
    phase_dif=(360+np.angle(best_cc,deg=True))%360
    amplitude_dif=-20*np.log10(abs(best_cc))
    SetCarrierCancelationAdvanced(amplitude_dif,phase_dif,frequency)
    print("hjer")
    time.sleep(sleepTime)
    I,Q=MeasureIQ(spectrum_analyzer)

    print(amplitude_dif,phase_dif,frequency)
    print("Final Carrier cancelation values, att: "
        +str(attenuator.GetAttenuation())+", phase1:"+
        str(phase_1.GetPhase())+", phase2:"+str(phase_2.GetPhase()))
    return attenuator.GetAttenuation(), phase_1.GetPhase(), phase_2.GetPhase()
```